Maria de Almeida Vasconcelos António

Deteção da proteína C-reativa utilizando nanopartículas de ouro funcionalizadas

Detection of C-reactive protein using functionalized gold nanoparticles

Universidade de Aveiro Departamento de Química
Ano 2017

Maria de Almeida Vasconcelos António

Deteção da proteína C-reativa utilizando nanopartículas de ouro funcionalizadas

Detection of C-reactive protein using functionalized gold nanoparticles

Dissertação apresentada à Universidade de Aveiro para cumprimento dos requisitos necessários à obtenção do grau de Mestre em Biotecnologia, realizada sob a orientação científica da Doutora Ana Luísa Daniel da Silva, Investigadora Auxiliar do Instituto de Materiais de Aveiro (CICECO) da Universidade de Aveiro e do Doutor Rui Miguel Pinheiro Vitorino, Investigador Principal no Instituto para Biomedicina (ibimed) da Universidade de Aveiro.

o júri

presidente   Professor Doutor João Filipe Colardelle da Luz Mano
professor Catedrático do Departamento de Química da Universidade de Aveiro

Doutora Sónia Oliveira Pereira
investigadora de Pós-Doutoramento do Departamento de Física da Universidade de Aveiro

Doutora Ana Luísa Daniel da Silva
investigadora Auxiliar do CICECO – Departamento de Química da Universidade de Aveiro

agradecimentos

Agradeço aos meus pais a possibilidade de realizar o mestrado e por me terem apoiado em todos os momentos. Aos avós por me apoiarem mesmo não percebendo nada do que é o meu mestrado ou dissertação. Ao meu irmão, namorado, madrinha do coração e amigos por me aturarem durante esta fase.

Agradeço também aos meus orientadores, a Doutora Ana Luísa da Silva por possibilitar a escolha do tema de tese e por todo acompanhamento durante a mesma e ao Doutor Rui Vitorino por todo acompanhamento na parte molecular. À Professora Doutora Rita Pereira por toda a ajuda, pela ultracentrifuga, albumina e micropipeta. À Doutora Bárbara Ferreira por todos os conselhos em relação ao ADN. À Doutora Sara Fateixa pela ajuda no Raman. À Mestre Celeste Azevedo por toda a ajuda no UV-vis, Raman e paciência no ATR-FTIR.

Um obrigada muito especial à minha avozinha, que infelizmente não conseguiu acompanhar-me até ao fim da tese. Tenho a certeza que te orgulhas por mais esta etapa da minha vida.

palavras-chave

Doenças cardiovasculares, proteína C-reativa, biodeteção, nanopartículas de ouro, funcionalização de superfícies, citidina difosfoscolina, aptâmeros.

resumo

Este projeto teve como objetivo desenvolver novas estratégias para funcionalizar nanopartículas de ouro (Au NPs) de forma a detetar a proteína C-reativa (CRP). Assim, foram sintetizadas nanopartículas de ouro esféricas com tamanhos médios de aproximadamente 10 e 40 nm. Posteriormente, a superfície das Au NPs foi modificada utilizando duas abordagens diferentes. Na primeira abordagem as Au NPs estabilizadas com citrato foram funcionalizadas com grupos ácidos carboxílicos pela modificação da superfície com os ligandos: ácido 11-mercaptoundecanóico (MUDA) e ácido mercaptopropiónico (MPA). Posteriormente a citidina difosfocolina (CDP) foi acoplada covalentemente à superfície das Au NPs utilizando 1-etil-3-(3'-dimetilaminopropil)carbodiimida (EDC) para promover a reação. Na segunda abordagem as Au NPs estabilizadas com citrato foram modificadas com um aptâmero específico para a CRP. Estes materiais foram caracterizados utilizando diversas técnicas de análise nomeadamente espectroscopia de UV-vis e de infravermelho (FTIR), medidas de potencial Zeta e de diâmetro hidrodinâmico e microscopia eletrónica de transmissão (TEM).

Amostras selecionadas de Au NPs modificadas com aptâmero (Au NPs@ssDNA+NaCl+KCl) e de Au NPs bioconjugadas com CDP (Au NPs@MUDA@CDP_40nm e Au NPs@MPA@CDP_10nm) foram utilizadas para o estudo da deteção da proteína: CRP. As Au NPs foram adicionadas a soluções de concentração conhecida (10 - 100 nM). A deteção da CRP foi investigada através da aquisição de espectros de UV-vis. O aumento da razão de agregação, isto é entre a absorvância a 620 nm e a absorvância da banda de ressonância de plasmão de superfície localizada (A_{620}/A_{LSPR}), foi monitorizada ao longo do tempo, indiciando a deteção da CRP para todas as amostras testadas. Para os sistemas Au NPs@MUDA@CDP_40nm e Au NPs@ssDNA+NaCl+KCl foi possível correlacionar a razão A_{620}/A_{LSPR} com a concentração da CRP através de uma relação linear nas gamas de concentração de 20 - 50 nM (R^2=0.9425) e de, 20 - 45 nM (R^2=0.9382) respetivamente.

Os resultados obtidos, embora preliminares, são promissores sendo necessário avaliar em estudos futuros aspetos tais como reprodutibilidade e interferência de outras proteínas em estudos futuros, tendo em vista o desenvolvimento de biossensores válidos para a deteção de CRP.

keywords

abstract

The main goal of this project was to develop novel strategies for the functionalization of gold nanoparticles (Au NPs) aiming the detection of C-reactive protein (CRP). Au NPs with an average size of 10 and 40 nm were synthesized. Then, the surface of Au NPs was modified following two different approaches. The first approach consisted on the surface functionalization of citrate stabilized Au NPs with carboxylic acid groups, by surface modification using 11-mercaptoundecanoic acid (MUDA) and mercaptopropionic acid (MPA). The cytidine diphosphocholine (CDP) was covalently attached to the surface of functionalized Au NPs using 1-(3-dimethylaminopropyl)-3-ethylcarbodiimide hydrochloride (EDC) to promote the coupling reaction. In the second approach, citrate stabilized Au NPs were modified with a CRP specific aptamer. These materials were characterized using several analysis techniques namely UV-vis spectroscopy, infra-red spectroscopy (F-T IR), zeta potential and hydrodynamic diameter measurements and transmission electron microscopy (TEM).

Selected samples of Au NPs modified with aptamer (Au NPs@ssDNA+NaCl+KCl) and CDP bioconjugated Au NPs (Au NPs@MUDA@CDP_40nm e Au NPS@MPA@CDP_10nm) were used for studying CRP detection. Au NPs samples were added to CRP solutions of known concentration (10-100 nM). The detection was measured through acquisition of the UV-vis spectra. The increase of aggregation ratio between absorbance at 620 nm and the absorbance of localized surface plasmon resonance band (A_{620}/A_{LSPR}) was monitored along time and, indicated that CRP was detected for all the Au NPs samples tested. For the systems Au NPs@MUDA@CDP_40nm and Au NPs@ssDNA+NaCl+KCl it was possible to find a linear correlation between the ratio A_{620}/A_{LSPR} and the CRP concentration, within the concentration range 20 - 50 nM (R^2=0.9425) and, 20 - 45 nM (R^2=0.9382), respectively.

The results obtained are very promising but still preliminary. Further studies are needed to evaluate key aspects such as reproducibility and interference of other proteins, keeping as main objective the development of valid biosensors for CRP detection.

List of abbreviations and symbols

A	Absorbance
A_{LSPR}	Absorbance at LSPR
AIDS	Acquired Immune Deficiency Syndrome
AMI	Acute myocardial infarction
APTES	(3-Aminopropyl)triethoxysilane
BMI	Body mass index
CAD	Coronary artery disease
CAd	Coronary artery diameter
CBF	Coronary blood flow
CD	Circular dichroism
CDP	Cytidine diphosphate
CE	Cardiovascular events
CED	Coronary endothelial dysfunction
CHD	Coronary heart disease
CRP	C-reactive protein
CVD	Cardiovascular diseases
Cys	Cysteine
Dh	Hydrodynamic diameter
DLS	Dynamic light scattering
DM	Diabetes mellitus
DNA	Deoxyribonucleic acid
DVT	Deep venous thrombosis
EDC	1-(3-dimethylaminopropyl)-3-ethylcarbodiimide hydrochloride
EDTA	Ethylenediaminetetraacetic acid
EIS	Electrochemical impedance spectroscopy
ELISA	Enzyme- linked immunosorbent assay
FT	Fourier-transform

FTIR	Fourier-transform infrared spectroscopy
FRS	Framingham risk score
G4	G-quadruplex
Gp 130	Glycoprotein 130
Glu	Glutamic acid
HDL	High-density lipoprotein
HDL-C	HDL - cholesterol
HIV	Human immunodeficiency virus
HRP	Horseradish peroxidase
HRT	Hormone replacement therapy
hs-CRP	High-sensitive C-reactive protein
ICP-MS	Inductively coupled plasma mass spectrometry
IgG	Immunoglobulin G
IL	Interleukin
Kd	Dissociation constant
LDL	Low density protein
LSPR	Localized surface plasmon resonance
MHDA	16-mercaptohexadecanoic acid
MPA	3-mercaptopropionic acid
MUDA	11-mercaptoundecanoic acid
NHS	N-hydroxysuccinimide
NIR	Near-infrared
NO	Nitric oxide
NPs	Nanoparticles
OR	Odds ratio
PBS	Phosphate buffered saline
PC	Phosphocholine
PDI	Polydispersity index
PEA	O-phosphorylethanolamine
Phe	Phenylalanine
PMPC	Poly(2-methacryloyloxyethyl phosphorylcholine)
PMPC-*b*-	Poly(2- methacryloyloxyethyl phosphorylcholine)- b-poly(N-methacryloyl--(L)-tyrosine methylester

PMPC-g-Au NPs	Poly(2-methacryloyloxyethyl phosphorylcholine)-grafted Au NPs
PTS	Post-thrombotic syndrome
QDs	Quantum dots
RNA	Ribonucleic acid
ROS	Reactive oxygen species
SAA	Serum amyloid A
SD	Standard deviation
SELEX	Systematic evolution of ligands by exponential enrichmente
SNP	Single nucleotide polymorphisms
ssDNA	Single-strand deoxyribonucleic acid
SPRi	Surface plasmon resonance imaging
TE	Tris-HCl
TEM	Transmission electronic microscopy
ThT	Benzothiazole dye thioflavin T
TNF-α	Tumor necrosis factor alpha
Trp	Tryptophan
Tyr	Tyrosine
Uv-vis	Ultraviolet - visible
US	United states

Index

Index of figures

Index of tables

1 Work context, objectives and strategy

1 Work context, objectives and strategy

1.1 Work context

Cardiovascular diseases (CVD) are a group of disorders of the heart and blood vessels that are the first cause of death in the world. Biomarkers have been studied for preventing, improving diagnosis and treatment of CVD. C-reactive protein (CRP) is one of the most well-known biomarker and it is used for standard clinical practice for detection of cardiovascular diseases. There is a need of a quickly, portable and low costing in other to prevent CVD. Biosensors may the answer for these desirable requirements for the detection of CVD. The localized surface plasmon resonance (LSPR) band is an optical property of some nanosized metals which is highly sensitive to the surrounding medium. Gold nanoparticles (Au NPs) and LSRP phenomenon could be used for detection of CRP by the development of a biosensor.

Nowadays, for CRP detection is used a system that demonstrate some issues like the utilization of antibodies, a long consumption of time during reaction and a high false-positive ratio. Also, in literature, some of the developed systems showed a complex strategy for materials preparation and do not reach the recommended CRP detection limit value (inferior to pg/mL). According to this, a desirable system should not use antibodies, be highly specific for CRP, be simple to prepare and have short time reactions.

1.2 Objectives and work strategy

The main goal of this work was to investigate novel strategies for the functionalization of colloidal Au NPs that could provide affinity to CRP, aiming the development of a simple, reliable and highly sensitive biosensor for the detection of CRP concentrations based on the optical properties of the Au NPs. To reach this goal two distinct strategies of surface functionalization of gold nanoparticles were investigated: the covalent attachment of cytidine diphosphocholine and secondly, the functionalization of Au NPs with an aptamer specific for CRP.

Having in mind the development of a LSRP sensor for the detection of C-reactive protein using gold nanoparticles, the following objectives must be achieved:

1. Synthesis of gold nanoparticles;

2. Functionalization of gold nanoparticles surface;

3. Use of functionalized gold nanoparticles for detection of CRP.

The present thesis is organized in seven topics. The first section includes the work context, objectives of the work and the strategy used to achieve the goals. The second section is the state of the art that allowed the analysis of current problems in detection of CRP. The third section describes the experimental methodologies namely for the synthesis and functionalization

of Au NPs and CRP detection tests. The results and discussion are presented in the fourth section; the fifth section comprises the main conclusions of the work done and the perspectives of future work to develop a biosensor for CRP detection. The references and supplementary material are included in sixth and seventh section, respectively.

2   Introduction

2 Introduction

2.1 Concern diseases in XXI Century

According to Word Health Organization, in Europe, cardiovascular diseases (CVD) cause more than half of the total deaths caused by acquired immune deficiency syndrome (AIDS or HIV), tuberculosis and malaria combined [1]. In United States (US), cardiovascular diseases are the leading cause of death. Disease Control and Prevention (CDC) presents information about the leading causes of death in 2010, as shown in **table 1**. As could be seen in this table, mortality due to heart disease become first than cancer and diseases caused by microorganisms as influenza and pneumonia [2].

Table 1: Representation of diseases in US and corresponding numbers of deaths in 2011 [2].

Disease	Number of Death in US
Heart disease	596,339
Cancer	575,313
Chronic lower respiratory diseases	143,382
Stroke (cerebrovascular diseases)	128,931
Accidents (unintentional injuries)	122,777
Alzheimer's disease	84,691
Diabetes	73,282
Influenza and Pneumonia	53,667
Nephritis, nephrotic syndrome, and nephrosis	45,731
Intentional self-harm	38,285

CVD are the number one cause of death in the world. It is estimated that 17.5 million of people died from this type of diseases, in 2012, which corresponds to 37% of the entire global deaths. Among these, around 7.4 million of deaths were result of coronary heart disease and approximately 6.7 million were due to stroke [3].

2.2 Cardiovascular diseases and their biomarkers

CVD could be defined as a group of disorders of the heart and blood vessels, including: coronary heart disease (CHD), peripheral arterial disease, rheumatic heart disease, congenital heart disease, deep vein thrombosis and pulmonary embolism [3]. For preventing CVD, European Guidelines on cardiovascular disease prevention in clinical practice 2016 recommend to avoid smoking or stop to smoke, increase physical activity, have a healthy food diet, limit the alcohol consumption, reduce body weight, blood pressure and control blood lipids. These risk factors vary depending on person age, premature CVD in family and occurrence of diabetes, for example, contribute to the calculation of the cardiovascular risk. The increased of cardiovascular risk value, lead to a necessity of have more intense actions in order to prevent a CVD [4]. For the prediction of cardiovascular risk could be used algorithms models, namely Framingham Risk Score (FRS), and

a biological marker, a biomarker [5]. The FRS is a cardiovascular disease model that uses an algorithm for evaluate the 10-year cardiovascular risk of an individual [6]. This risk score accounts for smoking, blood pressure, antihypertensive medication use, total and higher-density lipoprotein (HDL) cholesterol level, diabetes status, age, and gender to predict the 10-year risk for developing CHD [7].

New biomarkers have been investigated in order to prevent, improve diagnosis and treatment of CVD including myocardial infarction, congestive heart failure, and stroke [8]. Biosensors ideally should be accurate, reproducible, safe and cost-effective. Moreover the analysis time must be the most reduced possible [9] and ultrasensitive, capable of detecting trace concentrations of the biomarkers, below $pg.mL^{-1}$, in the case of C-reactive protein [10]. Several biomarkers have been proposed for detection of CVD and can be divided in two groups, non-genetic biomarkers and genetic biomarkers. Recently, the interest for genetic biomarkers has increased because the propensity to develop a CVD could be identified in the genome, aiming to improve the cardiovascular risk prediction [11], one example is 9p21 allele [12]. Non-genetic biomarkers could be associated to: cardiac damage like cardiac troponins and inflammation like interleukin 6, serum amyloid A or pentrameric proteins as C-reactive protein [8]. The 9p21 allele and the inflammatory biomarkers will be discussed in following sub-sections.

2.2.1 9p21 allele

9p21 locus is a non-protein coding region that is carried by 75% of Caucasians and for Asians, and seems to be a coronary artery disease risk factor in these populations [12]. 9p21 region, encodes an antisense non-coding RNA (ANRIL), that seems to be an inhibitor of two cyclin-dependent kinase genes involved in vascular cell proliferation [13]. The hypothesis is that 9p21 is associated to arteriosclerotic cardiovascular diseases due to loss of antiproliferative function. This could be supported for the fact that carriers of 9p21 allele have premature coronary artery disease (CAD) and coronary atherosclerosis. Also, according to literature the allele is related to the initiation of atherosclerosis process [14].

2.2.2 Interleukin 6 (IL-6)

Interleukin-6 (IL-6) is a protein that stimulates and activates macrophages, leading to the formation of foam cells. These foam cells are a type of macrophage that is present in fatty deposits on blood vessel walls, indicating atherosclerosis [15, 16]. The interactions of IL-6 in organism could happens by two ways, IL-6 bind to soluble IL-6 receptor (sIL-6r) and later to a transmembrane glycoprotein 130 (Gp 130) on nucleated cells or, bound to Gp 130 on lymphoid tissue. A study performed by Anderson *et al.* (2013) demonstrated that serum IL-6 levels were higher in patients with acute myocardial infarction (AMI) (11.75 $pg.mL^{-1}$) than in patients without

this disease (1.21 pg.mL^{-1}), and also compared with patients with CAD (2.07 pg.mL^{-1}). The same was observed with sIL-6r that the levels were: 41.340 pg.mL^{-1} for patients with AMI; 27.365 pg.mL^{-1}for patients without AMI and 29.382 pg.mL^{-1} for patients with CAD. No significant differences were observed in Gp 130 in patients with AMI or CAD compared to patients without these diseases [17]. For measurement of IL-6 levels, it was performed a Human IL-6 ELISA Set with a detection limit of $\geq$ 10 ng.mL^{-1}. Also, this assay could have some interferers: human γ-globulin, serum albumin, transferrin and heparin (> 300 U.mL^{-1}) [18].

2.2.3 Serum amyloid A

Serum amyloid A (SAA) is an acute phase family of proteins [19, 20] and its produced by liver during injury, inflammation, stress and infection [20]. High-density lipoproteins (HDL) exhibits a protective role, with higher levels associated to a lower risk of future myocardial infarction. HDL participate in the removal of cholesterol from tissues and cell to liver [21]. Jousilahti *et al.*(2001) referred the hypothesis that SAA might modify the metabolism of high density lipoproteins (HDL), leading to the loss of protective effect of these particles against cholesterol [19]. In 2012, Weichhart *et al.* demonstrate that HDL particles enriched in SAA lead to loss of protective action. Also, altered HDL particles were inversely correlated with its anti-inflammatory strength [22]. This condition could be found in patients with diseases such as CAD [23]. Zewinger *et al.*(2015) evaluate the relationship between the increasing concentration of SAA and HDL-C (HDL-cholesterol) with cardiovascular mortality, in patients undergoing coronary angiography [23]. Cardiovascular mortality is caused by unexpected cardiac death, lethal myocardial infarction, death caused by congestive heart failure, or death immediately after intervention to treat CAD and fatal stroke. Results showed that higher SSA levels were strongly related with cardiovascular mortality and that SSA levels > 16.9 mg.L^{-1} interfere with beneficial vascular properties of HDL-C. Due to endothelial nitric oxide (NO) production decrease, the production of reactive oxygen species (ROS) increases, when SAA levels were higher. Also, HDL-C became a pro-inflammatory particle. However, when SAA levels were not altered, the basal ROS production remains unchanged [23]. The measurement of SAA levels was performed by an immunonephelometry method that uses carboxylated latex particles covalently bounded to fragments of anti-SAA. The detection limit of this method was not referred and the limitations could be the presence of some particles that may interfere with turbidity of the medium [24].

2.3   Human C-reactive protein

Human C-reactive protein (CRP) is a major acute-phase reactant protein produced in liver and it is present in blood plasma. This native protein with a molecular weight of 118 kDa has five non-glycosylated similar subunits of 206 amino acids each (monomer) that are non-covalently (through van der Waals interactions and hydrogen bonding) bonded and that originate a cyclic form [25, 26], represented in **figure 1**. Each monomer is linked to two calcium ions through an electrostatic salt bridge [27].
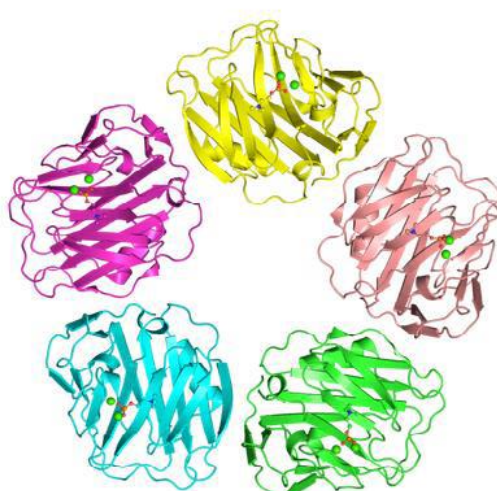
Figure 1: Three dimensional structure of CRP coloured by chain and viewed from the front [28].

Hepatocytes release CRP in response to inflammatory cytokines including IL-6, IL-1 and tumor necrosis factor alpha ((TNF)-α), which are released by leukocytes during infection or tissue inflammation [29]. CRP binds to phosphocholine (PC) and others related molecules expressed on the surface of dead or dying cells and microorganisms, in cause of disease. CRP binds to PC due to the interaction between the phosphate groups of PC and the calcium ions of CRP. Two of the oxygens of the phosphate group interact, each one with one calcium ion, and the third oxygen does not make part of the binding site and could be in ester linkage with other molecules. In this way, one molecule of PC could bind to each of five monomers of CRP. Also, the distance of the positively charged nitrogen of amine to acidic side-chain of Glu81, 3.8 Å, seems to be relevant in PC binding [27].

2.4   High-sensitivity CRP assays

High-sensitivity CRP (hs-CRP) assays have been used in the detection of small variations in CRP concentrations [30]. As reported by Ridker (2004) elevated levels of hs-CRP are directly associated with cardiovascular risk [31] and, high levels of hs-CRP have been associated with a

higher incidence of cardiovascular events in patients with multiple complex plaques [32]. However, hs-CRP apresent poor specificity, since hs-CRP levels are known to be considerably influenced by infection and tissue damage, as well as by obesity, old age, hypertension, diabetes mellitus (DM), smoking [30] and gender. Indeed the co-relation between hs-CRP level and future cardiovascular events is stronger in men than in women [33]. Also, post-menopausal women that take oral hormone replacement therapy using estrogen can have hs-CRP levels increased [34]. Moreover, the appropriate level of this protein also depends on people origins. For example, African patients, average hs-CRP levels are higher than in Caucasian or Hispanic patients and lower for Asian patients [5]. Also, Korean population show much lower hs-CRP levels than Caucasians [35]. Koeing *et al.* (2004) reported that hs-CRP is independent of the Framingham risk score. It was observed that by using both strategies together, the accuracy can be enhanced compared to each approach of measuring alone [36]. The American Heart Association and the Center for Disease Control and Prevention defined that cardiovascular diseases risk are low for a CRP concentration below 1.0 mg.L^{-1}, moderate for a CRP level from 1.0 to 3.0 mg.L^{-1}, and high for concentrations over 3.0 mg.L^{-1}. In a more specific approach, CRP levels <1 mg.L^{-1} show a low systemic inflammatory status, which is desirable; levels between 1 and 3 mg.L^{-1} reflect moderate vascular risk; whereas levels > 3 mg.L^{-1} designate higher vascular risk. **Figure 2** illustrates the relationship between levels of hs-CRP and the vascular risk [5].
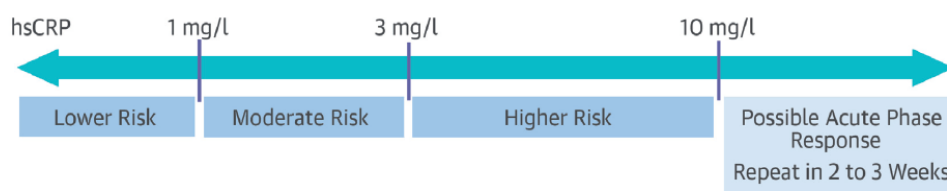
Figure 2: The relationship of inflammation to cardiovascular risk is linear across a wide range of hs-CRP values [5].

For values of hs-CRP superiors to 10 mg.L^{-1}, a transient infectious process or other acute phase response could be occurring and this result needs to be revaluated in 2 to 3 weeks. In the presence of frequent high values, these can be interpreted as a false positive results or a considerably elevated cardiovascular risk [37].

2.4.1 CRP as a biomarker

CRP is used for standard clinical practice [8], is one of the most well-known biomarkers in cardiovascular diseases [38] and is related to the development of numerous cardiovascular diseases like atherosclerosis, hypertension, the occurrence of cardiovascular events (CE), plaque disruption, post-thrombotic syndrome (PTS) and coronary endothelial dysfunction (CED). For that CRP is still an interesting and promising biomarker of cardiovascular diseases [29].

2 Introduction

The function of CRP in initiation and progression of atherosclerosis is still unclear and CRP may contribute for the development of the atherosclerotic lesion leading to acute cardiovascular events [39] however, it was observed in mice that CRP increased transcytosis of LDL across endothelial cell monolayers. LDL transcytosis is a significant component of the initiation of atherosclerosis; these findings strongly indicate the involvement of oxidative stress in atherosclerosis. In this way CRP levels could be associated with the development of atherosclerosis. CRP levels, in this article, was not measured but added 20 $\mu g.mL^{-1}$ for evaluate its presence in the mice organism [40]. CRP is also associated with hypertension, according to a study that evaluate if baseline CRP levels were associated with development of hypertension. From 6312 Taiwan individuals (some with hypertension and diabetes), 145 developed hypertension and it was frequent in older people. Results showed that incidence rates of hypertension by tertile of increasing CRP were 9.3, 19.0, and 33.0 per 1,000 person years (P for trend < 0.01). After adjustments (age, gender, and prehypertension) and using a multivariate model, the CRP baseline continued significantly predictive of incident hypertension [41].

In other article, it was reported that CRP could provide information about the occurrence of the first cardiovascular events (CE) in women. The studied population had 27 939 women and 12% were smokers, 2.5% had diabetes and 25% had a history of hypertension. This study measured baseline levels of hs-CRP and calculate the Framingham Risk Score in studied population who were followed up over a 9-year period. There were performed adjustments for relative risks in FRS. Additionally, as part of the population was taking hormone replacement therapy (HRT) it was not measured hs-CRP levels, because HRT is known to elevate hs-CRP levels. Women taking HRT had more CE than women without this hormone therapy. It was verified that the number of CE increases when hs-CRP levels increases. The same was observed in relation to the prediction of risk of future CE: hs-CRP levels from < 0.5 to 1.0 $mg.L^{-1}$ represent the "low risk" with a prediction of about 1-2 CE; the hs-CRP levels from 3.0 to > 20.0 $mg.L^{-1}$ represent the "high risk" with a prediction of about 2 a 3 CE, after risks adjusted for FRS. Of the total analyzed population, 15.1% had hs-CRP < 0.50 $mg.L^{-1}$, and 5.4% had hs-CRP > 10.0 $mg.L^{-1}$ [42]. It was reported that ruptured plaque at the culprit lesion is associated with elevated levels of C-reactive protein [43] which indicates a poor prognosis in patients with acute coronary syndrome (ACS). In this article authors investigate the relationship between multiple-plaque rupture, CRP and prognosis of AMI, in 45 patients with first AMI. It was observed that 21 patients (47%) had plaque rupture at the culprit site in the acute phase of AMI. These patients demonstrate higher hs-CRP levels (3.1 ± 0.5 $mg.L^{-1}$) when compared with patients without plaque ruptures (1.9 ± 0.4 $mg.L^{-1}$). Also, was verified that hs-CRP levels had a positive correlation with the number of plaque ruptures. This article indicates that hs-CRP may reflect activity

inflammatory processes, leading to plaque rupture in all coronary arteries. Additionally, hs-CRP was suggest not only as biomarker of systemic vascular inflammation but also as a marker of plaque disruption and subsequent thrombosis [44].

CRP gene shows four different single nucleotide polymorphisms (SNP): rs3093077, rs1205, rs1130864, and rs1800947, common variations in populations of European descent. 194 418 participants, of this study, were evaluated in order to relate the genetic variants of CRP gene and the CRP levels with coronary heart disease (CHD). It is important to refer that 46 557 patients had prevalent or incident CHD, the mean age at entry was 59 years old, 89% of participants were European descent and 44% were women. It was observed that variants of CRP were related with baseline C-reactive protein levels. The variations of allele differences in C-reactive protein concentration was: 23% for rs3093077, 19% for rs1205, 14% for rs1130864, and 30% for rs1800947. Also, the different SNPs of CRP were not associated with conventional risk factors or other inflammatory markers. In relation to the risk ratio for CHD was only 1.49 per 1 SD higher "usual" ln C-reactive protein concentration after adjustment of age, sex, and ethnicity. The risk ratio for CHD was 1.33 when adjusted for smoking status, history of diabetes mellitus, and usual levels of systolic blood pressure, body mass index (BMI), non-high density lipoprotein cholesterol, high density lipoprotein cholesterol and triglyceride concentrations. These results indicate that genetically higher concentrations of CRP are not associated with conventional risk factors and risk of CHD. Similarly, the results propose that C-reactive protein concentration is unlikely to be involved in CHD [45].

CRP demonstrates to be a good biomarker of post-thrombotic syndrome (PTS) in patients after an acute deep venous thrombosis (DVT). It was observed, in patients with PTS (12 months after index DVT), that levels of CRP and D-dimer were increased, compared to patients without PTS, as could be seen in results: CRP (median 3.9 mg.L^{-1}) interquartile range ((IQR) [1.6–8.5] vs. 2.4 mg.L^{-1} [1.0–4.3]; P = 0.018) and D-dimer (median 725 ng.mL^{-1} IQR [400–1400] vs. 378 ng/mL [251–652]; P = 0.004). Also, CRP levels had a more significate difference than D-dimer levels. Levels of CRP > 5 mg.L^{-1} in patients were significantly associated with PTS, odds ratio (OR): 8.0 (95% CI: 2.4–26.4; P = 0.001), showed that CRP level were strongly and independently associated with PTS [46]. Recently, was observed that hs-CRP is an independent biomarker of CED in patients with nonobstructive coronary artery disease (CAD). It was observed that patients with a high risk hs-CRP had a lower coronary blood flow (CBF) variation 43.8 ± 6.1% in response to acetylcholine compared to patients with a low risk hs-CRP 65.8 ± 4.5%. Also, it was observed a coronary artery diameter variation (CAd) of -17.2 ± 1.5% in patients with a high risk hs-CRP and -13.1 ± 0.8% for patients with a low risk hs-CRP. After adjusting for traditional risk factors, the percentage CBF variation and CAd variation remained significantly lower in patients with a high

risk hs-CRP -27.1 ± 11.0% and in patients with low risk hs-CRP, -4.5 ± 1.9%. In a multivariate logistic regression model, high risk hs-CRP was associated with CED, OR 1.82 (95% CI: 1.25-2.69). As the inflammation process is severely involved in the development of CED and CRP reflects the inflammatory state of organism, this study proved that are an association between CED and hs-CRP levels [47].

For measurement of CRP levels the authors of the described articles had to accomplish an assay. From all articles described, **table 2** resumes the different assays performed for CRP measurement; this table includes: the detection range, the limitations of method, interferents and detected diseases. Ridker and Cook (2004) [42] and Bouman *et al.* (2012) [46] utilized commercial turbidimetric assay kit, a technique performed by measuring the turbidity in solution. Tanaka *et al.* (2005) [44] analyzed the CRP level through nephelometry assay, a technique similar to the turbidimetric assay. Yet, Chuang *et al.* (2013) [41] used a photometer in other to detect the protein that was not explain in the reference of the method [41].

The analytical methods to assess the hs-CRP levels should be quite sensitive, selective, fast and trustworthy using the lowest sample volume (sensitive analysis of CRP levels in biological samples) [29]. Ideally the method should also be easy to procedure and cheap in order to be widely use in clinical diagnostics for the prevention of severe inflammatory states [48].

2 Introduction

Table 2: Type of assay, detected disease, limitation of the method, interferents, false positives results and the detection limit of the different assay performed for evaluation of the influence of CRP in CVD.; N.m.: Not mentioned.

Type of assay	Detected diseases	Limitation of method	Interferents	Detection limit	Reference
Photometer (smart hs CRP test kit)	Hypertension	N.m.	N.m.	N.m.	[41, 49]
CRP II Latex X2 turbidimetric hsCRP assay	Cardiovascular events	N.m..	Hemoglobin Triglyceride, above not tested concentrations	0.19 mg/L	[42, 50]
N-Latex CRP II,	Multiple plaque ruptures	N.m.	Increased concentrations of serum lipids	0.02 mg/dL	[44, 51]
N-Latex CRP II,	Acute myocardial infection	N.m.	Increased concentrations of serum lipids	0.02 mg/dL	[44, 51]
Turbidimetric assay	Post-thrombotic syndrome	Neonatal samples should not be tested	Hemoglobin, bilirubin, lipemia and rheumatoid Factor in not tested concentrations	0.18 mg/L	[46, 52]
N.m.	Coronary endothelial dysfunction	N.m..	N.m..	N.m.	[47]

2.5 Methods of detection of C-reactive protein

The detection of CRP has been studied by numerous techniques such as enzyme-linked immunosorbent assay (ELISA), turbidimetric assay, electrochemical assay, localized plasmon resonance assay, fluorescence assay and chemiluminescence assay, as examples [29]. These methods should have the ability to detect concentration of CRP below $pg.mL^{-1}$, because CRP is present in a low quantity in biological fluids and in order to detect the disease in an early stage. Amongst the mentioned assays the most used for the detection of CRP is ELISA[10]. In next topics will be discussed the ELISA, turbidimetric assay, electrochemical assay, fluorescence assay and localized surface plasmon resonance assay.

2.5.1 Enzyme-linked immunosorbent assay (ELISA)

Enzyme-linked immunosorbent assay is based on the interaction antibody-antigen complex of C-reactive protein. The commercial kits use indirect ELISA or a sandwich assay, where two distinct antibodies for CRP are used in the trial. First, monoclonal antibodies for CRP are immobilized on wells and establish interactions with free CRP; then, biotin-labelled antibodies are added with the purpose of, interacting specifically with CRP and with streptavidin, because biotin is present. Yet, streptavidin was conjugated with horseradish peroxidase (HRP), for visual detection of the CRP, since tetramethylbenzidine is later added to the reaction medium (a substrate of HRP) [53], allowing the development of a blue colour and lately a yellow colour [54]. The intensity of yellow colour is proportional of the concentration of CRP in the sample and this assay has a detection limit inferior to 10 $pg.mL^{-1}$ [53]. The disadvantage is the necessity of using antibodies that have a higher cost, low stability. In addition, the trial needs a large quantity of sample which is not desirable [10].

2.5.2 Turbidimetric assay

This type of assay uses antibodies for CRP (anti-CRP) for CRP detection in the sample. The anti-CRP reacts with CRP, forming anti-CRP/CRP complex that aggregates, being insoluble and causing turbidity. The turbidity is monitored and it was observed a change in absorbance at 940 nanometers due to formation of the complex that is proportional to the concentration of CRP, in a CRP linear range of 0.02-8.0 $mg.dL^{-1}$. The kit utilized by Bouman *et al* (2012) achieved a limit of detection of 0.18 $mg.L^{-1}$ [55]. Very similar to turbidimetric assay, the nephelometry assay causes turbidity through a complexation reaction between carboxylated latex particles covalently bounded to fragments of anti-CRP [56]. The kit in market for this assay achieved a limit of detection of 0.02 $mg.dL^{-1}$ as in the article performed by Tanaka *et al.* (2005) exemplified. In both articles presented the limit of

detection is superior to the desired ($> pg.mL^{-1}$), for a high sensitive assay and uses antibodies [10].

2.5.3 Electrochemical assay

Electrochemical sensors could be an alternative to ELISA giving the advantage of being a fast, accurate, reliable, and cheap assay; allowing a cost effective electrochemical detection. Electrochemical assays can be divided into amperometric detection, potentiometry and impedimetric spectroscopy (EIS) that could be used in sandwiched immunoassays for detection of CRP [29]. Immunosensors can improve sensitivity making possible detections in a nano-scale range. An example was the development of an electrochemical immunosensor for the detection of CRP which uses a gold electrode where antibodies can bind and generate a response signal. This strategy is also a sandwich-based immunoassay, using a secondary horseradish peroxidase conjugated monoclonal antibody for CRP. The current produced by the HRP reaction is detected by the gold sensor and was conducted using chronoamperometry that allow a good detection limit of 2.6 ng.mL^{-1} [57], but uses antibodies.

2.5.4 Fluorescence assay

Fluorescence assays allow a visual detection of C-reactive protein. The intensity of the fluorescence in the trial is compared to a calibration curve constructed with known concentrations of C-reactive protein, allowing the quantification of CRP in the reaction medium. One of numerous fluorescence assays performed for detection of CRP is an immunofluorescence assay that uses quantum dots as fluorescents probes [58]. Quantum dots are nanocrystals of a semiconducting material with diameters from1 to 10 nanometers of range [59]. Yang *et al*. (2014) developed an assay that uses silica-coated magnetic iron oxide nanoparticles and silica coated CdSe/ZnS quantum dots, both functionalized with antibody for CRP (designated as biofunctional magnetic and fluorescent nanoparticles, respectively). The biofunctional magnetic nanoparticles dispersed in a phosphate- buffered saline (PBS) solution were placed in a microplate well. Then, CRP was added within a range of 10^{-6} to 10^{-16} M and reacted with the antibody for 10 minutes. After the removal of unreacted CRP with PBS solution, biofunctional fluorescent nanoparticles were added to react with CRP for 10 minutes. After the removal of unreacted biofunctional fluorescent nanoparticles, the fluorescence intensity resulting for the assay was measured. The detection limit obtained was 1.0 ng mL^{-1}. The results show that this method exhibited a lower detection limit and a wider linear range than ELISA and other methods [58]. Once again this type of assay uses antibodies.

2.5.5 Localized surface plasmon resonance assay (LSPR)

Localized surface plasmon polaritons (LSPR) involve the propagation of electromagnetic waves in the interface between a metal and adjacent dielectric medium developing a magnetic field. In a metal particle that has a very low diameter compared with the wavelength of the incident radiation, occurs polarization of the electric field, with free electrons of the particles moving in relation to nuclei of the metal particle. This difference in the arrangement of the particle surface charge causes a restoring force, and if the oscillation of conduction electrons is in phase with the electromagnetic incident radiation of a certain frequency, originates a noticeable surface plasmon resonance band in the optical spectrum [60], as **figure 3** illustrates.
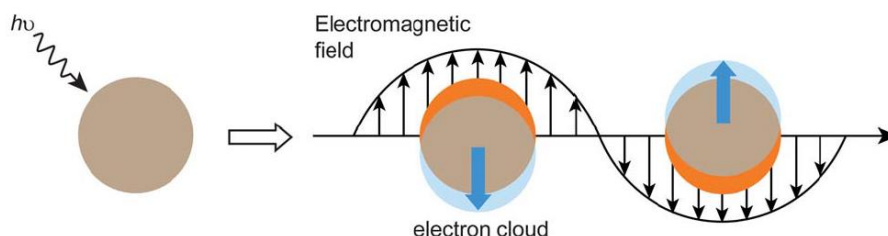
Figure 3: Representation of the oscillation of conduction electrons across the nanoparticle in the presence of an electromagnetic field with incident light [91].

LSPR could be used as a biosensor, and this might be an attractive technology for a sensitive, label-free, and real-time detection of biomolecular targets. This type of sensors has been used for the detection of proteins, nucleic acid and small molecules. However, LSPR assays present low signal intensity and nonspecific binding, which has precluded further application of LSPR in proteomics and disease diagnostics, especially in complex biological samples. To overcome these problems, a variety of amplification approaches has been employed that include the use of gold nanoparticles [61]. Zhang *et al*. (2016) also supported this information reforcing the idea that gold nanoparticles as a noble-metal nanocrystals have been frequently used to improve the sensitivity of biosensors through signal amplification [62]. Several biosensors use LSPR and gold nanoparticles for detection of CRP. **Table 3** resumes the different assays previously described for CRP detection.

Table 3: Example of assays used for the detection of C-reactive protein.

Type of assay	Description/ Example	Detection limit	Reference
ELISA	Uses a sandwich assay and an enzyme reaction for the visual detection of CRP	10 pg.mL^{-1}	[53]
Turbidimetric assay	Uses anti-CRP for complexation with CRP that aggregates being insoluble and causing turbidity that is detected by UV-vis for the detection of CRP	0.18 mg.L^{-1}	[52]
Electrochemical assay	Uses a sandwich assay and an enzyme reaction that is detected by a metal electrode for electrochemical detection of CRP	2.6 ng.mL^{-1}	[57]
Localized surface plasmon resonance assay	Uses gold nanoparticles functionalized with O-phosphorylethanolamine that in presence of CRP show a modification in plasmon resonance peak	50 ng.mL^{-1}	[63]
Fluorescence assay	Uses quantum dots as fluorescent nanoparticles and magnetic nanoparticles functionalized with antibodies for fluorescence detection of CRP	1.0 ng.mL^{-1}	[58]

Different LSPR biosensors for CRP detection are described by Raj and Sreenivasan (2010); Kitayama and Takeuchi (2014); Vance and Sandros (2014); Vashist *et al.* (2015) and Wu *et al.* (2016). All this articles will be clarified in the sections "**2.6.1.Antibody-antigen complex assay**", "**2.6.2.Assays using compounds similar to phosphocholine**" and "**2.6.3.Aptamers assays**", of this document.

2.6 Gold nanoparticles and their advantages in biological applications

Nanoparticles (NPs) are materials with intermediate dimensions between molecules and submicrometer particles that confer them properties distinct from the bulk materials with identical chemical composition due to their small size (range 1-100nm). When the average size of particles diminishes, the surface area to volume ratio increases. For example, a nanoparticle of iron with a diameter of 30 nm contain, 5 % of atoms at the surface, while nanoparticle of a diameter of 3 nm contain, 50% of atoms at the surface [64].

At 1970s, Faulk and Taylor discovered the immunogold labelling that determinated the beginning of biomedical applications of metal nanoparticles, with the use of nanobioconjugates [65]. Consequently, nanostructures have been introduced in a diverse biological applications [66]. Among the varied metal nanoparticles, gold is the most popular material used in functionalized

nanoparticles. The enormous versatility gold-based nanoparticles contributed for their abundant use was showed in this review [67]. Some of these advantages of gold nanoparticles are their chemical stabilities, shape and size controllability [68], higher surface area to volume ratio that could enhance the conductivity of the interface and improve the sensitivity of the analytical system (larger surface might increase the loading amounts and hold the bioactivity of the biomolecules), reproducibility in preparation and easy preparation [69], non-toxicity and biocompatibility that allow their use in biological applications [70].

2.6.1 Gold nanoparticles and Localized surface plasmon resonance

Nanoparticles of gold show significant extinction bands in visible and near-infrared regions [71]. In gold nanoparticles the LSRP bands arise from a resonant phenomenon, with a specific frequency of incident light, as referred [60]. The morphology of gold nanoparticles influence the LSRP bands, in non spherical gold nanoparticles (as gold nanorods) are exhibited two LSRP bands localized in visible and infrared spectrum wavelength due to the possibility of electrons oscillate in a longitudinal and transversal way [72], as represented in **figure 4**.
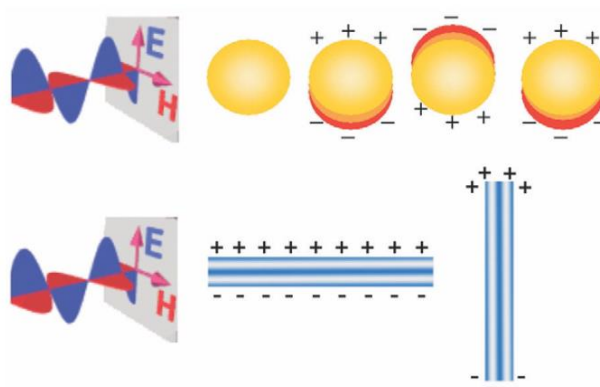
Figure 4: Representation of transversal oscillation of electrons of spherical gold nanoparticle (at top) and transversal and longitudinal oscillation of electrons of a gold nanorod (at bottom) [73].

Colloid gold nanoparticles with spherical shape exhibit one LSRP band and develop color that can range from blue, through orange to red that depends on nanoparticles average size [73]. The increase in particle diameter causes deviations in wavelength, for example, in spherical particles, an increase in the average diameter of 10 to 100 nm origins a red shift of 47 nm [74]. In addition, when the gold nanoparticles approximate from each other to distances comparable to their diameter, the LSPR band displays a red-shift (to high wavelengths) and presents enlargement, as a result of plasmonic coupling. These parameters allow the adjustment of the optical properties of gold nanostructures [75].

These nanoparticles have been used as sensing platforms that exploit the plasmon resonance detection method for bio-specific interaction analysis and biomolecular interaction assays. Unmodified gold nanoparticles with spherical shape and an average size of 39 ± 3 nm have a LSPR peak localized at 520 nm indicating that nanoparticles were well dispersed as individual particles [63]. However, gold nanoparticles (Au NPs), with low average size (< 20 nm) have high surface area-to-volume ratio that causes a propensity to aggregate in solution. Steric stabilization of the particles could be used for enhance colloidal stability, though the use of sterically bulky organic molecules that act as protective shields on the metal surface. This molecules act as charge agents that repel the nanoparticles in solution due to electrostatic stabilization. Even so, in negatively charged Au NPs, aggregation can result from the occurrence of cationic or oligocationic particles [76]. The positive charges that are disturbed in the surface of Au NPs diminish the distance between nanoparticles, provoking aggregation and inducing a shift in the LSPR band into higher wavelengths. This leads to a changing the solution colour from red to blue or purple due to plasmon coupling [77]. **Figure 5** illustrates this colour changing by the presence of an ion that induces Au NPs aggregation, once Au NPs are functionalized with chelating ligands [78].

individual nanoparticle
(red)

ion-mediated assembly
(blue)
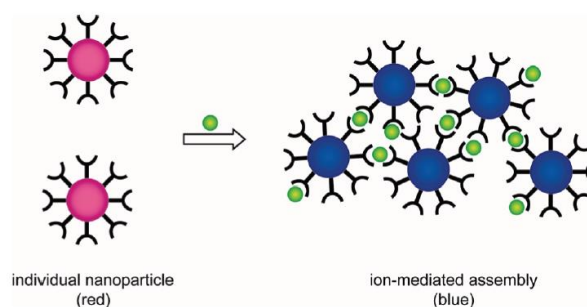
Figure 5: The effect of Au NPs aggregation in colour solution [78].

2.7 Synthesis of gold nanoparticles (Au NPs)

Au NPs can be prepared through "top down" and "bottom up" methods, though each method allows different results in relation to size, shape and characteristics of the nanoparticles. Using "top down" preparation method, Au bulk is broken down by a strong attack force, as ion irradiation in air or arc discharge in water, for producing Au NPs. Those Au NPs can be utilized in suspension, yet for further applications needed to be stabilized; also this method is limited because the control of size, particle size distribution and shape could be difficult. The "bottom up" method implicates wet chemical process like chemical reduction of Au salts, electrochemical pathways and decomposition of organometallic compounds. From these methods, the chemical

reduction is the easiest to prepare stable colloidal Au NPs with desirable sizes and shapes [79].

The synthesis of colloidal gold nanoparticles usually involves two-steps: nucleation and successive growth. The formation of the nucleus occurs by reduction of gold salt with reducing agent **(1)** and the collision between ions, atoms and clusters **(2)** as represented in **figure 6** [79].
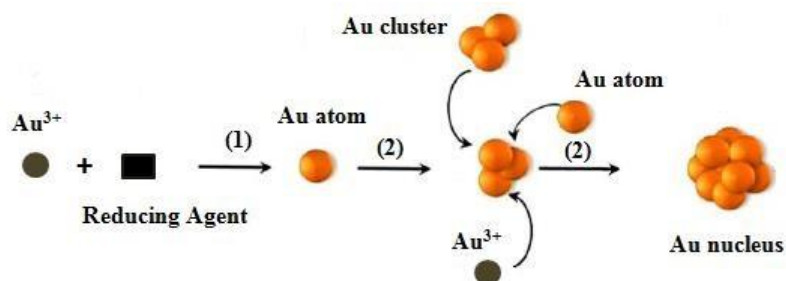
Figure 6: Process of nucleation for synthesis of Au NPs by chemical reduction method [79].

It is named *in situ* synthesis, if the nucleation and successive growth are finished in the same process; otherwise it is termed seed-growth method [80]. The size and shape-controlled growth of these nanoparticles depends on reaction conditions such as concentration of reactants, temperature, incubation time, pH and others, during successive growth. The most common shape of these nanoparticles is spherical shape, which requires isotropic growth on the surface of Au nuclei or particles. Even so, Au NPs can be synthesized into triangle, rod, cube, star, wire, and flower shape because the growth rate varies with direction, corresponding to an anisotropic growth [81, 79].

Currently, there are different approaches for the synthesis of spherical, triangle, rod, cube, star and other shapes of Au NPs [79]. The first methods were developed by Faraday, Turkevich and Brust [82, 83]. Synthesis of colloidal gold in a two-phase system was presented by Faraday, in 1857 by reduction of tetrachloroaurate solution by phosphorus in carbon disulphide [71]. Contrarily, Turkevich created a single phase aqueous method based on the reduction of a gold salt by citrate. This process was improved a few years later by Frens, which produced almost spherical particles over a tunable range of sizes [84]. Lately, the Schiffrin group, in 1994, reported the convenient Brust-Schiffrin biphasic method of thiolate-stabilized Au NPs [82]. These methods correspond to *in situ* synthesis; other approaches proposed by these researchers appeared later. The seed-growth method is one of them [85] and most recent approaches uses polymers [86], dendrimers [87] and include the synthesis of bimetallic Au NPs [85].

2.7.1 Turkevich method

Turkevich developed a single phase aqueous method that uses trisodium citrate as a reducing and stabilizing agent. The chloroauric acid ($HAuCl_4$) solution is taken to boil under

vigorous stirring, then trisodium citrate dehydrate is quickly added to HAuCl$_4$ solution. A red-wine solution is achieved, a few minutes later, due to the formation of Au NPs negatively charged with an average size of approximate 20 nm [88]. **Figure 7** resumes the procedure of Turkevich method [80]. The size of the nanoparticles can be adjusted by modification of the citrate/Au^{3+} molar ratio. At high citrate/Au^{3+} molar ratio, the nucleation is dominant, thus leading to the formation of small size Au NPs. If, the citrate/Au^{3+} molar ratio is low leads to formation of large size Au NPs [89]. Frens proved that by lowering the citrate/Au^{3+} molar ratios obtaining monodisperse Au NPs with an average size of 100 nm [84]. Recently, the Turkevich method was successfully used to produce monodisperse Au NPs with an average diameter smaller than 10 nm by simply reversing the order of addition of the reactants. Thus, instead of adding citrate to boiled chloroauric acid, the HAuCl$_4$ solution was added to the citrate solution, which is favorable for nucleation and stabilization of Au NPs [90]. Despite the electrostatic stabilization, citrate-stabilized particles obtained using the Turkevich method can aggregate during storage or subsequent functionalization steps. Large molecules such as Tween 20 for instance can be used to functionalize, and prevent the aggregation of Au NPs [91].
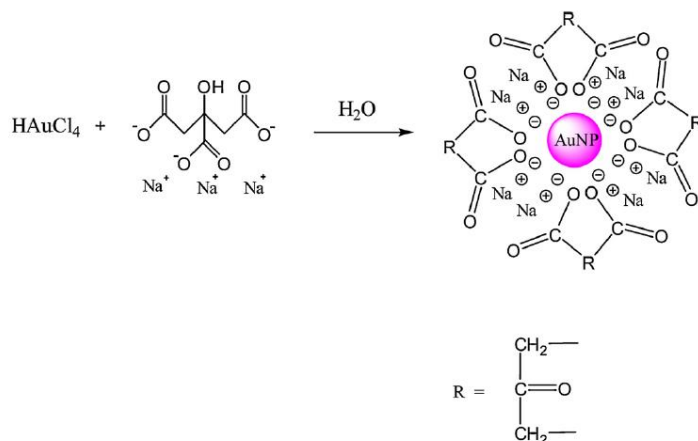
Figure 7: Representation of Turkevich method.

2.7.2 Seed-growth method

Compared to the "in situ" synthesis, the seed-growth method expands the size of the particles step by step, controlling easily the size and shape of Au NPs; becoming one of the most used methods for Au NPs preparation nowadays [80]. In the seed-growth method, firstly seeds are prepared; secondly, these seeds are added to a HAuCl$_4$ solution with stabilizing and reducing agents. These reducing agents reduce Au^{3+} to Au^0 in presence of Au seeds and the recent Au^0 can assembly on the surface of Au seeds. As the second step uses mild reducing agents, this step is slower than the first one, and could be repeated until the Au NPs have the desired size [85].

Depending on the amount and the nature of the reducing agent and stabilizer (e.g. surfactants), and their ratio to the Au precursor; size, shape and surface properties are regulated [85].

2.8 Materials used for surface modified gold nanoparticles for CRP detection

As reported in literature gold is a material widely used for detection of CRP. Different assays can be used for developing a CRP biosensor as the interaction between antibody-antigen complex of CRP functionalized Au NPs or on a gold surface, the most common assay, known as ELISA [92, 93, 94]; also Au NPs can be functionalized with compounds similar to phosphocholine for detection of CRP [95, 96, 63]; and aptamers that are ssDNA or RNA that can bind to pre-selected targets including proteins with high affinity and specificity [97, 98, 61].

2.8.1 Antibody-antigen complex assay

Previously, in the **section 2.5.1**, the classical immunoassay (ELISA) for detection of CRP was described. Yet, in literature we can find several variations in this type of assay, using gold materials. Mishra *et al.* (2014) performed a trial using the CRP antibody covalently immobilized on a platform composed by an electrochemically deposited 3-mercaptopropionic acid-capped gold nanoparticles Au(MPA)-polypyrrole nanocomposite film. The nanocomposite contained free pendant carboxylic groups that are used for specific covalent binding of CRP antibody via carbodiimide coupling, which resulted in a detection limit of CRP of 19.38 ng.mL^{-1} [94].

Similarly, Chammem *et al.* (2015) used gold labelled functionalized magnetic beads for detection of CRP. For antigen immobilization, authors developed modified gold electrode with carboxylated magnetic beads that was activated with a solution of N-(3 dimethylaminoproyl)-N-ethylcarbodiimide hydrochloride (EDC) and N- hydroxysuccinimide (NHS). The difference between the value of electrode resistance without antigen and the electrode resistance after antigen binding, allow the detection of CRP. This method had a detection limit of 0.1 pg.mL^{-1} antigen [99]. In another work, a KOH-treated gold (Au)-coated SPR chip was modified with 1-ethyl-3-(3-dimethylaminopropyl)-carbodiimide hydrochloride (EDC)-activated protein A/G in 3-aminopropyltriethoxysilane (APTES). For detection of CRP, the Pr A/G functionalized Au SPR chip was bound to CRP antibody and blocked with bovine serum albumin. The detection limit was 1.2 ng.mL^{-1} [100].

2.8.2 Assays using compounds similar to phosphocholine

Some approaches use compounds similar to phosphocholine, once, CRP binds to phosphocholine (PC) naturally in human organism, on the surface of dead or dying cells and microorganisms, as referred [27]. Iwasaki *et al.* (2014) have synthetized Au NPs thiol-terminated biomimetic block copolymer, a poly(2- methacryloyloxyethyl phosphorylcholine)- b-poly(N-

methacryloyl-(L)-tyrosine methylester) (PMPC-*b*-PMAT), using a new technique for the synthesis of highly stable gold nanoparticles. The surface of PMPC-*b*-PMAT-protected Au NPs has a dense hydration layer with an elevate number of PC groups. The PC binding site was located at a hydrophobic pocket of CRP, where established interaction with two coordinated Ca^{2+}. Allowing this interaction is phenylalanine (Phe)-66 and glutamic acid (Glu)-81 residues that mediate the binding of PC to CRP [95]. Other authors used poly(2-methacryloyloxyethyl phosphorylcholine) (PMPC) for the detection of CRP and prepared poly(2-methacryloyloxyethyl phosphorylcholine)-grafted Au NPs (PMPC-g-Au NPs). The authors investigated and evaluated the detection of CRP through UV-vis in a buffer solution. These researchers also tested the influence of the albumin in this system and obtained a detection limit of approximately 50 ng.mL^{-1} [101].

Gold nanoparticles functionalized with O-phosphorylethanolamine (PEA) have been also investigated for the detection of CRP in biological samples [96, 63]. PEA and PC are structurally and chemically similar, both having a phosphate group bound to a hydrocarbon chain with an amine as shown is **figure 8.** The difference is the presence of methyl substituents in the amine group in CP, thus being a tertiary amine, which are not present in PEA which has a primary amine [102, 103].
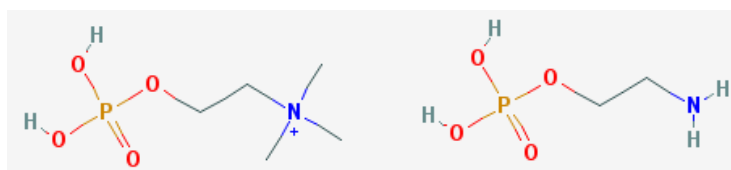
Figure 8: Representation of CP (left) and PEA (right) [102, 103].

Raj and Sreenivasan (2010) functionalized Au NPs using 16-mercaptohexadecanoic acid (MHDA). The thiol group of MHDA interacts with the Au surface of Au NPs, which were synthetized using the Turkevich method. MHDA can be linked to PEA, via the carbodiimide linkage using 1-ethyl-3-(3-dimethylaminopropyl)-carbodiimide hydrochloride (EDC) that allow covalent linkage between activated carboxylic acid groups of MHDA and amine groups of PEA. CRP binds to PEA because of their structural and chemical similarities to CP. This method allowed a detection limit of detection limit of 50 ng.mL^{-1} [63]. Similar, Islam and Kang developed a system using also, Au NPs and PEA, but utilizing luminol-H_2O_2 for fluorescence detection. In this system unmodified Au NPs were placed in a NaCl solution with PEA and luminol-H_2O_2. Au NPs interact with PEA, instead of interacting with NaCl, which leads to a non-aggregation of Au NPs and a weak fluorescence emission was observed. When CRP is present, a CRP/PEA complex is formed. This complex was added to Au NPs and because PEA interacts strongly with CRP, no

interaction between PEA and Au NPs was observed. Consequently, unmodified Au NPs were available to contact with NaCl in solution, resulting in aggregation and the development of strong fluorescence emission; this system allowed a detection limit of 1,88 fM [96].

2.8.3 Aptamers assays

In 1990 the first aptamer was reported, and since then, it has been attracted attention in several applications for analytical methods [98]. Aptamers are target specific ssDNA, RNA or peptide sequences generated by a randomized library of molecules that includes three steps: complex formation, separation and amplification. Systematic Evolution of Ligands by Exponential Enrichment, SELEX, generate aptamers by incubation of initial target and library molecules (a random single-stranded DNA or RNA pool), under appropriate conditions to make complex formation. Before, uncomplexed molecules are separated using a separation method and bound molecules are amplified for subsequent round of selection. [104, 105]. Aptamers can be easily modified or linked with other molecules and have higher specificity. Compared to antibodies, aptamers have diverse advantages, such as: they are easy to prepare and modify, cheaper, have no batch variations, stable and non - immunogenic; also can be incorporated in different fields, and in applications involving therapeutics and diagnoses. Consequently, aptamer-based assay could be a possible substitute for antibody-based assay [104], or aptamers and antibody- based assays could be combined together [61]. Wei *et al.* (2007) reported an aptamer-based colorimetric assay for the detection of thrombin, where the aptamer interacted with unmodified Au NPs. The unfold aptamer (named TBA) is an ssDNA that demonstrate flexibility, which allows to be sufficiently uncoil to expose its bases, that permit the attraction between bases of TBA and Au NPs citrate negative groups through van der Waals forces. TBA is specific for thrombin, and when thrombin is present in the aqueous medium the complex Au NPs/TBA dissolves and the complex TBA/ thrombin is formed thought a G-quadraplex/duplex structure [97]. A similar system was used for the detection of CRP, with G-rich aptamer. The aptamer 6h-62-40 forms a G-quadraplex structure with benzothiazole dye thioflavin T (ThT), showing higher florescence in the absence of CRP. When CRP is present, the complex aptamer/ThT will be disrupted by formation of aptamer/CRP complex, the ThT is drifted away, and consequently, the solution exhibited weak fluorescence. The intensity of fluorescence was inversely proportional to the concentration of CRP, and for high concentrations of CRP, a weak fluorescence is shown, **figure 9**. This fluorescence method had a detection limit of 380 pM [98].
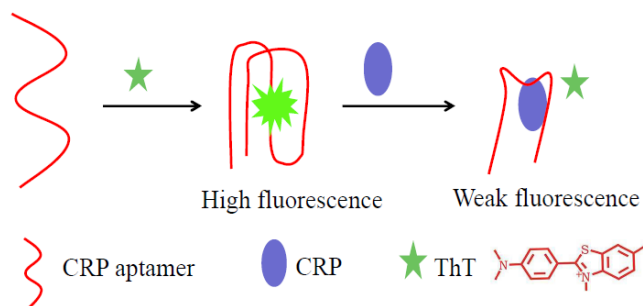
Figure 9: Illustration of a system for detection of CRP using G-rich aptamer and benzothiazole dye thioflavin T (ThT) [98].

High affinity DNA aptamers against C-reactive protein (CRP) were used for the construction of an Au nanoparticle enhanced LSRP biosensor, based on aptamer-antibody sandwich assay. The DNA aptamers were selected using a microfluidic chip, and were immobilized on the Au surface to perform the SPR biosensor. In the presence of CRP, the immobilized aptamers retains CRP on the Au film by specific binding. Lately, the signal was amplified after the addition of anti-CRP coated Au NPs. In this article, the authors have investigated three different approaches of direct measurement, aptamer-antibody sandwich measurement and Au NPs enhanced aptamer-antibody sandwich measurement. The last one demonstrated the lowest detection limit, 10 pM [61]. In another study, that used a surface plasmon resonance imaging (SPRi) aptasensor, researchers were able to detect CRP at lower concentrations. They developed an ultrasensitive SPRi-based nano-aptasensor for the detection of CRP (5 fg.mL^{-1}) in spiked human serum. The SPRi-based nano-aptasensor was composed by gold-coated chip that provides place for attaching the capture probe and extravidin was chosen as direct chemical linker to the capture probe. To avoid non-specific interaction with serum proteins, the salt concentration was elevated to 250 mM and was built a sandwich based assay that uses CRP-specific aptamer coated NIR (near infrared) quantum dots (QDs), for amplifying the signal. However, the mechanism behind NIR QDs SPRi signal enhancement is not well understood. Yet, this work has shown the capability of SPRi sensors to detect CRP in low concentrations [10]. **Table 4** resumes the different materials used for surface modification of gold nanoparticles aiming the detection of CRP, in antibody-antigen assay, assays that use compounds similar to phosphocholine and aptamer assays.

2 Introduction

Table 4: Resume of different assays performed of the detection of CRP, using gold nanoparticles.

Type of Assay	Description	Detection limit	Reference
Antibody-antigen assay	CRP antibody covalently immobilized on a platform composed by an electrochemically deposited 3-mercaptopropionic acid-capped gold nanoparticles	19.38 ng.mL^{-1}	[94]
	Gold electrode modified with carboxylated magnetic beads that was activated with N-(3 dimethylaminoproyl)-N-ethylcarbodimide hydrochloride and N-hydroxysuccinimide (NHS), that interacts with antibody of CRP	0.1 pg.mL^{-1} antigen	[99]
	KOH-treated gold (Au)-coated SPR chip was modified with 1-ethyl-3-(3-dimethylaminopropyl)-carbodiimide hydrochloride (EDC)-activated protein A/G in 3-aminopropyltriethoxysilane (APTES) bound to antibody of CRP	1.2 ng.mL^{-1}	[100]
Similar coumponds to phosphocholine assay	Surface functionalization of Au NPs with poly(2-methacryloyloxyethyl phosphorylcholine)- b-poly(N-methacryloyl-(L)-tyrosine methylester) (PMPC-b-PMAT)	20-40 nM	[95]
	Poly(2-methacryloyloxyethyl phosphorylcholine)-grafted Au NPs (PMPC-g-Au NPs)	50 ng.mL^{-1}	[101]
	Au NPs were functionalized with 16-mercaptohexadecanoic acid (MHDA), which is covalently linked with PEA., that interacts with CRP	50 ng.mL^{-1}	[63]
	System using Au NPs and PEA, but utilizing luminol-H$_2$O$_2$ for flourescence emission	1,88 fM	[96]
Aptamers assays	High affinity DNA aptamers were used for the construction of an Au nanoparticle enhanced SRP biosensor, based on aptamer-antibody sandwich assay	10 pM	[61]
	Ultrasensitive SPRi-based nano-aptasensor for detection of CRP	5 fg.mL^{-1}	[10]
	Aptamer-based method using G-quadruplex/duplex structure with benzothiazole dye thioflavin T (ThT) for CRP detection	380 pM	[98]

2.9 Current problems in assays for the detection of CRP

The most used technique for detection of CRP, ELISA, provides a good sensitivity method (pg.mL^{-1} or fg.mL^{-1}) [10] and are used as a kit test [106]. However, this technique presents some drawbacks, namely: it involves large quantities of sample; it uses antibodies which usually

have low stability, needs specific chemical medium conditions; it involves high production costs [106], it requires long reaction time [100], it requires trained professionals and expensive reagents [94] and it has a relative high false-positive rate due to non-specific binding [106]. On the other side, the strategies reported by Chammem *et al*. (2015) [99] and Wu *et al*. (2013) [98] do not have a detection limit lower below to pg.mL^{-1}, which compromises the evaluation of the disease developed by the patient [10]. Other studies show very complex strategies, involving too many steps for performing the trial as described by Vashist *et al*. (2015) [100] and Wu *et al*. (2016) [61], becoming a time-consuming process. It is also important to note that some of the studies reported do not test the CRP detection in biological samples and consequently do not take in consideration the presence of all blood proteins that could interfere in CRP detection.

2.9.1 Proteins that could interfere in detection of C-reactive protein

Alterations in the concentration of fractions or total proteins in blood could indicate development of disease and blood analysis allows clinical diagnosis. The proteins presented in blood are distributed into two groups: albumins and globulins. Albumin is the most abundant protein, constituting more than fifty percent of all blood proteins. Globulins are divided into three forms: beta, alfa and gamma or immunoglobulin [107] like immunoglobulin G (IgG) [99]. Other proteins also present in blood are: cytochrome C [96], hemoglobin, myoglobin, transferrin [61], human fetuin A, human lipocalin 2, interleukin-1β, IL-6, IL-8 and tumor necrosis factor ((TNF)-α) [100]. IL-6 [11] and (TNF)-α [8] and SAA [23] are used as biomarker for CVD detection. The blood proteins described were used to confirm the specificity of the strategy used for detection of CRP: Islam and Kang (2011) confirmed the accuracy of their results using albumin and cytochrome C as controls [96]; Wu *et al*. (2013) used transferrin, myoglobin, albumin; hemoglobin and IgG for testing the selectivity of their system [98]; Chammem *et al*. (2015) utilized IgG to confirm specific interaction with antigen (CRP) and used albumin in their strategy avoiding its detection [99]; yet, Vashit *et. al* (2015) tested the specificity of their system using albumin, fetuin A, lipocalin 2, IL-6, IL-8, IL-1β and (TNF)-α [100] and Wu *et al*. (2016) used five proteins to investigate the selectivity of the assay, these proteins being albumin, hemoglobin, myoglobin and transferrin [61].

3   Experimental section

3 Experimental section

3.1 Materials

The reactants tetrachloroauric (III) acid trihydrate (HAuCl$_4$.3H$_2$O, ≥99.9%), sodium citrate tribasic dihydrate (Na$_3$C$_6$H$_5$O$_7$.2H$_2$O, ≥99.0%), 11-mercaptoundecanoic acid (C$_{11}$H$_{22}$O$_2$S, 95%), 3-mercaptopropionic acid (C$_3$H$_6$O$_2$S, ≥99%), cytidine 5'-diphosphocholine sodium salt dihydrate from yeast (C$_{14}$H$_{25}$N$_4$NaO$_{11}$P$_2$.2H$_2$O, (~98%)), C-reactive protein from human plasma, Trizma Base (C$_4$H$_{11}$NO$_3$, ≥99.9%) and sodium phosphate dibasic (Na$_2$HPO$_4$ ≥99.0%) were purchased form Sigma-Aldrich. 1-(3-dimethylaminopropyl)-3-ethylcarbodiimide hydrochloride (CH$_3$CH$_2$N=C=N(CH$_2$)$_3$ N(CH$_3$)$_2$.HCl, EDC, >98%) was acquired in Alfa Aesar. (Ethylenediamine)tetraacetic acid (HO$_2$CCH$_2$)$_2$NCH$_2$CH$_2$N(CH$_2$CO$_2$H)$_2$, (EDTA, 99.5%), calcium chloride (CaCl$_2$, 97%) and sodium chloride (NaCl, >99.5%) were purchased from PanReac. The aptamer, an oligonucleotide (single strand DNA - ssDNA) specific for C-reactive protein: 5'-CGA AGG GGA TTC GAG GGG TGA TTG CGT GCT CCA TTT GGT G-3', with a molecular weight of 12495.2 g.mol^{-1} and a molar extinction coefficient of 383500 M^{-1}.cm^{-1} was acquired in Eurogentec. All the reactants were used without further purification.

3.2 Synthesis of Au NPs

3.2.1 Synthesis of Au NPs *via* the Turkevich method

The synthesis was performed following a procedure reported in the literature [63]. Typically in a round-bottom flask of 250 mL 92.47 mL of Milli-Q water was heated until 85ºC, under reflux. Then 2.54 mL of 10.01 mM HAuCl$_4$ solution was added while stirring (300 rpm). Afterwards, 1.73 mL of 98.04 mM sodium citrate solution and 3.27 mL of Milli-Q water were added. The solution reacted for 30 minutes at 91ºC, under stirring and afterwards was left to cool until reach room temperature (**figure 10 a)**).

3.2.2 Synthesis of Au NPs *via* the seed-growth method

The synthesis via the seed-growth method was performed following a procedure reported in the literature [108]. In this method, the seeds (Au nanoparticles with an average size of 15 nm) are firstly prepared using a procedure based on the Turkevich method. Thus, in a round-bottom flask of 250 mL, 45 mL of Milli-Q water was brought to boil under reflux. Then, 4.99 mL of 10.01 mM HAuCl$_4$ was added under stirring (300 rpm). Afterwards, 5.09 mL of 39.50 mM sodium citrate solution was added and the solution was left to react until the solution colour was red-wine (**figure 10 b1)**).

The next stage consists on the growth of the Au seeds previously prepared. Thus, 121.89 mL of Milli-Q water was brought to boil under reflux, in a round-bottom flask of 250 mL. After, 3.12 mL of 10.01 mM HAuCl$_4$ was added under reflux and stirring (300 rpm), at 85ºC.

Afterwards 1.13 mL of the previously prepared AuNPs (15 nm) was added, followed by the addition of 0.57 mL of 39.50 mM sodium citrate solution. Immediately the colour of the solution changed for a purple to pink. The solution reacted for 30 minutes and afterwards, 5.09 mL of 39.50 mM sodium citrate solution was added. The solution reacted for 1h further (**figure 10 b2)).**

Synthesis of Au NPs_10 nm and Au NPs_40nm:
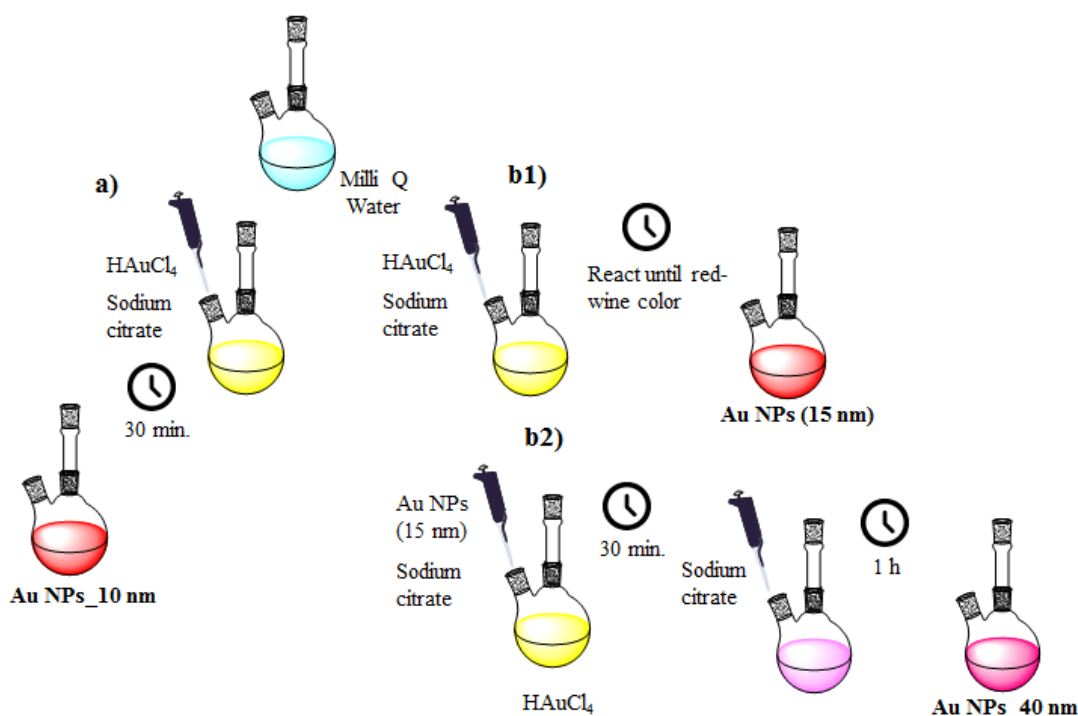
Figure 10: Schematic illustration of synthesis of bare Au NPs.

3.3 Determination of Au NPs concentration

3.3.1 Determination of Au NPs concentration based on LSPR

The concentration of Au nanoparticles was estimated from the visible spectrum of the Au colloid using a method previously reported [109]. First the average particle size was estimated from the ratio between the absorbance of the LSPR (localized surface plasmon resonance) band and the absorbance at 450nm (A_{LSPR}/A_{450nm}). Through this ratio it was possible to estimate the molar extinction coefficient [109]. Then, using the Lambert Beer Law, the concentration of gold nanoparticles was determined:

(1) $$A = \varepsilon . b . C$$

3 Experimental section

In **equation 1**, A is the absorbance of Au NPs colloid at 450 nm, ε is the molar extinction coefficient at 450 nm ($M^{-1}cm^{-1}$), b the path length of the sample expressed in centimetres and *C* the concentration of gold nanoparticles (M).

3.3.2 Determination of Au NPs concentration using chloroauric acid concentration

In this strategy it is assumed that all gold Au^{3+} from chloroauric acid is converted into Au^0 in the form of nanoparticles:

$$1 \text{ mol } HAuCl_4 \rightarrow 1 \text{ mol of } Au^{3+} \rightarrow 1 \text{ mol of } Au^0$$
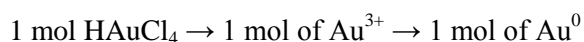
The diameter used for calculation of Au^0 concentration was 10.3 nm and 38.2 nm, for Au NPs synthetized via Turkevich and seed-growth method, respectively.

3.4 Determination of aptamer concentration

The aptamer concentration was determined measuring the optical density, i.e. absorbance, at 260 nm, using a UV-vis spectrophotometer. According to the aptamer fabricator, 1 optical density of ssDNA at 260 nm corresponds to a concentration of 33μg/mL.

3.5 Surface functionalization of Au NPs

3.5.1 Surface functionalization of Au NPs with MUDA

Citrate-capped gold nanoparticles synthetized using the Turkevich method and the seed-growth method were both functionalized using 11-mercaptoundecanoic acid (MUDA). MUDA is only partially soluble in water, with a solubility at 25ºC of 13.8 mg/L (6.32×10^{-5} M) [110].

The procedure used for surface modification was adapted from literature [111]. For the smallest Au NPs, obtained via Turkevich method, the Au NPs/MUDA molar ratio used was 256.7. Thus the surface modification was performed by adding 243 μL of MUDA solution (4.28×10^{-5} M) to 10 mL of Au NPs colloid (2.67×10^{-4} M). The colloid was used as prepared and no centrifugation was performed in Au NPs colloid prior the functionalization with MUDA. For the surface modification of largest Au NPs, synthetized via seed-growth method, the Au NPs/MUDA molar ratio was 9483.9. Thus 14.5 μL of MUDA solution (4.28×10^{-5} M) was added to 20 mL of 2.94×10^{-4} M Au NPs colloid. In both cases the resulting solution was equilibrated at 25ºC and left to react 15h30 min., under stirring (100 rpm). Unreacted reagents were removed by centrifugation at 13300 rpm (smallest Au NPs) and 6000 rpm (largest Au NPs), during 10 and 15 minutes, respectively and were resuspended in the same volume of water. These nanoparticles will be named as Au NPs@MUDA. **Figure 11** illustrates the functionalization.

3.5.2 Surface functionalization of Au NPs with MPA

For the surface functionalization with MPA the Au NPs/MPA molar ratio was 0.144 and the pH of MPA solution was adjusted to pH 5.10 (**appendix A1**).

Thus Au NPs synthetized via Turkevich method, were functionalized with MPA, by adding 578μL of MPA solution (0.032M) to 10 mL of 2.67×10^{-4}M Au NPs. Identically, Au NPs synthetized using seed-growth method were functionalized with MPA by adding 638 μL of MPA solution (0.032M) to 10 mL of Au NPs 2.94×10^{-4}M. In both cases the reaction was performed for 2 h, under magnetic stirring (150 rpm) at 25ºC. After functionalization, unreacted reagents were removed by centrifugation at 13300 rpm for 10 min (smallest Au NPs) and at 6000 rpm for 15 min (largest Au NPs) and were resuspended in the same volume of water [112]. The designation of these nanoparticles will be Au NPs@MPA. **Figure 11** summarizes the functionalization procedure.
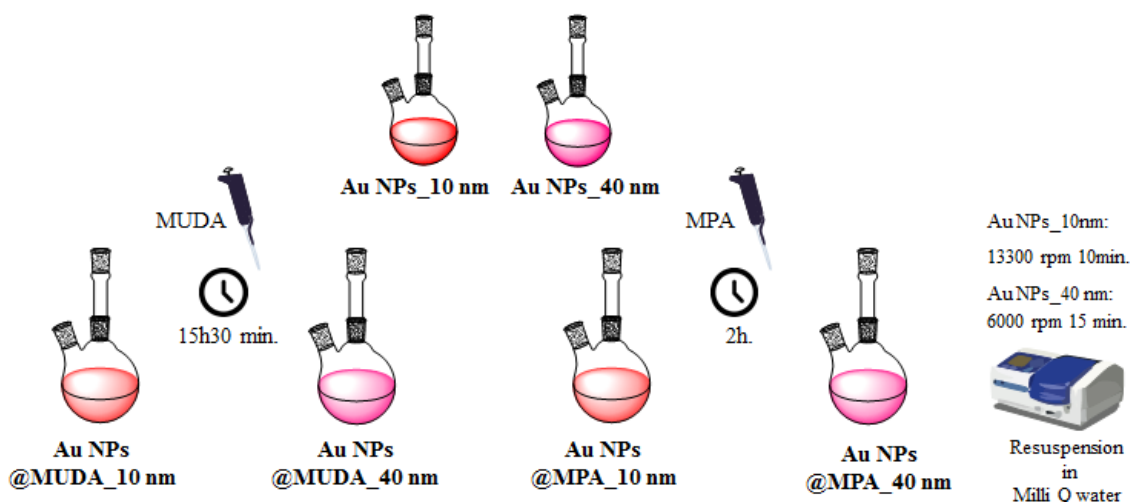
Figure 11: Schematic illustration of Au NPs functionalization with MPA or MUDA.

3.6 Bioconjugation of Au NPs with CDP

Gold nanoparticles functionalized with MUDA and MPA, were then conjugated with cytidine 5' diphosphocholine (CDP). CDP was covalently linked to the surface of Au NPs using 1-(3-dimethylaminopropyl)-3-ethylcarbodiimide hydrochloride (EDC). For bioconjugation with CDP to the Au NPs functionalized with MUDA or MPA was added the molar number of CDP of 10-fold molar excess to the molar number of MUDA in Au NPs 40 nm, used as reference for the bioconjugation of surface modified MPA or MUDA Au NPs. Also, EDC was added in 10-fold molar excess over CDP (**table 14** and **figure 47**, **appendix A4**). In a typical procedure, 59.6 μL of 10^{-4}M EDC aqueous solution was added to 1 mL of MUDA/MPA functionalized Au NPs, followed by 56.5 μL of 10^{-5}M CDP solution. This protocol was adapted from the literature [63, 113].

The reagents (EDC and CDP) were added under vigorous stirring at 400 rpm during 10 minutes and then left to react for 2 h at 25ºC. The unreacted reagents were removed by centrifugation at 6000 rpm for 15 minutes, in the case of AuNPs_40nm and 10 minutes at 13300 rpm for AuNPs_10nm. The gold nanoparticles conjugated with CDP (AuNPs@MUDA@CDP and AuNPs@MPA@CDP) were resuspended in 1 mL of Milli-Q water. In **figure 12** this functionalization is represented.
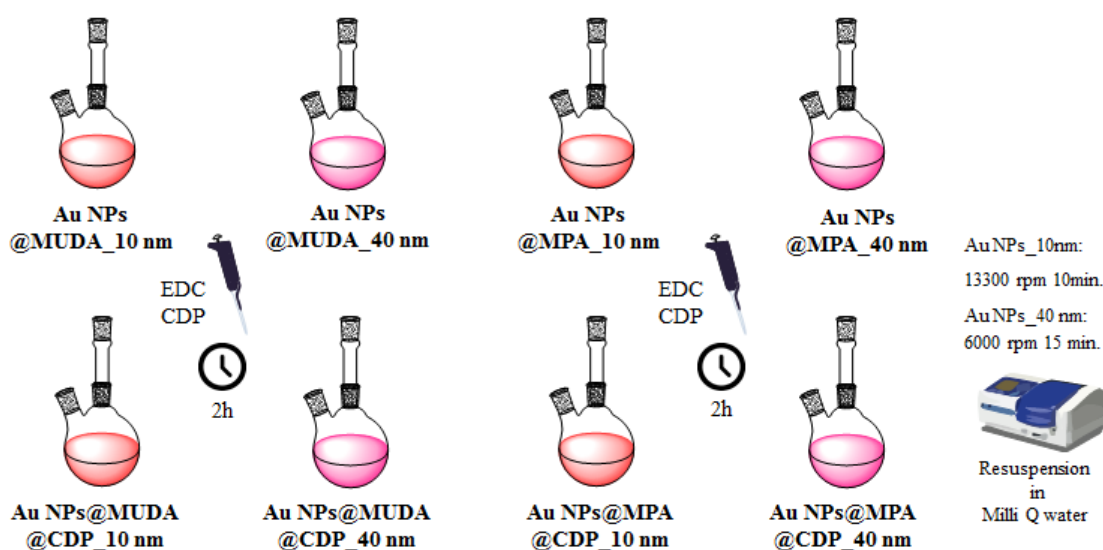
Figure 12: Schematic representation of Au NPs bioconjugation with cytidine diphosphocholine.

3.7 Bioconjugation of Au NPs with the aptamer

The aptamer was resuspended in a TE buffer solution (11.0 mM Tris-HCl, 0.214 mM EDTA) at pH 7.42, as recommended by the aptamer fabricant. Following a procedure adapted from the literature [114, 115, 116] the aptamer was firstly kept at 75ºC for 10 min to promote the unfold state and then at room temperature for 30 minutes. Then 2.4 mL of AuNPs_13 nm colloid as prepared was added to 720 μL of aptamer solution 19.7 μM. The mixture reacted for 48 hours at room temperature and under stirring at 150 rpm. After, the solution was centrifuged at 13300 rpm during 10 minutes and the pellet of Au NPs@ssDNA was resuspended in 3.12 mL of TE buffer. Then 177 μL NaCl (1.01 M) and 2 μL KCl (0.103 M) solution were added to 1.25 mL of Au NPs@ssDNA and the mixture was allowed to react for 30 minutes at 23ºC and 150 rpm following a procedure adapted from literature [117, 97] (See **figure 13**).The resultant solution was used for CRP detection trials.

3 Experimental section

Synthesis of aptamer surface modified Au NPs:
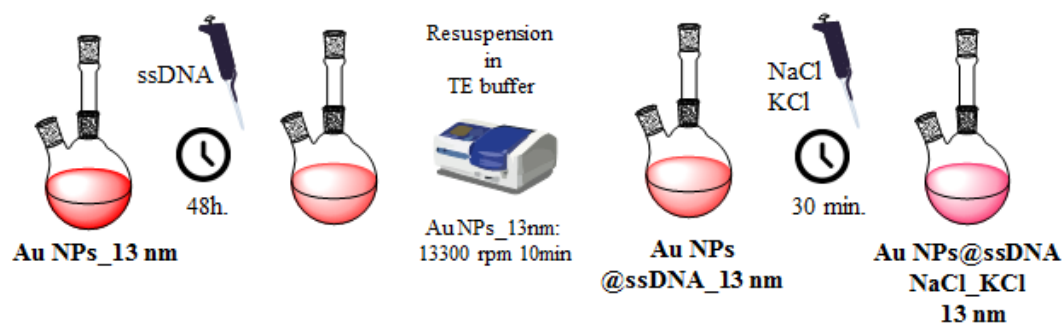
Figure 13: Schematic illustration of synthesis of modified aptamer Au NPs.

3.8 Detection of C-reactive protein using bioconjugated AuNPs with CDP

The tests for CRP detection were performed in a UV-vis spectroscopy quartz cell. Typically 12 μL of CRP solution with variable concentration (10, 20, 25, 30, 45 and 60 nM) and 22.6 μL of 1.13 mM $CaCl_2$ solution were introduced in the cell. Then, 240 μL of AuNPs@MUDA@CDP_40nm or AuNPs@MPA@CDP_10nm were added to the protein and the calcium chloride. The mixture was allowed to react for 5 minutes. A UV-vis spectrum was accomplished every 5 minutes for a period of 30 minutes.

3.9 Detection of C-reactive protein using bioconjugated AuNPs with aptamer

In order to detect CRP was added to a quartz UV-vis cell 230 μL of AuNPs@ssDNA+NaCl+KCl and 30 μL of 10, 20, 25, 30, 40, 45, 50, 60 and 100 nM CRP solutions. The cell was agitated four times in order to promote the mixture of CRP with aptamer modified Au NPs. Then, it was allowed to react for 5 minutes. Later was added 100 μL of 0.484 mM NaCl solution and the same process was repeated, the cell was agitated four times and left to react for 5 minutes [97]. Posteriorly, was performed a UV-vis spectra every 5 minutes until 30 minutes.

3 Experimental section

3.10 Instrumentation

3.10.1 Characterization of Au NPs

The **LSPR** band of the gold nanoparticles was evaluated using a GBC Cintra 303 UV–Vis spectrophotometer, using Milli-Q water as reference. The shift of the LSPR band in the Au NPs functionalized with MUDA, MPA, CDP and aptamer were investigated. For aptamer and Au NPs functionalized with aptamer the reference used was TE buffer. Each spectrum was acquired at the speed 200 nm/min.

The morphology and size of the Au NPs was analysed by high resolution transmission electron microscopy (**TEM**), using a JEOL 2010 transmission electron microscope operating at 200 kV. Samples for TEM analysis were prepared by evaporating suspensions of the nanoparticles on carbon-coated copper grids. The analysis of TEM images to build the particle size histograms was performed using the software ImageJ version 1.46.

The surface charge of the Au NPs, Au NPs@MUDA, Au NPs@MUDA and CDP bioconjugated Au NPs was assessed by **zeta potential** measurements performed in aqueous solutions, using a Zetasizer Nano ZS equipment from Malvern Instruments. The same equipment was used for evaluate the **hydrodynamic diameter** through dynamic light scattering (DLS) of the synthetized materials.

The **pH** measurement, zeta potential and DLS analysis were performed without dilution of nanoparticles.

FT-Raman was performed in order to identify the presence of MUDA or MPA in functionalized Au NPs. FT-Raman spectra were acquired using a FT-Raman spectrophotometer Bruker RFS 100S with a 1043 nm diode laser and fiber-optic probe. The laser power was 260 mW and the integration time was 10 s for all measurements. Also, a Raman spectral imaging and AFM were performed in a combined Raman-AFM-SNOM confocal microscope WITec alpha300 RAS+ (WITec, Ulm, Germany). A He:Ne laser operating at 532 nm and 633 nm was used as excitation source with the power set at 22 mW.

Fourier transform infrared spectroscopy (FTIR) was used to acquire the spectra of bare Au NPs, MPA, MUDA and MPA functionalized Au NPs and CDP functionalized Au NPs. These spectra were acquired in KBr pellets and were collected using a spectrometer Bruker optics tensor 27, using 512 scans at a resolution of 4 cm^{-1}. Samples for analysis were prepared by deposition of 3 to 5 drops of the colloid on KBr powder. Afterwards the powder was dried at 40ºC overnight and the pellets were prepared in a press.

3 Experimental section

Attenuated total reflectance - Fourier transform infrared spectroscopy (ATR - FTIR) was used to acquire the spectra of bare Au NPs, MUDA, MUDA and MPA functionalized Au NPs, CDP and CDP functionalized Au NPs. These spectra were acquired by N_2 drying of 1 mL of liquid samples (gold colloids) and were collected using a spectrometer Bruker optics tensor 27, using 512 scans at a resolution of 4 cm^{-1}.

From FTIR, FT-Raman and FTIR-ATR spectroscopies, ATR-FTIR with N_2 drying of bared and functionalized gold nanoparticles was the best technique for performing an IR spectrum of gold nanoparticles.

The concentration of gold nanoparticles (Au^0) was determinate by **inductively coupled plasma mass spectrometry (ICP-MS)**. The analysis was performed in Central Analysis Laboratory of Aveiro University. The samples were prepared by ultracentrifugation of 1 mL of Au NPs bare and functionalized with MUDA and MPA. The centrifugation was accomplished at 40000 g during 120 minutes for AuNPs_10nm and, at 16000 g during 45 minutes for AuNPs_40nm in a Sigma 2 - 16KCH Heated and Refrigerated Centrifuge at 25ºC. Afterwards the supernatant was carefully removed without perturb the pellet of gold nanoparticles. Then the Au NPs were resuspended in 0.5 mL of Milli-Q water.

3.10.2 Characterization of the aptamer

The UV-vis spectrum of the aptamer in Tris-HCl with EDTA (TE) buffer at pH 7.42 was performed in a GBC Cintra 303 UV-vis spectrophotometer. TE buffer was used as reference. The velocity of measurement was 200 nm/min. and the wavelength range was from 190 to 500nm.

Circular dichroism (DC) was performed in order to understand in which form was the G-quadruplex structure of simple strand (deoxyribonucleic acid) DNA. The samples analysed contained the aptamer solution: ssDNA and TE buffer. The velocity of measurement was 200 nm/min. and the wavelength evaluated was from 190 to 400nm, in a Jasco J-1500 CD spectrometer.

3.10.3 Characterization of C-reactive protein

A UV-vis spectrum of C-reactive protein (CRP) in phosphate buffer (PBS buffer) at pH 7.42 was performed in a GBC Cintra 303 UV-vis spectrophotometer. The PBS buffer was used as reference, the velocity of measurement was 200 nm/min and the wavelength range was from 190 to 500 nm.

4 Results and discussion

4 Results and discussion

4.1. Characterization of bare Au NPs

Citrate-capped gold nanoparticles with two distinct particle sizes were synthesized in this work. Au NPs synthesized via the Turkevich method were nearly spherical with an average size of 10.3 ± 1.4 nm, assessed by TEM analysis (**figure 14**). The TEM image suggests the presence of an organic component together with the Au NPs, even after centrifugation and resuspension of the particles. This could be residual sodium citrate that was used in the synthesis of Au NPs. Another phenomenon could be seen, the merge of some gold nanoparticles. Au NPs synthesized via the seed-growth method were spheroidal as well but larger, with an average size of 38.2 ± 5.3nm (**figure 14**). TEM image of Au NPs_40 nm reveals the presence of seed nanoparticles that did not complete the subsequent growth step. These samples will be designated by Au NPs_10 nm and Au NPs_40 nm, respectively. In **figure 15** it is showed the optical spectra and a photograph of the colloids. Au NPs_10nm exhibits the localized surface plasmon resonance (LSPR) band at 520.8 nm, while the LSPR band of Au NPs_40nm is localized at 540.0 nm. The absorbance at the LSPR band was 0.952 and 1.21 for 10 and 40 nm Au NPs, respectively. The data of the LSPR band were used to estimate the concentration of nanoparticles in the colloid, using the method described in the **section 3.3.1**.
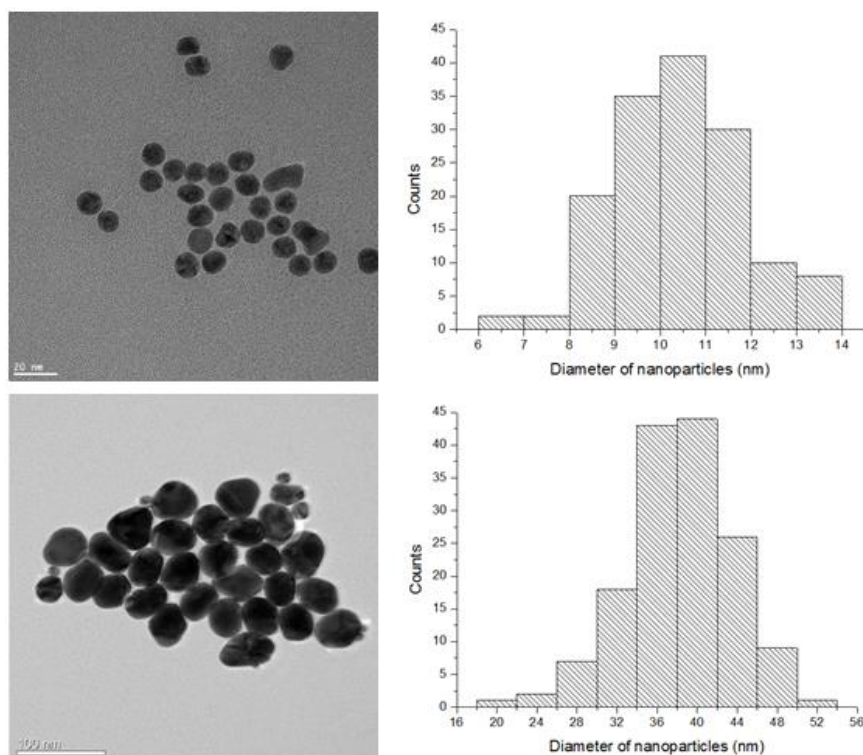
Figure 14: HR-TEM image of Au NPs_10nm in top corner at left and at the right the respective histogram of particle size; and Au NPs_40nm in the bottom of the corner at left and at the right the respective histogram, the seeds were not take in count for histogram construction.
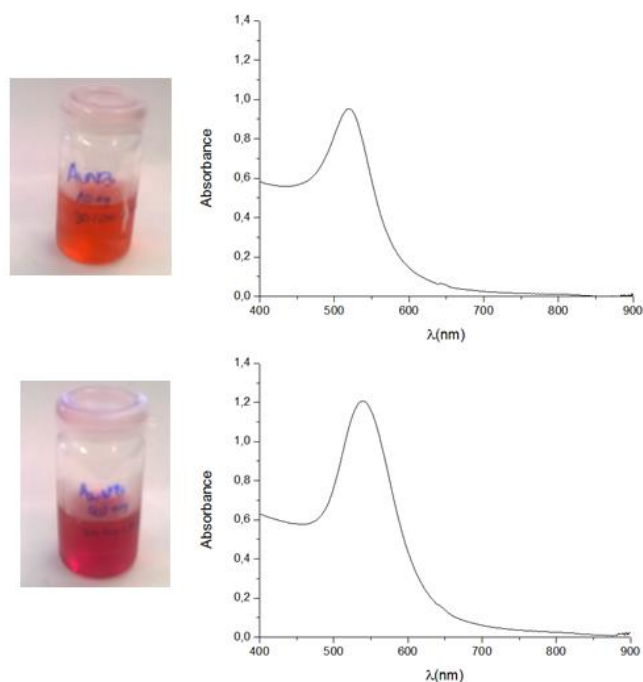
Figure 15: A photograph of Au NPs_10nm in top corner at left and at the right the respective visible spectra of particle; and Au NPs_40nm in the bottom of the corner at left and at the right the respective visible spectra.

The concentration of Au^0 in the form of nanoparticles in the colloids was assessed using ICP-MS, and it was obtained 2.89×10^{-4} and 2.29×10^{-4} mol Au^0/L for Au NPs_10 and 40 nm, respectively. For comparison, the Au^0 concentration was also calculated assuming that all the chloroauric acid was reacted and converted into Au NPs, as described in the **section 3.3.2.** With this method the concentration of Au^0 in the form of nanoparticles was 2.67×10^{-4} and 2.94×10^{-4} mol Au^0/L. The concentration of Au NPs was calculated from the concentration of Au^0 assuming spherical morphology of the Au NPs and having in mind that gold crystalizes in a face-centred cubic crystalline structure (4 Au atoms per unit cell with a volume of 0.0679 nm^3). The results (**table 5**) show that the Au NPs concentration values estimated from the chloroauric acid concentration are the most approximate to the experimental values obtained using the technique of ICP-MS. The difference between the values was 7.6% in Au NPs_10nm and 47.4% in Au NPs_40 nm. Thus assuming that all chloroauric acid reacts to form Au NPs gives good prediction of Au NPs concentration. Yet, using LSPR method the concentration of nanoparticles achieved was 1.46×10^{-9} and 4.35×10^{-11} mol NPs/L. The difference in relation to ICP-MS values was much higher in the Au NPs_10 nm (82.9%) and in the Au NPs_40 nm the difference was not so significant (62.5%).

4 Results and discussion

Table 5: Determination of Au NPs_10 nm and Au NPs_40 nm concentration through LSPR and chloroauric concentration and ICP-MS method.

Gold nanoparticles	LSPR method (mol NPs/L)	Chloroauric concentration (mol NPs/L)	ICP-MS (mol NPs/L)
Au NPs_10 nm	1.46×10^{-9}	7.92×10^{-9}	8.75×10^{-9}
Au NPs_40 nm	4.35×10^{-11}	1.71×10^{-10}	1.16×10^{-10}

4.2. Surface modification with MUDA and MPA

Figure 16 shows the TEM images of Au NPs_10nm functionalized with MUDA (Au NPs@MUDA_10nm) and with MPA (Au NPs@MPA_10nm), and the respective particles size histograms. The average size of Au NPs was 10.5 ± 1.1 nm and 10.6 ± 1.0 nm, respectively. Compared with bare Au NPs the variation in particle size was negligible as expected. Also, there was no variation in the morphology of the nanoparticles.

The particle size of bare Au NPs_40 nm was 38.2 ± 5.3nm. After functionalization with mercapto ligands the size was 38.5 ± 4.9nm and 38.4 ± 7.3nm for Au NPs@MUDA_40nm and Au NPs@MPA_40nm as seen in **figure 17** likewise, the particles kept the spheroidal morphology after functionalization. Nevertheless in Au NPs@MUDA_40nm few particles appear merged.

The optical spectra of the Au NPs before and after surface modification with 11-mercaptoundecanoic acid (MUDA) and 3-mercaptopropionic acid (MPA) are shown in **figure 18**.
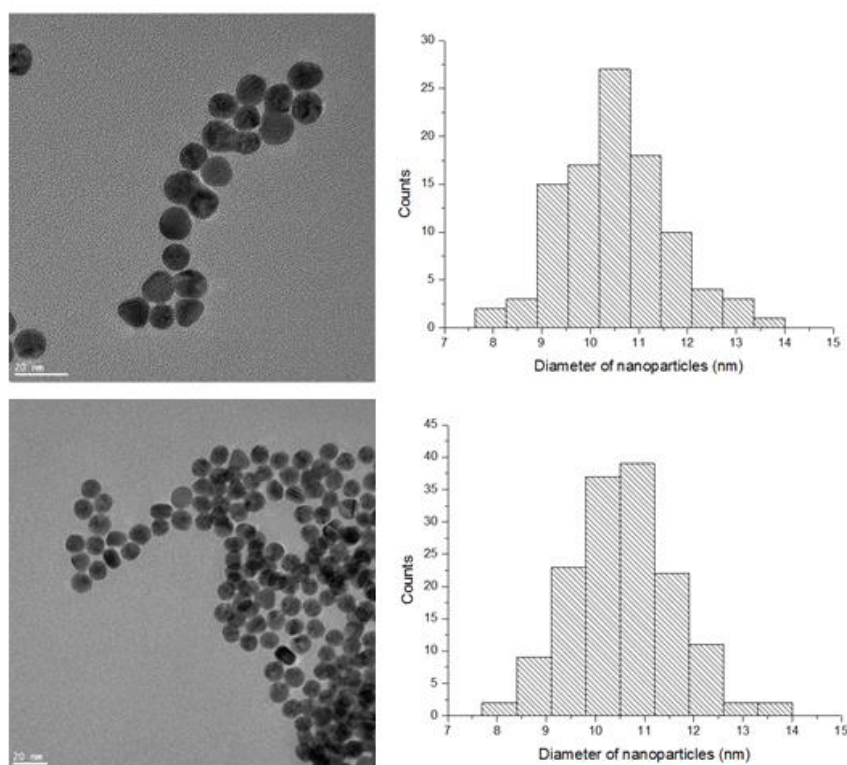
Figure 16: TEM images of Au NPs@MUDA_10nm (top left) and Au NPs@MPA_10nm (bottom left) and the respective histograms of the particle size (right).

4 Results and discussion

In the case of Au NPs_10 nm the LSPR band shows a negligible shift from 520.8 nm to 520.3 nm after surface modification with MUDA and MPA. For Au NPs_40nm a very small blue shift of the LSPR is observed from 540.0 nm to 539.5 and 538.6 nm after surface modification with MUDA and MPA, respectively. **Table 6** resumes the optical properties of bare gold nanoparticles and functionalized gold nanoparticles.

In all cases there is a marked decrease of the intensity of the LSPR band after surface modification. This could be in principle due to loss of Au NPs during resuspension of gold nanoparticles after the centrifugation step. ICP-MS analysis of the functionalized samples was performed to assess their Au NPs concentration (**table 6**.) In the case of Au NPs_10 nm there is a decrease of the concentration from 2.89×10^{-4} M to 2.01×10^{-4} and 2.64×10^{-4} M, for MUDA and MPA functionalization respectively, that could contribute to the decrease of the intensity of the LSPR band. Nevertheless, in the case of Au NPs_40nm the ICP results show even a slight increase of Au NPs concentration after mercapto functionalization, despite the decrease of the LSPR intensity.
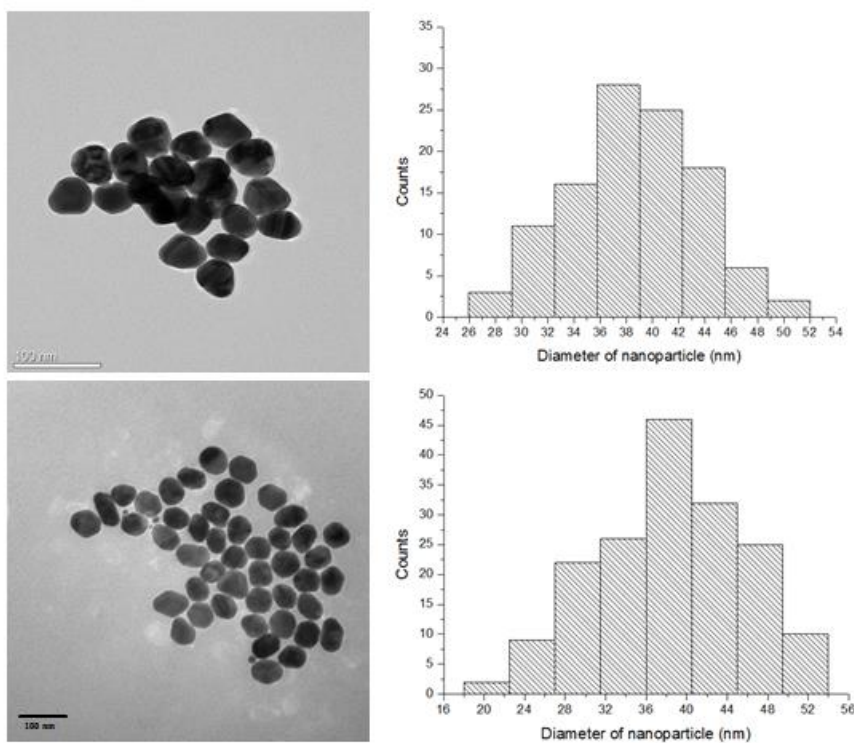
Figure 17: TEM images of Au NPs@MUDA_40nm (top left) and Au NPs@MPA_40nm (bottom left) and the respective histograms of the particle size (right).

4 Results and discussion
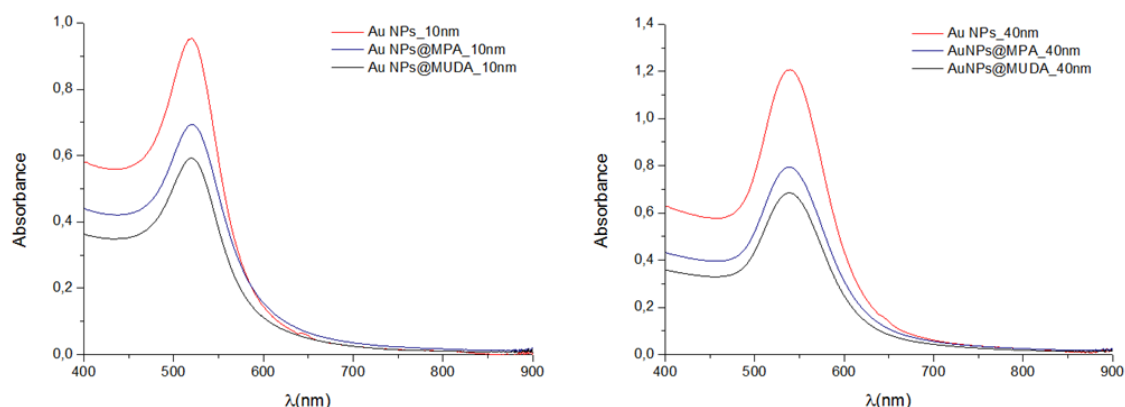
Figure 18: Optical spectra of bare Au NPs and functionalized Au NPs with MUDA or MPA.

Table 6: Wavelength and absorbance of LSPR band and Au NPs concentration assessed by ICP-MS of bare and functionalized Au NPs.

Sample	λ(nm)	Absorbance	ICP-MS (M)
Au NPs_10nm	520.8	0.952	2.89×10^{-4}
Au NPs_40nm	540.0	1.21	2.29×10^{-4}
Au NPs@MPA_10nm	520.3	0.694	2.64×10^{-4}
Au NPs@MUDA_10nm	520.3	0.592	2.01×10^{-4}
Au NPs@MPA_40nm	538.5	0.794	2.41×10^{-4}
Au NPs@MUDA_40nm	539.5	0.684	2.36×10^{-4}

Zeta potential measurements of bare Au NPs (**table 7**) revealed a negative surface charge due to the presence of, sodium citrate used in the synthesis procedure. After functionalization with MUDA and MPA, the nanoparticles were centrifuged and resuspended in the same volume of Milli-Q water for the removal of unreacted reagents. At pH 6.3, the zeta potential value of Au NPs_10nm was -76.9 mV and similar value was observed after surface modification with MUDA (-75.8 mV, pH 6.1) and MPA (-73.6 mV, pH 6.1). Au NPs_40nm display a more negative surface with zeta potential values of -89.5 mV at pH 6.1 and identical values after functionalization with MUDA (-81.2 mV, pH 6.0) and MPA (-83.3 mV , pH 6.0). The fact that the surface charge of functionalized AuNPs was markedly negative is in agreement with the presence of carboxylate groups from mercapto ligands at the surface of Au NPs.

DLS measurements were performed in order to verify if there was an increase of the hydrodynamic diameter of Au NPs after surface modification with the mercapto ligands. **Table 7** resumes all measurements mentioned before.

4 Results and discussion

Table 7: Final pH, zeta potential, hydrodynamic diameter (Dh) and polydispersity index (PDI) of the colloids before and after surface functionalization.

Samples	pH	Zeta potential (mV)	Hydrodynamic diameter (Dh.nm)	PDI
AuNPs_10nm	6.3	-76.9± 1.4	24.11 ± 0.23	0.239
AuNPs_40nm	6.1	-89.5±4.7	37.82 ± 0.12	0.321
AuNPs@MUDA_10nm	6.0	-75.8±1.0	26.90 ± 0.88	0.360
AuNPs@MUDA_40nm	6.1	-81.2 ± 0.7	40.72 ± 1.21	0.361
AuNPs@MPA_10nm	6.1	-73.6±1.3	24.55 ± 0.29	0.261
AuNPs@MPA_40nm	6.0	-83.3±0.7	38.30 ± 0.11	0.320

As expected, the hydrodynamic diameter (Dh) increased with the average size of nanoparticles. Au NPs_10nm with 10.3 ± 1.4 nm of average size revealed a hydrodynamic diameter of 24.11 ± 0.23 nm and Au NPs_40nm with 38.2 ± 5.3 nm a similar hydrodynamic diameter of 37.82 ± 0.12 nm was observed. After surface functionalization, the hydrodynamic diameter increased, which can be ascribed to the presence of MUDA or MPA in the surface of nanoparticles. After modification with MPA, the Dh increased from 24.11 ± 0.23 and 37.82 ± 0.12 nm to 24.55 ± 0.29 and 38.30 ± 0.11 nm for Au NPs_10nm and Au NPs_40nm, respectively. Using MUDA, which contains a longer carbon chain (11 carbons) than MPA, the final Dh was larger, being 26.90 ± 0.88 and 40.72 ± 1.21 nm for Au NPs_10nm and Au NPs_40nm, respectively.

The analysis of the **polydispersity index (PDI)** allowed to understand if synthetized nanoparticles were monodispersed (values between 0.0 and 0.1) or polydispersed (values between 0.1 and 0.4) in solution [118].The PDI results (**table 7**) show that synthetized nanoparticles were size polydisperse in solution, with PDI values ranging from 0.24 to 0.36.

ATR-FTIR spectroscopy was used to get further evidences of the successful functionalization of Au NPs with MUDA and MPA. To facilitate the assignment of the bands, **figures 43**, **44**, and **45 (appendix A2)** show the FTIR spectra of sodium citrate tribasic (the stabilizing agent of bare Au NPs), MUDA and MPA. As MPA is a viscous liquid, it was not possible to acquire its spectrum using a KBr disk, therefore a FTIR spectrum from literature [119] was included instead.

4 Results and discussion

Figure 19 compares the FTIR spectra of bare and mercapto functionalized gold nanoparticles with 10 nm and 40nm diameter. The most representative FTIR bands of sodium citrate and bare Au NPs_10nm and 40 nm were assigned in **table 11 (appendix A3)**. The presence of citrate in bare gold nanoparticles was confirmed by the appearance of the asymmetric stretching band COO$^-$ of deprotonated carboxylic acid group in Au NPs_10 nm at 1584 cm^{-1} and in Au NPs_40nm at 1580 cm^{-1}. Also, the following infrared vibrations of citrate were identified in bare Au NPs: (COO$^-$) symmetric stretching vibration at 1393 and 1400 cm^{-1} for Au NPs_10nm and Au NPs_40 nm [120], respectively; the C-O-H stretching vibration at 1282 cm^{-1} in citrate appears shifted to 1276 cm^{-1} and 1269 cm^{-1} in Au NPs_10nm and 40nm, respectively. Furthermore, C-C stretching vibration at 908 cm^{-1} in citrate appears at 908 and 894 cm^{-1} respectively for Au NPs_10nm and Au NPs_40 nm [121]; C-COOH stretching vibration at 838, 848 and 841 cm^{-1} for citrate, Au NPs_10nm and Au NPs_40 nm, respectively [122].

The assignment of the most relevant FTIR bands of functionalized Au NPs was elaborated in **table 12 (appendix A3)**. The bands at 1733 cm^{-1} in spectrum of Au NPs@MUDA_10nm could be ascribed to the C=O stretching of carboxylic acid group (-COOH) of MUDA. Nevertheless this band was not visible in Au NPs@MPA_40nm spectrum. The stretching vibrations present in Au NPs@MUDA_10nm at 1393 cm^{-1} and 40nm at 1395 cm^{-1} could be due to COO$^-$ stretching vibrations in MUDA [123]. In MUDA spectrum these vibrational bands appear at 1470 and 1436 cm^{-1}. The carboxylic group of MUDA was present on a protonated and non-protonated state as
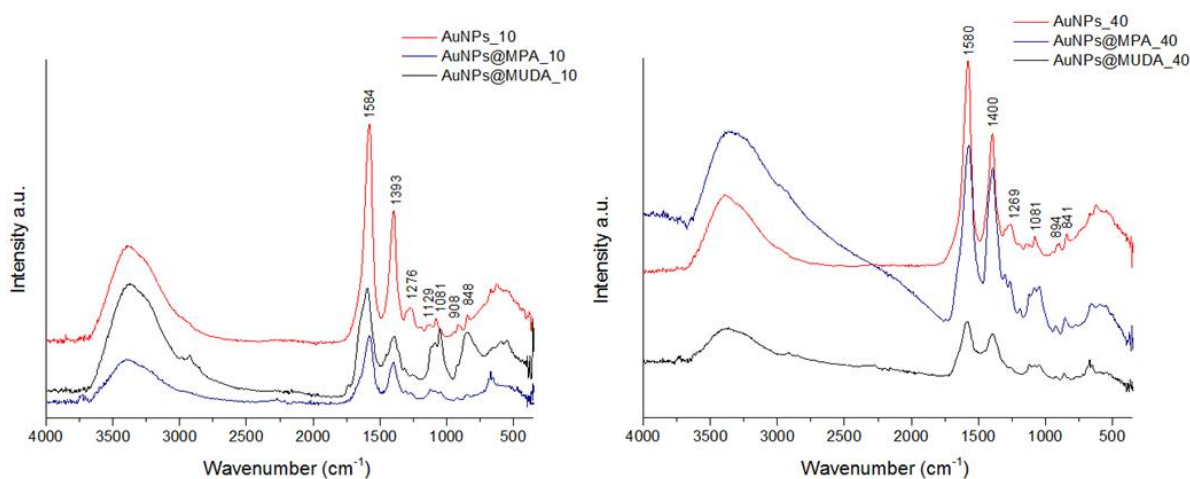
Figure 19: ATR-FTIR spectra of Au NPs_10nm , Au NPs@MPA_10nm and Au NPs@MUDA_10 nm (left) and of Au NPs_40nm , Au NPs@MPA_40nm and Au NPs@MUDA_40 nm (right).

stretching C-COOH at 818 cm^{-1} and C-COO$^-$ at 943 cm^{-1}, respectively. This stretching vibrations was present in Au NPs@MUDA_10nm and 40 nm at 922 cm^{-1} for C-COO$^-$ and, 838 cm^{-1} and 826 cm^{-1} for C-COOH, respectively [122].

In case of MPA, it could be identified infrared vibrations similar to MUDA due to the similar structure. This similar vibration is the COO⁻ stretching vibrations of carboxylic group of MPA. In gold nanoparticles functionalized with MPA, the presence of the C=O stretching of carboxylic group at 1740 cm⁻¹ of AuNPs@MPA_10nm can be also seen. Moreover, this vibration should be present in AuNPs@MPA_40nm, but spectra resolution did not allowed its visualization. The presence of the stretching vibration of COO⁻ group was not observed in spectra of MPA, as well as the presence of carboxylic group in a protonated (C-COOH) and non-protonated (C−COO⁻) state. However, it was observed in spectra of MPA functionalized gold nanoparticles the vibration of COO⁻ group at 1400 cm⁻¹ and 1393 cm⁻¹ [124], in protonated state at 848 cm⁻¹ and 858 cm⁻¹, and in non-protonated state at 929 cm⁻¹ for 10nm and 40nm, respectively. Also, the C-O-H stretching vibration was not verified in MPA, but was present in MPA functionalized Au NPs at 1310 cm⁻¹ and 1303 cm⁻¹ for 10nm and 40nm, respectively [122].

Once both citrate, MUDA and MPA contain carboxylic acid groups on their composition, it was not possible to prove that the functionalization with the mercapto ligands was successful, based only on the assignment of the carboxylic acid group. However, other less intense vibration bands present in MUDA and MPA spectra that are not typical of citrate was identified in the functionalized Au NPs spectra. For example, MUDA functionalized Au NPs show a band at 2925 cm⁻¹ (10 nm) and 2918 cm⁻¹ (40 nm) that is ascribed to the stretching of –CH₂- in long chain of MUDA. As expected this contribution is much smaller in the case of MPA that contains a much shorter carbon chain. In addition the C-C twisting band of the aliphatic backbone of mercapto ligands is visible in the Au NPs functionalized with MUDA (1116 cm⁻¹) and MPA (ca 1121 cm⁻¹).

Attempts were made to further prove the functionalization with MUDA and MPA using FT-Raman spectroscopy and FTIR using KBr. The attempts were unsuccessful and no significant differences between citrate stabilized and mercapto functionalized Au NPs could be observed (**figures 48** and **49**) (**appendix A5**).

4.3. Bioconjugation with CDP

Au NPs modified with MPA and MUDA were bioconjugated with cytidine diphosphocholine (CDP), composed by cytosine, a D-ribose and a diphosphate with a C3 aliphatic chain [125]. The compound 1-(3-dimethylaminopropyl)-3-ethylcarbodiimide hydrochloride (EDC) was used to promote the covalent attachment of CDP to Au NPs (**section 3.6**). As **figure 20** illustrates, after functionalization with CDP the colour of the solution became bright which might be evidence that the functionalization was achieved. The optical spectra of CDP bioconjugated Au NPs was presented in **figure 21**. After addition of CDP the LSPR band of Au NPs_10 nm was shifted from 520.3 to 520.8 and 520.8 to 524.0 nm for MPA and MUDA NPs, respectively. A

decrease of absorbance at A_{LSPR} was noticed for 0.375 and 0.493 for Au NPs@MUDA and Au NPs@MPA, respectively.
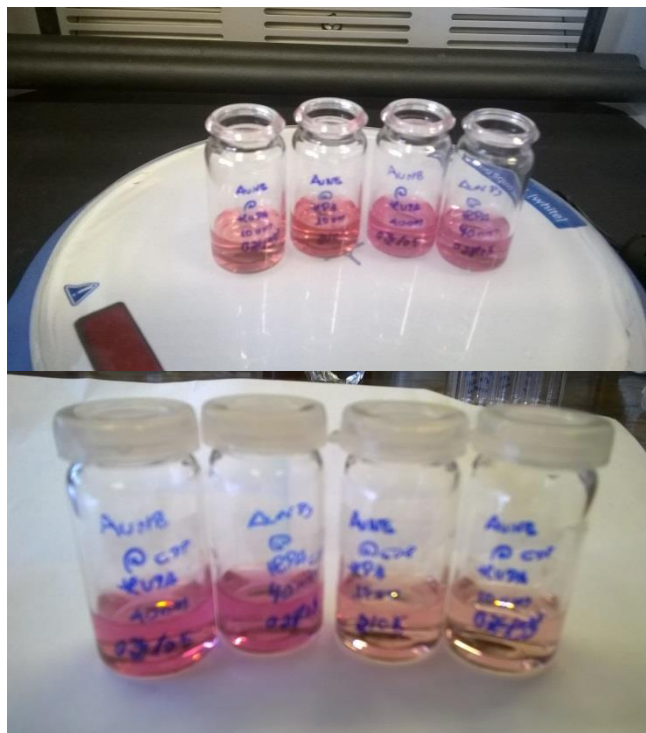
Figure 20: A photograph of AuNPs@MUDA_10nm, AuNPs@MPA_10nm, AuNPs@MUDA_40nm, AuNPs@MPA_40nm, before the functionalization with CDP (top) and at the bottom AuNPs@MUDA_40nm, AuNPs@MPA_40nm, AuNPs@MUDA_10nm and AuNPs@MPA_10nm, after the functionalization with CDP.

In Au NPs_40nm, a red shift was observed from 538.5 to 542.4 nm and from 539.5 to 543.3 nm and a decrease in absorbance from 0.794 to 0.444 and from 0.684 to 0.363 in Au NPs@MPA and AuNPs@MUDA, respectively. This LSPR shift might be due to the increase of molecules length attached to the surface of nanoparticles. Also, in all experiments the absorbance decreased. Zeta potential measurements (**table 8**) revealed zeta potential values of -58.3 mV for Au NPs@MUDA@CDP_10nm (pH 6.1), -52.4 mV at pH 6.1 for Au NPs@MUDA@CDP_40nm and, -69.1 and -67.7 mV (pH 6.2 and 6.0) for Au NPs@MPA@CDP_10nm and Au NPs@MPA@CDP_40nm, respectively. The results indicate that zeta potential values were less negative than the mercapto functionalized gold nanoparticles.

The hydrodynamic diameter increased when mercapto functionalized Au NPs were bioconjugated with CDP. More specifically, in Au NPs@MUDA@CDP_10nm increases from 26.90 to 45.37 nm, in Au NPs@MUDA@CDP_40nm from 40.72 to 47.60 nm, in Au NPs@MPA@CDP_10nm from 24.55 to 39.21 nm and in Au NPs@MPA@CDP_40nm from

4 Results and discussion
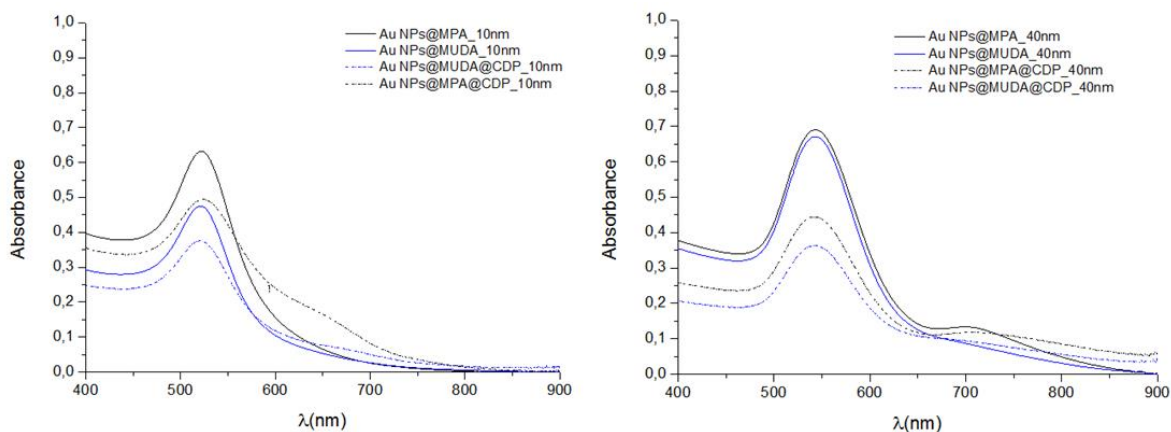
Figure 21: Optical spectra of bioconjugated Au NPs with cytidine diphosphocholine.

38.30 to 42.36 nm. These results were consistent with the addition of CDP to mercapto functionalized gold nanoparticles.

Table 8: Final pH, zeta potential, hydrodynamic diameter (Dh) and polydispersity index (PDI) of the colloids after CDP bioconjugation.

Samples	pH	Zeta potential (mV)	Hydrodynamic diameter (Dh.nm)	PDI
Au NPs@MPA@CDP_10nm	6.1	-58.3±2.0	45.37±2.19	0.692
Au NPs@MUDA@CDP_40nm	6.1	-52.4±2.4	47.60±0.24	0.320
Au NPs@MPA@CDP_10nm	6.2	-69.1±1.0	39.21±1.27	0.493
Au NPs@MPA@CDP_40nm	6.0	-67.7±0.6	42.36±0.30	0.327

The **ATR-FTIR** spectra were acquired for the nanoparticles Au NPs@MUDA@CDP_40nm and Au NPs@MPA@CDP_40nm. Unsuccessful attempts were made to obtain FTIR spectra of the CDP conjugated 10 nm Au NPs that resulted in low quality spectroscopy data.

Figure 22 shows the ATR-FTIR spectra of Au NPs@MUDA@CDP_40nm and Au NPs@MPA@CDP_40nm. Also the ATR-FTIR spectrum of cytidine 5' diphosphocholine (CDP) was acquired in order to identify the vibrations present in this molecule for comparison with spectra of CDP bioconjugated Au NPs (see **figure 46** at **appendix A2**). **Table 13** at **appendix A3** lists the infrared vibrations assigned for CDP and for CDP bioconjugated Au NPs_40nm.

Carbodiimide (EDC) was used to activate the carboxylic acid groups of mercapto functionalized Au NPs that should then react with amine group of CDP to form an amide linkage. Several new bands appear in the spectra (**figure 22**) after the bioconjugation of Au NPs with CDP

49

that could be ascribed to the presence of CDP. Thus a very intense band appears at 1047 and 1037 cm^{-1} for Au NPs@MUDA@CDP_40nm and Au NPs@MPA@CDP_40nm, respectively that could be ascribed to scissoring vibrations of N-C-H and C-H stretching in CDP. In the spectrum of Au NPs@MPA@CDP_40nm an intense band appears at 1263 cm^{-1} that could be due to C-N stretching of CDP. This band is less visible in the spectrum of Au NPs containing MUDA. The band at 1643 cm^{-1} in Au NPs@MUDA@CDP_40nm and 1693 cm^{-1} in Au NPs@MPA@CDP_40nm should result both from the contribution of C=O stretching from CDP (appears at 1658 cm^{-1} in CDP spectrum) and the amide I band (C=O and C-N stretching and N-H bending) due to the formation of the amide linkage between the Au NPs and the CDP. Although less marked it is possible to observe in the spectra a contribution at around 1520 cm^{-1} that can be ascribed to the amide II band (C-N stretching and N-H bending) of the covalent linkage [122].
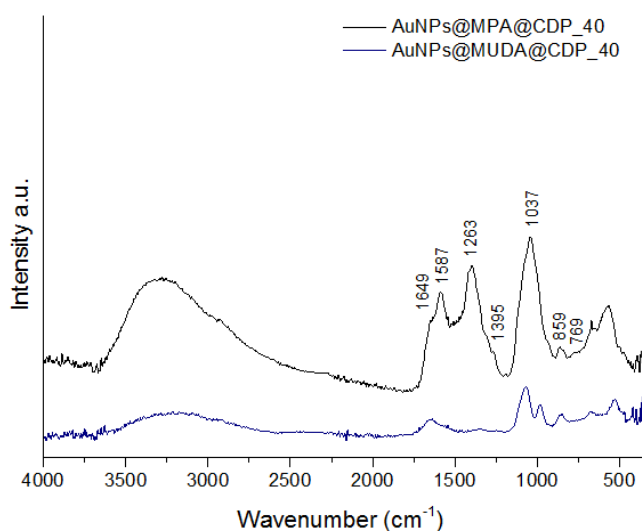
Figure 22: ATR-FTIR spectra of Au NPs@MPA@CDP_40nm and Au NPs@MUDA@CDP_40nm.

4.4. Surface modification with aptamer

As previously referred, high extinction coefficient of the Au NPs is desirable for the development of a sensitive colorimetric method [117]. It is known that the extinction coefficient of Au NPs increases with particle size [126], thus in principle 40 nm Au NPs would be more suitable for detection purposes. Nevertheless smaller nanoparticles provide larger specific surface area, which also favours detection after proper surface modification. Indeed a previous study has shown promising results in the detection of protein (thrombin) using smaller Au NPs (13 nm diameter) modified at the surface with an aptamer [97].

4 Results and discussion

Thus for the surface modification with the aptamer, a new batch of gold nanoparticles was prepared using the Turkevich method. The average size of the Au NPs was 13.1±1.6 nm, as presented in **figure 50**, **appendix A6**. These nanoparticles (Au NPs_13 nm) showed an almost spherical morphology, having some gold nanoparticles with a nearly triangular shape.

The UV-vis spectrum was collected. These gold nanoparticles exhibit a LSPR band at 520 nm and the corresponding absorbance of 0.912, as shown in **figure 23**. The concentration of Au NPs_13 nm calculated assuming complete reaction of the chloroauric acid was 2.67×10^{-4} M.
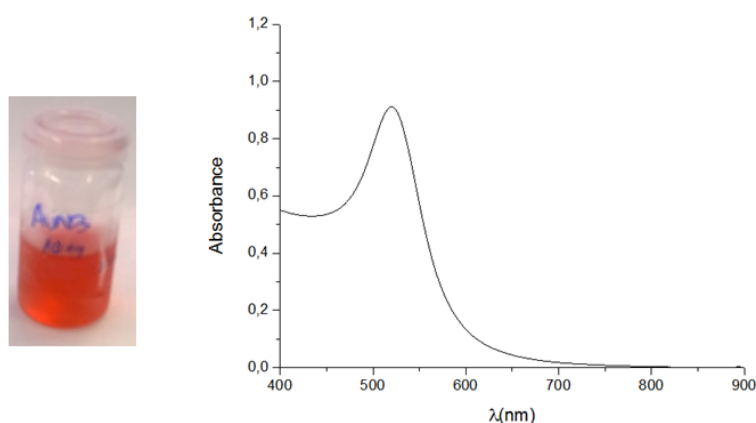
Figure 23: A photograph of Au NPs_13nm colloid (left) and the respective visible spectrum (right).

The aptamer used in this work is an oligonucleotide specific for C-reactive protein, with the following sequence: 5'-CGA AGG GGA TTC GAG GGG TGA TTG CGT GCT CCA TTT GGT G-3'. According to previous work [61] this ssDNA displays very high affinity and specificity against CRP. The dissociation constant (k_d) of the selected aptamer towards CRP was 16.2 nM, that was lower compared with other tested aptamers. Smaller k_d indicates higher affinity between the aptamer and the protein due to tight the interaction and formation of aptamer-protein complex. Before performing the functionalization, the aptamer, was characterized using UV-vis and circular dichroism (CD) spectrophotometry. **Figure 24** shows the UV-vis spectra of aptamer concentrated (as received) and with a dilution ratio of 1:10 in Tris-HCl (TE) buffer. The absorbance of the aptamer concentrated and diluted at 260 nm was 0.969 and 0.749, respectively. The concentration of the ssDNA was calculated through the absorbance at 260 nm from the UV-vis spectra of aptamer diluted, due to signal saturation of aptamer concentrated. The obtained concentration of aptamer was 19.7 μM, a similar value compared to the value referred in the instructions guide of the purchased aptamer, which was 20 μM. Also, it was verified if the ssDNA was free of contaminations. In a DNA free of protein or phenols the value of the A_{260}/A_{280} ratio is equal or superior to 1.8 [127, 128]. Herein the absorbance of the diluted aptamer at 280 nm was 0.512, and the

ratio A_{260}/A_{280} was 1.46, which suggests the presence of contaminants in the ssDNA [127, 128]. In addition, the shape of UV-vis spectrum of aptamer was not a perfect Gaussian curve which might be due to G-quadruplex structure formation [129].
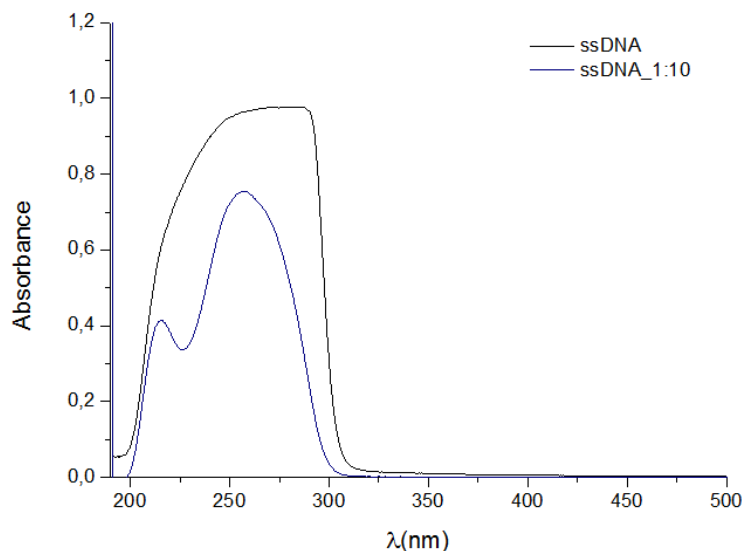
Figure 24: Representation of UV-vis spectra of concentrated ssDNA and diluted ssDNA (ratio 1:10), in diluted ssDNA the first curve (215 nm) is the signal of TE buffer.

The aptamer used in this work is a simple stranded DNA (ssDNA), rich in guanine in order to form a G-quadruplex (G4) structure. These G4 structures are arrangements of guanine that could be formed by the molecule itself, with other stranded DNA or protein. The formation of a G4 structure is composed by several G-quartets stacked. A G-quartet has 4 guanines disposed in a square disposition due to Hoogsteen hydrogen-bonding arrangement (**figure 25**) [130, 131]. The formation of this structure is rather important and plays a key role in the mechanism of CRP detection.
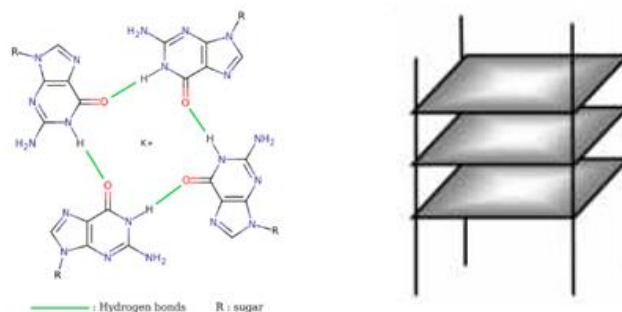
Figure 25: A G-quartet structure comprising 4 guanines and the Hoogsteen hydrogen-bonding arrangement, structure usual in G-rich DNA sequences [131] at left and G4 structure composed by 3 stacked G-quartets (shaded squares) [132].

The DC spectra of concentrated and diluted aptamer were collected in order to characterize the possible folding typologies of G4 structures. According to **figure 26** the ssDNA had an intense positive band around 300 nm that turns into a slight negative band around 290 nm. With this description the ssDNA could be considered be in a bimolecular quadruplex [d(G4T4G4)]$_2$ [130]. However, this sequence it was not founded in ssDNA sequence: 5' CGA AGG GGA TTC GAG GGG TGA TTG CGT GCT CCA TTT GGT G 3'. Yet, in ssDNA diluted in ratio 1:10 an intense positive band was present at 280 nm (approximately), turns into negate near at 250 nm and turns into positive again at 230 nm and 197 nm. This type of line shape was observed in non canonical G4 sequences [133]. Comparing ssDNA concentrated and diluted, it could be observed that the Hoogsteen hydrogen-bonding arrangement is different. This may be due to the abundance in ssDNA molecules that lead to different hydrogen bonding arrangement that changes G4 conformations.

In order to evaluate the effect of the surface modification with aptamer in the optical properties of gold nanoparticles, the UV-vis spectrum was collected before and after surface modification. **Figure 27** shows the LSPR band in bare Au NPs localized at 520.0 nm with an absorbance of 0.912. However after modification a slight red shift to 521.3 nm and a marked decrease of the absorbance to 0.521 were observed. Also, a new band of 260.2 nm with an absorbance of 0.603 appeared, that confirmed the presence of ssDNA/aptamer at the surface of gold nanoparticles.
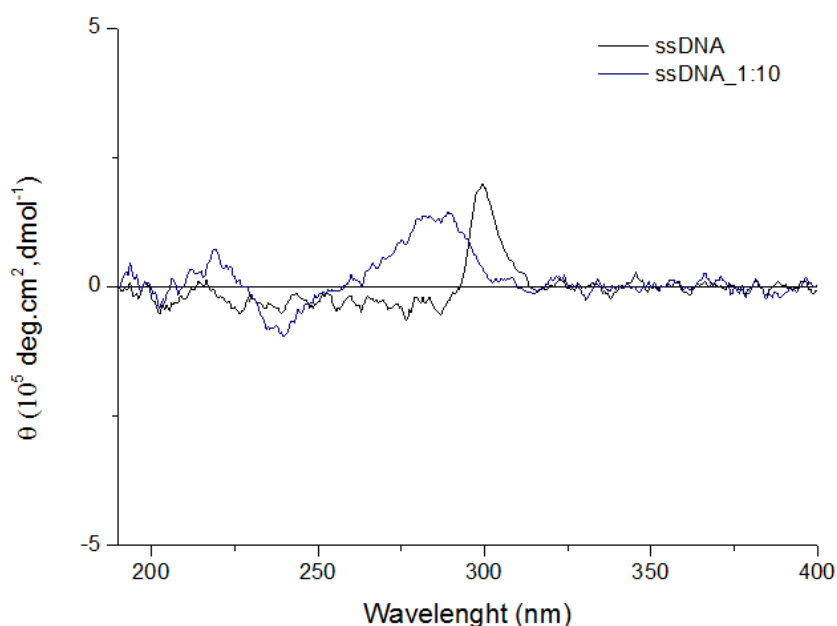
Figure 26: Circular dichroism spectra of the aptamer concentrated and diluted in ratio 1:10.
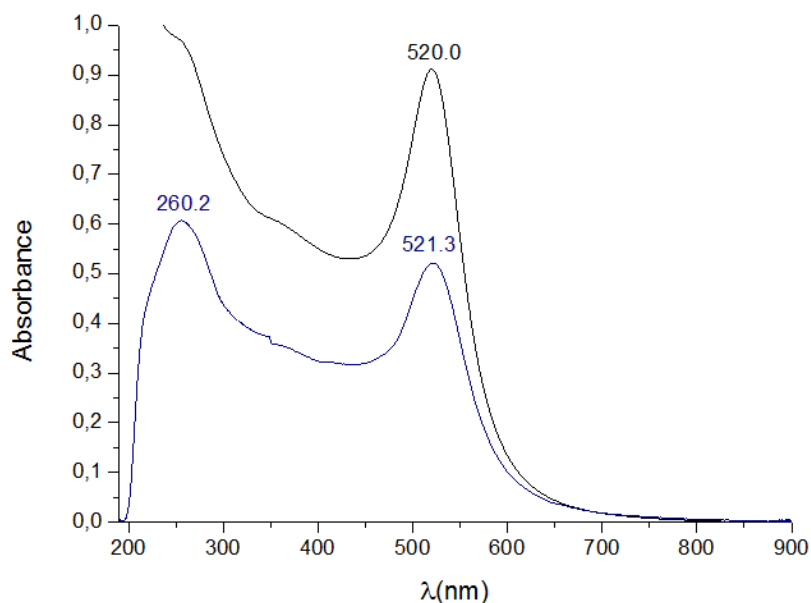
Figure 27: UV-vis spectra of bare Au NPs (black) and aptamer modified Au NPs (blue), after 48h trial.

4.5. C-reactive protein detection using functionalized gold nanoparticles

The CRP detection was investigated using gold nanoparticles with two distinct surface functionalizations: functionalized with CDP and functionalized with the aptamer. In the first approach, it is expected to detect CRP through the interaction between calcium ions of CRP and two oxygens of CDP phosphate group [27]. In the later approach, it is expected that in the presence of CRP, the unfold aptamer stacked onto gold nanoparticles surface will form a G4 structure [98]. In both strategies CRP detection should be possible due to changes on optical properties owing to gold nanoparticles aggregation. This aggregation was quantified by monitoring the ratio between the absorbance at 620 nm and at LSPR (A_{620}/A_{LSPR}) of functionalized Au NPs.

A stock of CRP solution (100 nM) was prepared by dilution of the acquired CRP solution (2.1 mg/mL) in phosphate (PBS) buffer 11.0 mM at pH 7.42. This stock solution was then used to prepare CRP standard solutions with distinct concentrations (10, 20, 25, 30, 40, 45, 50 and 60 nM) that were used to obtain a calibration curve for CRP detection. The UV-vis spectra of 100 nM CRP solution and dilution 1:10 are included, in **figure 28** and show an absorption band centred at 280 nm that is ascribed to the C-reactive protein.

4 Results and discussion
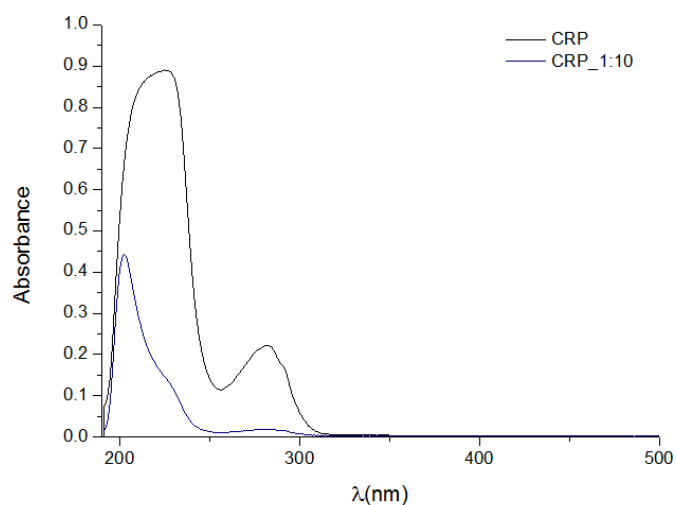
Figure 28: UV-vis spectra of CRP solution 100 nM and diluted CRP (ratio 1:10) and diluted solution (1:10).

4.5.1. CRP detection using AuNPs bioconjugated with CDP

Among the four different materials synthetized, AuNPs@MUDA@CDP_40nm and AuNPs@MPA@CDP_10nm were selected and tested for CRP detection. The detection tests were performed as described in **section 3.8**. Briefly, the CDP conjugated Au NPs were added to a solution of CRP of well-known concentration containing calcium ions. The optical properties of the mixture were monitored by acquisition of the UV-vis spectra along 30 minutes. **Figure 29** shows the variation of the aggregation ratio A_{620}/A_{LSPR} with time for Au NPs@MPA@CDP_10nm after being in contact with CRP solution of concentration ranging from 10 to 60 nM. In all the CRP concentrations tested, a pronounced increase of the aggregation ratio was observed in the first 5 minutes and afterwards (from 5 to 30 minutes) the A_{620}/A_{LSPR} ratio increases more
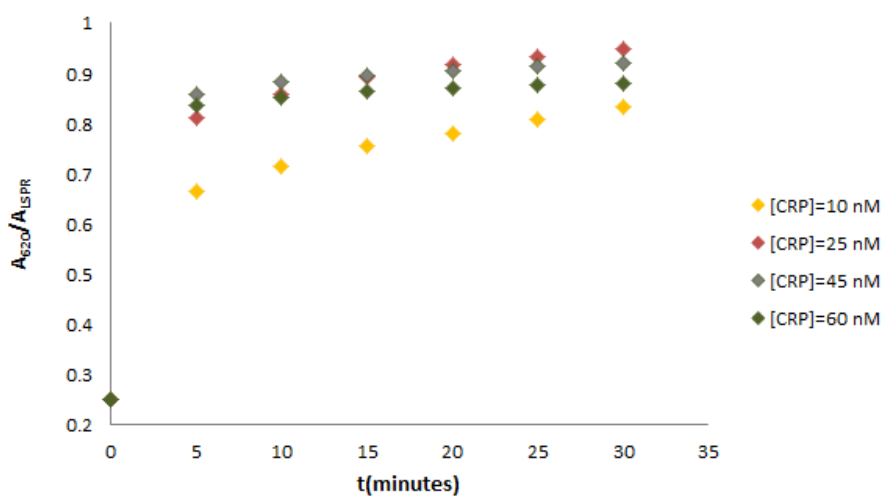
Figure 29: A_{620}/A_{LSPR} variation along 30 minutes after addition of distinct concentrations of CRP (from 10 to 60 nM) using AuNPs@MPA@CDP_10nm as biosensor.

55

gradually. In principle, the two oxygens from phosphate groups of CDP bioconjugated Au NPs can establish interactions with two calcium ions of CRP. This interaction lead to changes in the aggregation state of Au NPs caused by the fact that each CDP molecules present at Au NP could stablish two or more interactions with the same CRP molecule and with others CRP molecules. It is expected than higher CRP concentration will lead to higher values of aggregation ratio. Nevertheless, after 30 minutes the opposite trend was observed, with aggregation ratio A_{620}/A_{LSPR} decreasing when the increasing the CRP concentration from 25 nM to 45 nM and 60 nM, **figure 30**. However, 10 nM CRP induced less aggregation than 25 nM as was expected.
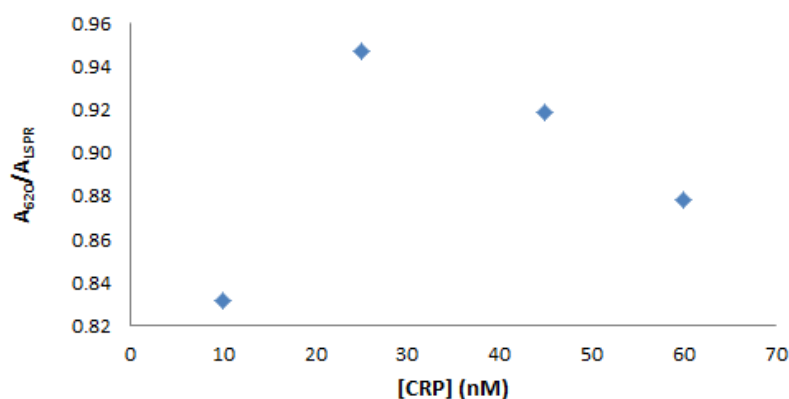
Figure 30: A_{620}/AL_{SPR} variation variation of different concentrations of CRP: 10, 25, 45 and 60 nM using AuNPs@MPA@CDP_10nm as biosensor at 30 minutes.

In case of AuNPs@MUDA@CDP_40nm it was performed trials where different concentrations of CRP, from 10 to 60 nM were tested. As could be seen in **figure 31** the material showed an increase in A_{620}/A_{LSPR} for 5 minutes, but from 5 to 30 minutes a slight decrease was observed for 10, 20 and 45 nM. However, for 50 nM the aggregation ratio was increased along time. It was considered 5 minutes the time for CRP detection using this material.
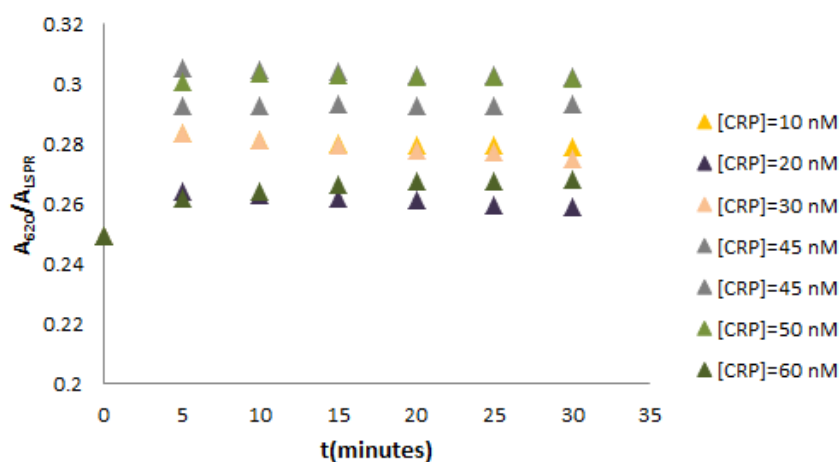
Figure 31: A_{620}/A_{LSPR} variation along 30 minutes after addition of distinct concentrations of CRP (from 10 to 60 nM) using AuNPs@MUDA@CDP_40 as biosensor.

4 Results and discussion

The test using a solution of 45 nM CRP concentration was replicated for understanding if the material had a similar answer. The A_{620}/A_{LSPR} ratio results obtained were 0.305 and 0.293, being similar. All concentrations for CRP detected were presented in **figure 32** at the time of detection. As could be seen in this figure a linear behaviour with the 20, 30, 45 and 50 nM CRP concentrations was observed. Yet, if the 20 nM point of the trial was included, the correlation coefficient had a slight improvement from the 0.9420 to 0.9425, as may be observed in **figure 32** at the left and right, respectively. The results suggest that the AuNPs@MUDA@CDP_40nm detected CRP, following a linear range correlation between CRP concentration and the aggregation ratio, for CRP concentrations ranging between 20 and 50 nM. However, these trials were only indicatives and needed to be replicate in order to be confirmed and more CRP concentrations should be tested.
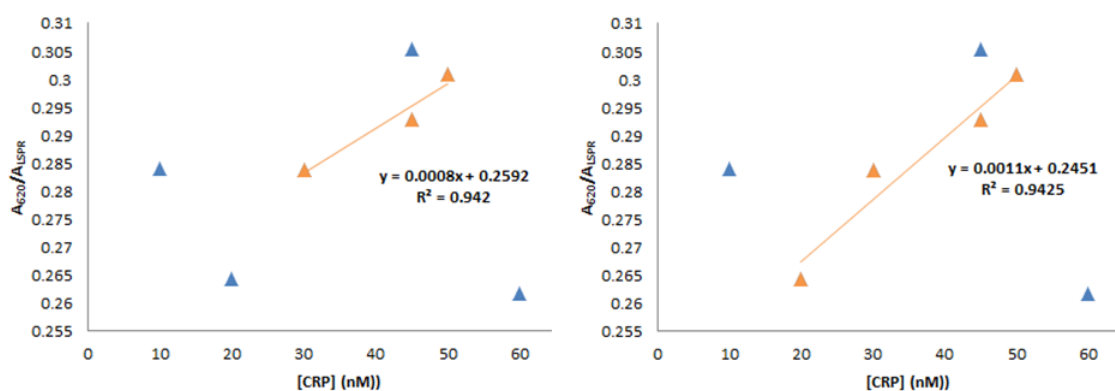
Figure 32: A_{620}/A_{LSPR} variation of different concentrations of CRP: 10, 20, 30, 45, 50 and 60 nM using AuNPs@MUDA@CDP_40 as biosensor at 5 minutes; including 30, 45 and 50 nM in calibration curve at the left and, 20, 30, 45 and 50 nM at the right.

Comparing this material with Au NPs@MPA@CDP_10nm it is perceived that the aggregation ratio at 0 minutes (materials without CRP) was similar, 0.25; but the Au NPs@MPA@CDP_10nm had an A_{620}/A_{LSPR} ratio higher for the same CRP concentrations: 10, 45 and 60 nM (**figures 30** and **32**).

4.5.2. CRP detection using Au NPs functionalized with aptamer

As described above in the experimental section (**section 3.9**) prior to test with CRP, the cations Na^+ (NaCl) and K^+ (KCl) were added to the Au NPs functionalized with aptamer (Au NPs@ssDNA) [97]. This was done with the purpose of stabilizing the G4 structure that is expected to be formed as the result of the interaction of CRP with the aptamer [133, 134]. The effect of adding these ions on the optical properties of the functionalized Au NPs was investigated.

4 Results and discussion

Effect of NaCl and KCl addition

The influence of the concentration of salts was investigated. **Table 9** lists the conditions of the experiments performed as well as the changes observed on the optical properties. Overall the addition of the cations K^+ and Na^+ caused a visible colour change in gold nanoparticles solution that became more purplish. After adding salts the intensity of the LSPR band decreases and an increase of the intensity at 620 nm was observed. A red shift of the LSPR band is observed as well. The UV-vis spectrum of the Au NPs@ssDNA before and after addition of Na^+ and K^+ is shown in the **figure 33** for trial #2, as example. As it could be seen the addition of the cations caused a red-shift of the LSPR band from 521.3 nm to 524.2 nm after 30 min. The absorbance ratio A_{620}/A_{LSPR} increased from 0.126 to 0.328 after ions addition, which suggests an increase of the aggregation state of Au NPs. The ssDNA band at 256 nm is present in both spectra. However the intensity of the spectrum bands decreased after the addition of the cations, including the ssDNA band. Moreover a new band appeared at 211 nm. These changes in the absorption of ssDNA could indicate that the addition of these salts led to changes in the conformation of aptamer due to the release of some ssDNA from the surface of Au NPs, but in a low extension.
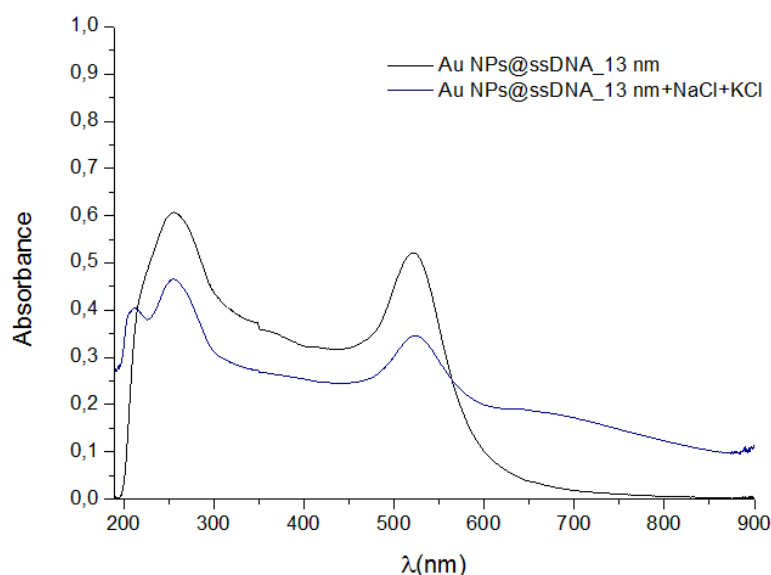
Figure 33: UV-vis spectra of Au NPs@ssDNA and Au NPs@ssDNA+NaCl+KCl after 30 minutes of salts contact (trial #2).

As mentioned in **section 3.9**, following the recommendations of the aptamer fabricant, the buffer used to prepare ssDNA solutions contained EDTA, in order to avoid interferences of resuspended ssDNA with cations, owing its chelating capacity of EDTA. It is expected that EDTA molecules in the buffer will chelate part of the cations Na^+ and K^+, preventing strong aggregation of Au NPs. The resuspension of aptamer modified Au NPs in Tris-HCl without EDTA was not tested due to time limitations.

4 Results and discussion

Table 9: Experimental conditions and the variation of A_{620}, A_{LSPR}, A_{620}/A_{LSPR} of AuNPs@ssDNA and AuNPs@ssDNA+NaCl+KCl (trials #1 to-#6).

Trial		AuNPs@ssDNA			AuNPs@ssDNA+NaCl+KCl (before CRP addition)				
	Contact Time* (h)	A_{620}	A_{LSPR} $(\lambda_{LSPR})nm$	A_{620}/A_{LSPR}	C_{NaCl} (mM)	C_{KCl} (μM)	A_{620}	A_{LSPR} $(\lambda_{LSPR})nm$	A_{620}/A_{LSPR}
1	48	0.0659	0.521 (521.2)	0.126	0.125[1]	0.144[1]	0.191	0.345 (524.1)	0.554
2	48	0.0659	0.521 (521.2)	0.126	0.125[2]	0.144[2]	0.103	0.345 (523.6)	0.328
3	24	0.149	0.447 (522.7)	0.333	0.125[1]	0.144[1]	0.234	0.237 (637.9)	0.98 (aggregate state)
4	24	0.169	0.457 (522.2)	0.369	0.050[5]	0.163[5]	0.275	0.446 (526.0)	0.617
5	24	0.149	0.447 (522.7)	0.333	0.041[3]	0.158[3]	0.249	0.405 (525.1)	0.601
6	24	0.149	0.447 (522.7)	0.333	0.034[4]	0.133[4]	0.228	0.437 (524.1)	0.523

* contact time between the aptamer and AuNPs during the functionalization step, prior the addition of NaCl and KCl

[1] 177 μL NaCl (1.01 mM) + 2 μL KCl (0.103 mM) added to 1.25 mL AuNPs@ssDNA

[2] 148 μL NaCl (1.01 mM) + 1.68 μL KCl (0.103 mM) added to 1.05 mL AuNPs@ssDNA

[3] 177 μL NaCl (1.01 mM) + 2 μL KCl (0.103 mM) added to 1.25 mL AuNPs@ssDNA

[4] 63.2 μL NaCl (1.01 mM) + 2 μL KCl (0.103 mM) added to 1.20 mL AuNPs@ssDNA

[5] 52.4 μL NaCl (1.01 mM) + 2 μL KCl (0.103 mM) added to 1.25 mL AuNPs@ssDNA

[6] 52.4 μL NaCl (1.01 mM) + 2 μL of KCl (0.103 mM) added to 1.50 mL AuNPs@ssDNA

Despite the presence of EDTA molecules, in some of the experiments the addition of salts caused a more marked effect on the aggregation of Au NPs. Moreover, in some cases the results show low reproducibility. For example trials #1 and #2 are replicas, performed in identical conditions, including the concentrations of salts. However, the results show significant differences in the aggregation ratio (A_{620}/A_{LSPR}) and LSPR red shift (**table 9**). The aggregation ratio increased from 0.126 to 0.554 and 0.328 for trial #1 and #2, respectively; also, the red shift caused by salts addition was from 521.2 to 524.1 and 523.6 nm, in trial #1 and #2, respectively.

In the trials #1 and #2 the Au NPs@ssDNA were obtained after, 48h contact between the Au NPs and the ssDNA. Efforts were done to reduce the time of the trial, by decreasing this contact time to 24h. However, the addition of salts, in identical molar concentration to the previous experiments, led to marked aggregation of the NPs as **figure 34** demonstrate, trial #3. The A_{620} increased from 0.149 to 0.234 and, the maximum absorbance was 0.237 at 637.9 nm leading to ratio $A_{620}/A_{637.9}$ of 0.98. The aggregation of the nanoparticles was visible and most likely due to excessive concentration of salts.

Following these results, attempts were made to obtained non-aggregated AuNPs@ssDNA+NaCl+KCl (24h contact time) by reduced the salt concentration. The salts were added in a final concentration of 0.050-0.034 mM (NaCl) and 0.163-0.133 μM (KCl) in trials #4, #5 and #6. No visible aggregation of Au NPs was noticed in these experiments, after 30 minutes.

Noteworthy trials #3 and #5 (**table 9**) were performed starting from equal volume of Au NPs@ssDNA (1.25 mL) and only differed in salts concentration. Trail #3 was performed with 0.125 mM of NaCl and 0.144 μM KCl while in trial #5, the final concentration were 0.041 mM of NaCl and 0.158 μM KCl. This decrease in NaCl concentration combined with slight increase in KCl concentration (trial #5) allowed preventing the sudden aggregation of Au NPs@ssDNA+NaCl+KCl, and the resulting system was CRP sensitive and detected the protein.
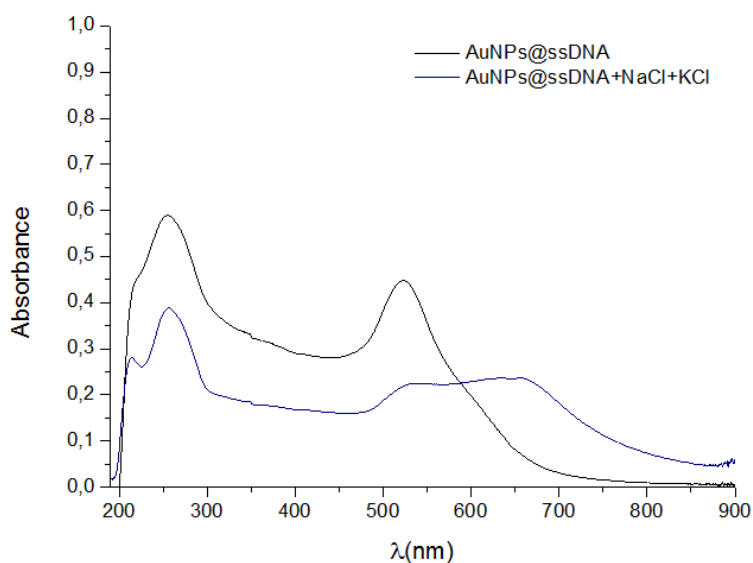
Figure 34: UV-vis spectra of AuNPs@ssDNA and AuNPs@ssDNA+NaCl+KCl (trial #3) showing marked aggregation of Au NPs, after salts addition.

Nevertheless the results (**table 9**) show that as the concentration of NaCl and KCl increased, the final ratio A_{620}/A_{LSPR} also increased, from 0.523 to 0.617, and the red-shift of the LSPR band was more marked as well (from 524.1 to 526.0 nm), for trials #6 and #4, respectivelly. This indicates that increasing the concentration of salts promotes the aggregation of Au NPs as expected.

Another key parameter seems to be the time contact between the Au NPs and the ssDNA in the preparation of Au NPs@ssDNA nanoparticles. Overall, the results demonstrate that the A620/ALSPR ratio of Au NPs@ssDNA at 24h is higher than 48h, the latter being apparently more stabilized. Consequently, studies to assess the influence of time in the optical properties of Au NPs@ssDNA should be performed in the future.

Detection of C-reactive protein

The nanoparticles AuNPs@ssDNA+NaCl+KCl were added to CRP solutions. All the experiments (#1, #2, #4, #5 and #6) described in **table 9** were successful in the detection of CRP, using the procedure described in **section 3.9**. The CRP detection was noticed by the increase of aggregation ratio after addition of CRP and NaCl. The aggregation ratio (A_{620}/A_{LSPR}) was monitored 30 minutes, for distinct CRP concentrations (**figure 35**) added to systems #1 and #2.
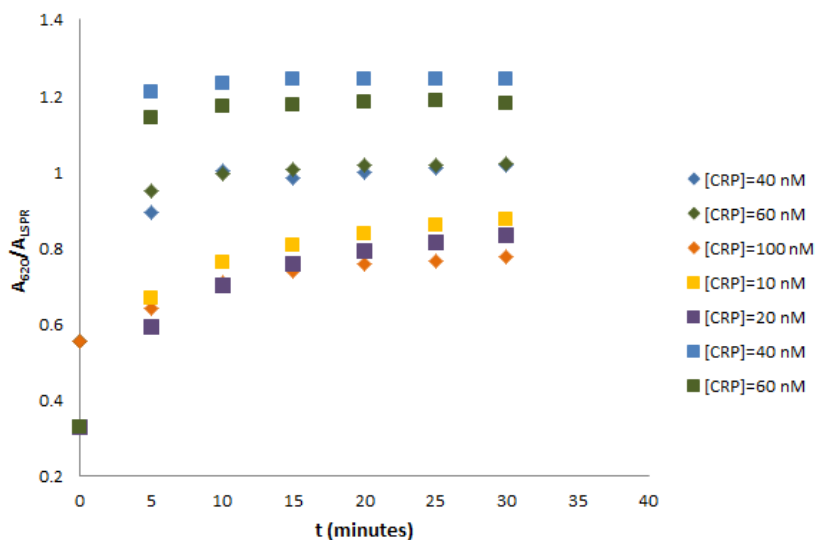
Figure 35: A_{620}/A_{LSPR} variation along 30 minutes after addition of distinct CRP concentration (from 10 to 100 nM) using Au NPs@ssDNA+NaCl+KCl (systems #1 (rhombus) and #2 (squares)) as biosensor.

For all the CRP concentrations tested the A_{620}/A_{LSPR} increased along time and had tendency to stabilize after 20 minutes. Once, ssDNA is CRP specific, in the presence of CRP the ssDNA that was at the surface of Au NPs@ssDNA nanoparticles should in principle leave to the surrounding medium and preferentially form a complex with CRP. This complex assumes a G4 structure that

is stabilized by the cations: K^+ and Na^+ previously added. As consequence the Au NPs without the ssDNA trend to aggregate, which results in an increase of the A_{620}/A_{LSPR} ratio. This ramp profile was much less pronounced for the concentrations 40 and 60 nM (in both trials #1 and #2) indicating faster Au NPs aggregation in these conditions. However these preliminary results apparently suggest the absence of direct relation between the A_{620}/A_{LSPR} values and the CRP concentration. The A_{620}/A_{LSPR} values obtained at 30 minutes were plotted against the concentration of CRP (**figure 36**). Several observations could be noticed. The maximum aggregation ratio (A_{620}/A_{LSPR}) was detected for 40 nM in both trials. Above this concentration the A_{620}/A_{LSPR} decreases, indicating a possible a maximum capacity of the material in CRP detection. Between 20 and 40 nM the A_{620}/A_{LSPR} increases with CRP concentration from the two systems tested. For further conclusions it will be necessary to perform, more trials in order to better understand the material behaviour in relation to the CRP different concentrations.
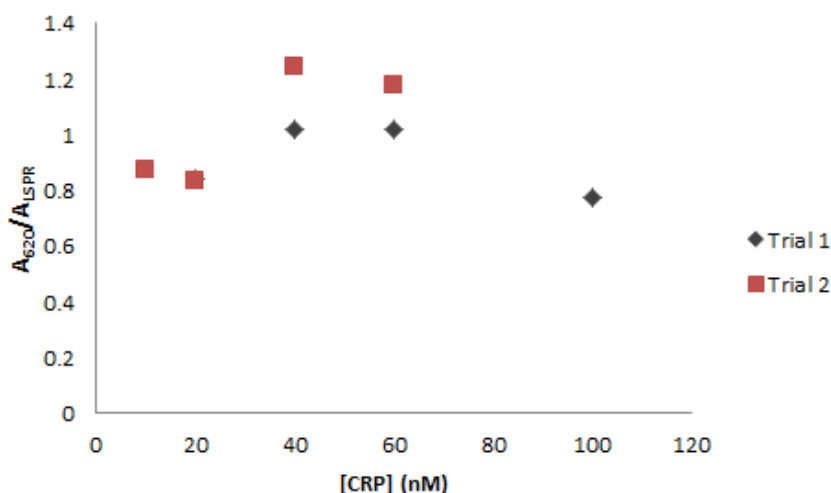
Figure 36: A_{620}/A_{LSPR} variation of different CRP concentrations (from 10 to 100 nM) using Au NPs@ssDNA+NaCl+KCl (systems #1 (rhombus) and #2 (squares)) as biosensor at 30 minutes.

Having this in mind, the AuNPs@ssDNA+NaCl+KCl from trials #4, #5 and #6 were also tested in CRP detection, in a narrower CRP concentration range (20 to 60 nM).

Figure 37 compares the variation of A_{620}/A_{LSPR} with time for trials #5 and #6, tested with different CRP concentrations. For all experiments the A_{620}/A_{LSPR} increases with time and stabilizes after 20-30 minutes. Overall A_{620}/A_{LSPR} values are higher in trial #5 than in #6 for identical CRP concentration owing to differences in salt concentration, which was higher in #5 (**table 9**). The A_{620}/A_{LSPR} values obtained at 20 and 30 min (trial #5 and #6, respectively) were plotted against the CRP concentration (**figure 38**). In the Au NPs system #6 the aggregation ratio
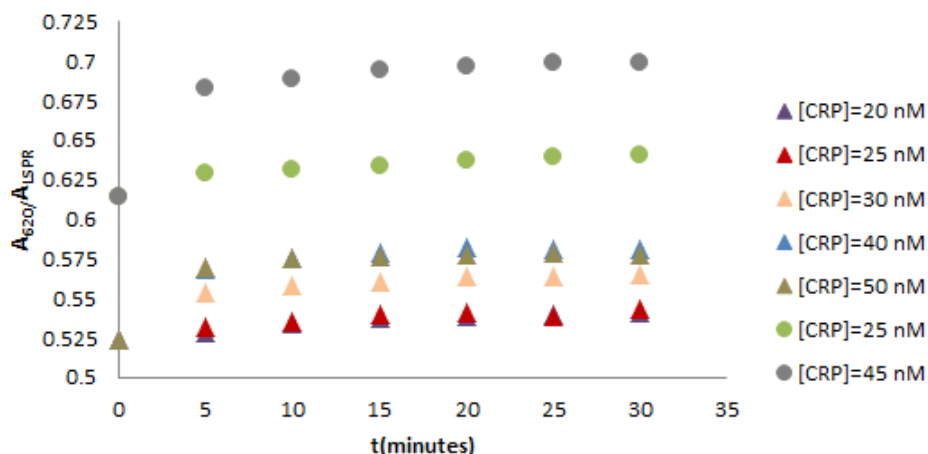
Figure 37: A_{620}/A_{LSPR} variation along 30 minutes after addition of distinct concentrations of CRP from (20 to 50 nM) using AuNPs@ssDNA+NaCl+KCl (systems #5 (circles) and #6 (triangles)) as biosensor.

seems to increase linearly with CRP concentration, up to 40 nM CRP. Then, for higher CRP concentration (50 nM) the A_{620}/A_{LSPR} seems to decrease reached the maximum material capacity for CRP detection. A linear trend was observed with Au NPs from system #5 as well, although further experiments with distinct concentrations are required to confirm this trend.
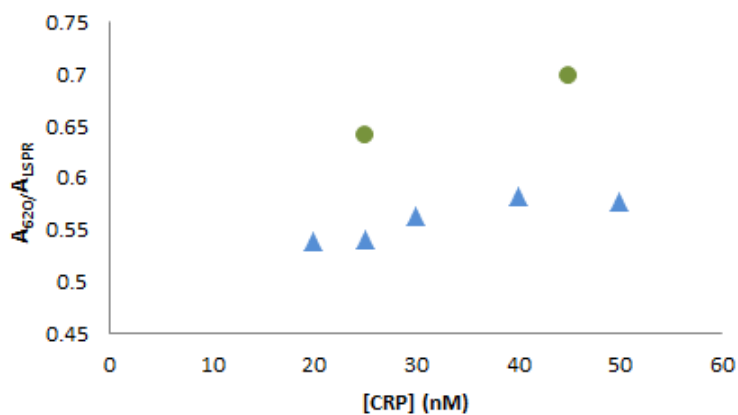
Figure 38: A_{620}/A_{LSPR} variation of different CRP concentrations (from 20 to 50 nM) using Au NPs@ssDNA+NaCl+KCl (systems #5 (circles) and #6 (triangles) as biosensor at 20 and 30 minutes, respectively.

Based on the results obtained with Au NPs from system #6 it was possible to build a calibration curve by linear regression fitting of the results obtained for 20, 25, 30 and 40 nM CRP concentrations as illustrated by **figure 39**. A correlation coefficient of 0.9382 was achieved. Even so, the number of points was not sufficient for a reliable calibration curve, able to detect CRP concentrations. More studies need to be performed in order to improve these results.

Figure 39: Aggregation ratio variation of different concentrations of CRP: 20, 25, 30 and 40 nM using AuNPs@ssDNA+NaCl+KCl (system #6) as biosensor.

Finally the CRP detection using Au NPs trial #4 was also investigated, where five CRP concentrations were tested: 20, 25, 30, 40 and 45 nM. These Au NPs contained higher concentrations of salts than those from trials #5 and #6. Again, it was verified an increase of the aggregation ratio as CRP concentration increases. **Figure 40** shows a slight increase in the aggregation ratio from 0 to 30 minutes. The effect of CRP concentration in aggregation ratio after 30 minutes was analysed. As could be seen in **figure 41** a significant increase in A_{620}/A_{LSPR} ratio from 0.678 to 0.725 was verified for when the CRP concentration increases from 20 to 25 nM. Above these concentrations, the A_{620}/A_{LSPR} ratio increases gradually with CRP concentrations. The curve presented in **figure 41** seems to show two zones with distinct linear trend. The curve was divided in calibration curve 1, for lowest CRP concentrations tested (20, 25 and 30 nM) and calibration curve 2, for higher CRP concentrations (25, 30, 40 and 45 nM) and the correlations obtained by linear regression was found to be 0.928 and 0.893, respectively. The calibration curve 1 showed a better correlation coefficient than the curve 2, however, it has only 3 points, while calibration curve 2 has 4 points.
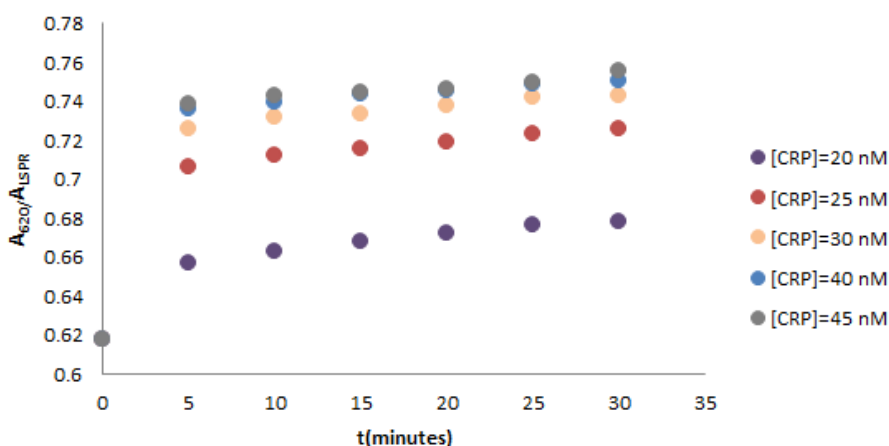
Figure 40: A_{620}/A_{LSPR} variation along 30 minutes after addition of distinct concentrations of CRP (from 20 to 45 nM) using AuNPs@ssDNA+NaCl+KCl (system #4) as biosensor.
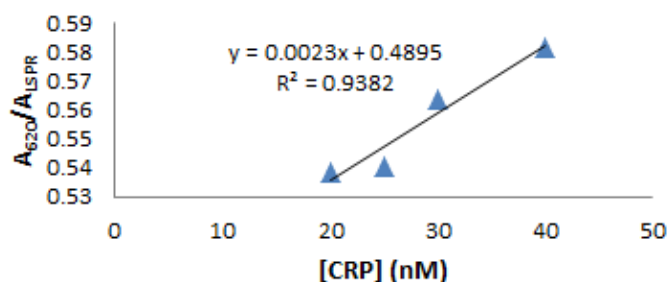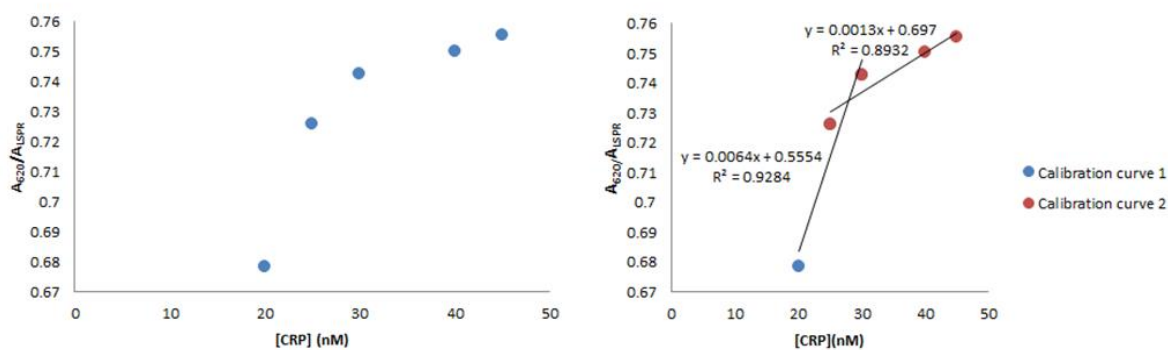
Figure 41: Aggregation ratio variation for different concentrations of CRP: 20, 25, 30, 40 and 45 nM using AuNPs@ssDNA+NaCl+KCl (system #4) as biosensor (at left) and, the correspondent linear fitting (curves 1 and 2) (at right).

These calibration curves were indicative results that needed to be replicated. From all trials described for the CRP detection only the experimental described in **section 3.9** (trial #1) showed reproducibility (trial #2) most likely to higher stabilization of Au NPs@ssDNA due to long timer contact between Au NPs and ssDNA.

5   Conclusions and future work

Conclusions and future work

This dissertation investigated novel strategies for the surface functionalization and bioconjugation of Au NPs aiming to obtain gold nanoparticles with high affinity to CRP protein that could be used in the development of a simple and highly sensitive biosensor of CRP. Two distinct strategies were investigated: the covalent coupling of cytidine 5'diphosphocholine (CDP) to functionalized Au NPs and the non-covalent surface modification of Au NPs with an aptamer (ssDNA) that is specific for CRP.

All the Au NPs bioconjugated with CDP suffered an exhaustive study of characterization using different experimental techniques. The results show that CDP was successfully attached to the surface of Au NPs. Also, the functionalization of Au NPs with aptamer was well-succeeded. The Au NPs@ssDNA, however were not studied regarding its surface charge (zeta potential) and hydrodynamic diameter (DLS), due to time limitations. The latter functionalization (with aptamer) was more straightforward as it requires less synthesis steps than is the covalent attachment of CDP. Nevertheless in the case of aptamer functionalized Au NPs (Au NPs@ssDNA), addition of salts (NaCl and KCl) is required for CRP biodetection, which reveal to be a very critical step in the stability of Au NPs.

Among Au NPs bioconjugated with CDP, the best results for CRP detection were obtained Au NPs@MUDA@CDP_40nm nanoparticles. For this system it was possible to find a linear correlation coefficient (R^2=0.9425) between CRP concentration and the aggregation ratio of Au NPs (A_{620}/A_{LSPR}) measured 5 minutes after CRP contact. This relation was valid for CRP concentration range between 20 and 50 nM. Although the results are promising, further tests are needed in order to assess the reproducibility of CRP detection using this material. Moreover other CDP bioconjugated Au NPs that were prepared in the frame of this work but were not tested in detection due to time limitations (Au NPs@MUDA@CDP_10nm and Au NPs@MPA@CDP_40nm) should be investigated for detection of CRP.

Au NPs@ssDNA nanoparticles were also successfully used to detect CRP. Under specific salt concentration conditions, a linear relation between CRP concentration and the aggregation ratio of Au NPs (A_{620}/A_{LSPR}) could also be establishing. For example, under the conditions of trial #6, this relation was found for CRP concentrations ranging from 20 to 40 nM with a correlation coefficient of 0.9382. Nevertheless longer periods (20-30 minutes) were needed to obtain stable aggregation values. In addition the linear relation varied with small changes on the concentrations of added salts (NaCl and KCl). Thus this parameter should be exquisitely controlled in order to get reliable and reproducible detection results. Another parameter that should be carefully investigated is the time needed for preparing Au NPs @ssDNA as it seems to have a direct

5 Conclusions and future work

influence on aggregation ratio before and after the addition of salts and consequently, during CRP detection.

In addition, for applied the synthetized CDP bioconjugated Au NPs and modified aptamer Au NPs in biological samples (blood plasma), these materials should be tested against interfering proteins such as interleukin (IL)-1β, IL-6, IL-8, immunoglobulin G and albumin.

The work developed in this dissertation was exploratory in nature and aimed to develop bionanomaterials capable of detecting C-reactive protein, a biomarker for cardiovascular diseases. More studies are necessary in the development of functionalized gold nanoparticles for CRP detection in order to obtain a valuable biosensor.

6 Bibliography

6 Bibliography

Bibliography

1. World Health Organization. Data and statistics of cardiovascular diseases in Europe. (2016). at <http://www.euro.who.int/en/health-topics/noncommunicable-diseases/cardiovascular-diseases/data-and-statistics> accessed at 22/10/2016.

2. Santulli, G. Epidemiology of cardiovascular disease in the 21 st Century : Updated numbers and updated facts. *J. Cardiovasc. Dis.* **1,** 1–2 (2013).

3. World Health Organization. Cardiavascular Diseases. (2016). at <http://www.who.int/mediacentre/factsheets/fs317/en/> accessed at 22/10/2016.

4. Piepoli, M. F. *et al.* 2016 European Guidelines on cardiovascular disease prevention in clinical practice. *Eur. Heart J.* **37,** 2315–2381 (2016).

5. Ridker, P. M. A test in context: High-Sensitivity C-reactive protein. *J Am Coll Cardiol.* **67,** 712–723 (2016).

6. Wilson, P. W. F. *et al.* Prediction of coronary heart disease using risk factor categories. *Circulation* **97,** 1837–1847 (1998).

7. D'Agostino, R. B. *et al.* General cardiovascular risk profile for use in primary care: The Framingham heart study. *Circulation* **117,** 743–753 (2008).

8. Cahill, L. E. *et al.* New and Emerging Biomarkers in Cardiovascular Disease. *Curr. Diab. Rep.* **15,** 88-103 (2015).

9. Paynter, N. P. *et al.* Cardiovascular disease risk prediction in women: Is there a role for novel biomarkers? *Clin. Chem.* **60,** 88–97 (2014).

10. Vance, S. A. & Sandros, M. G. Zeptomole detection of C-reactive protein in serum by a nanoparticle amplified surface plasmon resonance imaging aptasensor. *Sci. Rep.* **4,** 5129-36 (2014).

11. Averna, M. & Noto, D. Clinical utility of novel biomarkers for cardiovascular disease risk stratification. *Intern. Emerg. Med.* **7,** S263-270 (2012).

12. Assimes, T. L. *et al.* Susceptibility locus for clinical and subclinical coronary artery disease at chromosome 9p21 in the multi-ethnic ADVANCE study. *Hum. Mol. Genet.* **17,** 2320–2328 (2008).

13. Pasmant, E. *et al.* Characterization of a germ-line deletion, including the entire INK4/ARF locus, in a melanoma-neural system tumor family: Identification of ANRIL, an antisense noncoding RNA whose expression coclusters with ARF. *Cancer Res.* **67,** 3963–3969 (2007).

14. Patel, R. S. *et al.* The chromosome 9p21 risk locus is associated with angiographic severity

and progression of coronary artery disease. *Eur. Heart J.* **31,** 3017–3023 (2010).

15. Huber, S. A. *et al.* Interleukin-6 Exacerbates Early Atherosclerosis in Mice. *Arterioscler. Thromb. Vasc. Biol.* **19,** 2364–2367 (1999).

16. Ait-Oufella, H. *et al.* Recent advances on the role of cytokines in atherosclerosis. *Arterioscler. Thromb. Vasc. Biol.* **31,** 969–979 (2011).

17. Anderson, D. R. *et al.* IL-6 and its receptors in coronary artery disease and acute myocardial infarction. *Cytokine* **62,** 395–400 (2013).

18. BD Biosciences Pharmingen. Technical Data Sheet BD OptEIA ™ Human IL-1 b ELISA Set. 1–2 (2015).

19. Jousilahti, P. *et al.* The association of c-reactive protein, serum amyloid a and fibrinogen with prevalent coronary heart disease - Baseline findings of the PAIS project. *Atherosclerosis* **156,** 451–456 (2001).

20. Johnson, B. D. *et al.* Serum Amyloid A as a Predictor of Coronary Artery Disease and Cardiovascular Outcome in Women: The National Heart, Lung, and Blood Institute-Sponsored Women's Ischemia Syndrome Evaluation (WISE). *Circulation* **109,** 726–732 (2004).

21. Mineo, C. & Shaul, P. W. Novel biological functions of high-density lipoprotein cholesterol. *Circ. Res.* **111,** 1079–1090 (2012).

22. Weichhart, T. *et al.* Serum Amyloid A in Uremic HDL Promotes Inflammation. *J. Am. Soc. Nephrol.* **23,** 934–947 (2012).

23. Zewinger, S. *et al.* Serum amyloid A: High-density lipoproteins interaction and cardiovascular risk. *Eur. Heart J.* **36,** 3007–3016 (2015).

24. Dade Behring. N Latex SAA. (2003) <http://www.medcorp.com.br/medcorp/upload/downloads/Soro%20Amiloide%20A_2006 329114622.pdf> accessed at 5/02/2017

25. Tillett, Wi. S. & Thomas Francis, J. Serological reactions in pneumonia with a non-protein somatic fraction of *Pneumococcus*. *J Exp Med.* **52,** 561–571 (1930).

26. Pepys, M. B. & Hirschfield, G. M. C-reactive protein: a critical update. *J Clin Invest.* **7,** 169-177 (2003).

27. Thompson, D. *et al.* The phsiological structure of human C-reactive protein and its complex with phosphocholine. *Struct. London Engl. 1993* **7,** 169–177 (1999).

28. Shrive AK, Cheetham GM, Holden D, Myles DA, Turnell WG, Volanakis JE, Pepys MB, Bloomer AC, G. T. Human C-reactive protein. *PDBe* (1996). at

6 Bibliography

<http://www.ebi.ac.uk/pdbe/entry/pdb/1gnh> accessed at 26/10/2016.

29. Vashist, S. K. *et al.* Bioanalytical advances in assays for C-reactive protein. *Biotechnol. Adv.* **34,** 272–290 (2016).

30. Soeki, T. & Sata, M. Inflammatory Biomarkers and Atherosclerosis. *Int. Heart J.* **57,** 134–9 (2016).

31. Ridker, P. M. High-sensitivity C-reactive protein, inflammation, and cardiovascular risk: From concept to clinical practice to clinical benefit. *Am. Heart J.* **148,** S19-26 (2004).

32. Goldstein, J. A. *et al.* Relation of number of complex coronary lesions to serum C-reactive protein levels and major adverse cardiovascular events at one year. *Am. J. Cardiol.* **96,** 56–60 (2005).

33. Lakoski, S. G. *et al.* Gender and C-reactive protein: Data from the Multiethnic Study of Atherosclerosis (MESA) cohort. *Am. Heart J.* **152,** 593–598 (2006).

34. Ridker, P. M. *et al.* Hormone Replacement Therapy and Increased Plasma Concentration of C-Reactive Protein. *Circulation* **100,** 713–2891 (1999).

35. Saito, I. *et al.* C-reactive protein and cardiovascular disease in east asians: A systematic review. *Clin. Med. Insights Cardiol.* **8,** 35–42 (2014).

36. Koenig, W. *et al.* C-reactive protein modulates risk prediction based on the Framingham Score - Implications for future risk assessment: Results from a Large Cohort Study in Southern Germany. *Circulation* **109,** 1349–1353 (2004).

37. Pearson, T. A. *et al.* Markers of inflammation and cardiovascular disease: Application to clinical and public health practice: A statement for healthcare professionals from the centers for disease control and prevention and the American Heart Association. *Circulation* **107,** 499–511 (2003).

38. FG Hage. C-reactive protein and hypertension. *J. Hum. Hypertens.* **28,** 410–415 (2014).

39. Paffen, E. & deMaat, M. P. M. C-reactive protein in atherosclerosis: A causal factor? *Cardiovasc. Res.* **71,** 30–39 (2006).

40. Bian, F. *et al.* C-reactive protein promotes atherosclerosis by increasing LDL transcytosis across endothelial cells. *Br. J. Pharmacol.* **171,** 2671–2684 (2014).

41. Chuang, S. Y. *et al.* C-reactive protein predicts systolic blood pressure and pulse pressure but not diastolic blood pressure: The cardiovascular disease risk factors two-township study. *Am. J. Hypertens.* **26,** 657–664 (2013).

42. Ridker, P. M. & Cook, N. Clinical usefulness of very high and very low levels of C-reactive protein across the full range of Framingham Risk Scores. *Circulation* **109,** 1955–

1959 (2004).

43. Auer, J. C-reactive protein in patients with acute myocardial infarction * Response. *Circulation* **109,** 20 (2004).

44. Tanaka, A. *et al.* Multiple plaque rupture and C-reactive protein in acute myocardial infarction. *J. Am. Coll. Cardiol.* **45,** 1594–1599 (2005).

45. Wensley, F. *et al.* Association between C reactive protein and coronary heart disease: Mendelian randomisation analysis based on individual participant data. *Br. Med. J.* **342,** 1–8 (2011).

46. Bouman, A. C. *et al.* Markers of coagulation, fibrinolysis and inflammation in relation to post-thrombotic syndrome. *J. Thromb. Haemost.* **10,** 1532–1538 (2012).

47. Sara, J. D. *et al.* High sensitivity C reactive protein is an independent marker of coronary endothelial dysfunction in patients with nonobstructive coronary artery disease. *J. Am. Coll. Cardiol.* **67,** 360 (2016).

48. Sklavou, R. *et al.* Variation of serum C-reactive protein (CRP) over time in pediatric cancer patients with febrile illness and its relevance to identified pathogen. *Clin. Biochem.* **45,** 1178–1182 (2012).

49. Stago BNL. Smart hs CRP test kit. (2017). at <http://catalog.stago-bnl.com/fr/product/point_of_care/reactifs/1331/smart_hs_crp_test_kit> accessed at 5/01/2017.

50. Sung, H. J. *et al.* Evaluation of Denka-Seiken turbidimetric high-sensitivity C-reactive protein assay. *Clin. Chem. Lab. Med.* **40,** 840–845 (2002).

51. Hutchinson, K. C-reactive protein in serum by nephelometry. *National Health and Nutrition Examination Survey* 1–12 (2002).

52. Beckman & Coulter. Higher sensitivity cardiac C-reactive protein <https://www.beckmancoulter.com/wsrportal/techdocs?docname=cis/A42557/AE/EN_CRPH%20(CARDIAC).pdf> (2015).

53. Thermo Fisher Scientific. Human C-Reactive Protein ELISA Kit. 24–25 (2016). at <https://tools.thermofisher.com/content/sfs/manuals/MAN0004010_KHA0031_Hu_CRP_PI.pdf> accessed at 5/11/2016.

54. Josephy, D. *et al.* The Horseradish Peroxidase-catalyzed Oxidation of 3,5,3',5'-Tetramethylbenzidine. *J. Biol. Chem.* **257,** 3669–3675 (1982).

55. Beckman Coulter. Higher sensitivity cardiac C-reactive protein <https://www.beckmancoulter.com/wsrportal/techdocs?docname=cis/A42557/AE/EN_CR

PH%20(CARDIAC).pdf> (2011).

56. Collet-Cassart, D. *et al.* A quantitative C-reactive protein assay using latex agglutination in microtiter plates. *J. Immunol. Methods* **125,** 137–141 (1989).

57. Fakanya, W. M. & Tothill, I. E. Detection of the inflammation biomarker C-reactive protein in serum samples: Towards an Optimal Biosensor Formula. *Biosensors* **4,** 340–357 (2014).

58. Yang, S. F. *et al.* Detection of C-reactive protein based on a magnetic immunoassay by using functional magnetic and fluorescent nanoparticles in microplates. *Analyst* **139,** 5576–5581 (2014).

59. Rao, C. N. R. *et al.* Nanomaterials - An Introduction. *Chem. Nanomater.* **1,** 1–11 (2005).

60. Pavassiliou, G. C. Optical properties of small inorganic and organic metal particles. *Prog. Solid State Chem.* **12,** 185–271 (1980).

61. Wu, B. *et al.* Detection of C-reactive protein using nanoparticle-enhanced surface plasmon resonance using an aptamer-antibody sandwich assay. *Chem. Commun.* **52,** 3568–3571 (2016).

62. Zhang, X. *et al.* An ultrasensitive label-free immunoassay for C-reactive protein detection in human serum based on electron transfer. *Anal. Methods* **8,** 6202–6207 (2016).

63. Raj, V. & Sreenivasan, K. Selective detection and estimation of C-reactive protein in serum using surface-functionalized gold nano-particles. *Anal. Chim. Acta* **662,** 186–192 (2010).

64. Martins, M. A. & Trindade, T. Os nanomateriais e a descoberta de novos mundos na bancada do químico. *Quim. Nova* **35,** 1434–1446 (2012).

65. Page Faulk, W. & Malcolm Taylor, G. An immunocolloid method for the electron microscope. *Immunochemistry* **8,** 1081–1083 (1971).

66. Boisselier, E. & Astruc, D. Gold nanoparticles in nanomedicine: preparations, imaging, diagnostics, therapies and toxicity. *Chem. Soc. Rev.* **38,** 1759–1782 (2009).

67. Niidome, Y. *et al.* Anisotropic Gold-based Nanoparticles: Preparation, Properties, and Applications. *Chem. Lett.* **45,** 488–498 (2016).

68. Hayat, M. A. Colloidal gold: Principles, methods, and applications. *Micron Microsc. Acta* **21,** 193 (1989).

69. Ghosh, P. *et al.* Gold nanoparticles in delivery applications. *Adv. Drug Deliv. Rev.* **60,** 1307–1315 (2008).

70. Shukla, R. *et al.* Biocompatibility of gold nanoparticles and their endocytotic fate inside

the cellular compartment: A microscopic overview. *Langmuir* **21,** 10644–10654 (2005).

71. Faraday, M. The Bakerian lecture: experimental relations of gold (and other metals) to light. *R. Soc. London* **147,** 145–181 (1857).

72. Henglein, A. Physicochemical properties of small metal particles in solution: 'Microelectrode' reactions, chemisorption, composite metal particles, and the atom-to-metal transition. *J. Phys. Chem.* **97,** 5457–5471 (1993).

73. Liz-Marzán, L. M. Nanometals formation and color. *Mater. Today* **7,** 26–31 (2004).

74. Liz-Marzán, L. M. Tailoring surface plasmons through the morphology and assembly of metal nanoparticles. *Langmuir* **22,** 32–41 (2006).

75. Ung, T. *et al.* Gold nanoparticle thin films. *Colloids Surfaces A Physicochem. Eng. Asp.* **202,** 119–126 (2002).

76. Yang, Y. *et al.* Controlling the aggregation behavior of gold nanoparticles. *Mater. Sci. Eng. B Solid-State Mater. Adv. Technol.* **140,** 172–176 (2007).

77. Baptista, P. V. *et al.* Gold-nanoparticle-probe-based assay for rapid and direct detection of *Mycobacterium tuberculosis* DNA in clinical samples. *Clin. Chem.* **52,** 1433–1434 (2006).

78. Saha, K. *et al.* Gold nanoparticles in chemical and biological sensing. *Chem. Rev.* **112,** 2739–2779 (2012).

79. Nguyen, D. T. *et al.* Controlled synthesis and biomolecular probe application of gold nanoparticles. *Micron* **42,** 207–227 (2011).

80. Zhao, P. *et al*. State of the art in gold nanoparticle synthesis. *Coord. Chem. Rev.* **257,** 638–665 (2013).

81. Shah, M. *et al.* Biological applications of gold nanoparticles. *J. Nanosci. Nanotechnol.* **14,** 344–362 (2014).

82. Brust, M. *et al.* Synthesis of Thiol-derivatised Gold Nanoparticles in Two-phase Liquid-Liquid System. *J. Chem. Educ.* **0,** 801–802 (1994).

83. Kimling, J. *et al.* Turkevich method for gold nanoparticle synthesis revisited. *J. Phys. Chem. B* **110,** 15700–15707 (2006).

84. Frens, G. Controlled nucleation for the regulation of the particle size in monodisperse gold suspensions. *Nat. Phys. Sci.* **241,** 20–22 (1973).

85. Brown, K. R. & Natan, M. J. Hydroxylamine seeding of colloidal Au nanoparticles in solution and on surfaces. *Langmuir* **14,** 726–728 (1998).

86. Corbierre, M. K. *et al.* Polymer-Stabilized Gold Nanoparticles with High Grafting Densities. *Langmuir* **20,** 2867–2873 (2004).

87. Wangoo, N. *et al.* Facile synthesis and functionalization of water-soluble gold nanoparticles for a bioprobe. *Anal. Chim. Acta* **610,** 142–148 (2008).

88. Turkevich, J. *et al.* A study of the nucleation and growth process in the synthesis of colloidal gold. *Discuss. Faraday Soc.* **11,** 55–75 (1951).

89. Ho, L. C. *et al.* Sensitive and selective gold nanomaterials based optical probes. *J. Chinese Chem. Soc.* **61,** 163–174 (2014).

90. Sivaraman, S. K. *et al.* Monodisperse sub-10nm gold nanoparticles by reversing the order of addition in Turkevich method - The role of chloroauric acid. *J. Colloid Interface Sci.* **361,** 543–547 (2011).

91. Yeh, Y.-C. *et al.* Gold nanoparticles: preparation, properties, and applications in bionanotechnology. *Nanoscale* **4,** 1871–80 (2012).

92. Tanaka, R. *et al.* A novel enhancement assay for immunochromatographic test strips using gold nanoparticles. *Anal. Bioanal. Chem.* **385,** 1414–1420 (2006).

93. Chammem, H. *et al.* Surface plasmon resonance for C-reactive protein detection in human plasma. *J. Biomater. Nanobiotechnol.* **5,** 153–158 (2014).

94. Mishra, S. K. *et al.* Biofunctionalized gold nanoparticle-conducting polymer nanocomposite based bioelectrode for CRP detection. *Appl. Biochem. Biotechnol.* **174,** 984–997 (2014).

95. Iwasaki, Y. *et al.* Label-free detection of C-reactive protein using highly dispersible gold nanoparticles synthesized by reducible biomimetic block copolymers. *Chem. Commun. (Camb).* **50,** 5656–8 (2014).

96. Islam, M. S. & Kang, S. H. Chemiluminescence detection of label-free C-reactive protein based on catalytic activity of gold nanoparticles. *Talanta* **84,** 752–758 (2011).

97. Wei, H. *et al.* Simple and sensitive aptamer-based colorimetric sensing of protein using unmodified gold nanoparticle probes. *Chem. Commun.* **0,** 3735–3737 (2007).

98. Wu, B. *et al.* A simple label-free aptamer-based method for C-reactive protein detection. *Anal. Methods* **8,** 4177–4180 (2013).

99. Chammem, H. *et al.* Functionalised magnetic beads on gold surface for C-reactive protein detection. *Int. J. Nanotechnol.* **12,** 552–561 (2015).

100. Vashist, S. K. *et al.* Surface plasmon resonance-based immunoassay for human C-reactive protein. *Analyst* **140,** 4445–52 (2015).

101. Kitayama, Y. & Takeuchi, T. Localized surface plasmon resonance nanosensing of C-reactive protein with poly(2-methacryloyloxyethyl phosphorylcholine)-grafted gold

nanoparticles prepared by surface-initiated atom transfer radical polymerization. *Anal. Chem. (Washington, DC, U. S.)* **86,** 5587–5594 (2014).

102. National Center for Biotechnology Information. Phosphocholine. (2016). at <https://pubchem.ncbi.nlm.nih.gov/compound/phosphocholine#section=Top> accessed at 3/11/2016.

103. National Center for Biotechnology Information. O-Phosphorylethanolamine. (2016). at <https://pubchem.ncbi.nlm.nih.gov/compound/1015#section=Top> accessed at 3/11/2016.

104. Gopinath, S. C. B. *et al.* Aptamer-based ' point-of-care testing '. *Biotechnol. Adv.* **34,** 198–208 (2016).

105. Yuce, M. *et al.*Trends in Aptamer Selection Methods and Applications. *Analyst* **140,** 5379–5399 (2015).

106. Algarra, M. *et al.* Current analytical strategies for C-reactive protein quantification in blood. *Clin. Chim. Acta* **415,** 1–9 (2013).

107. Artemyev, D. N. *et al. Blood proteins analysis by Raman spectroscopy method. Biophotonics: Photonic Solutions for Better Health Care V* **9887,** Y1-8 (2016).

108. Lekeufack, D. D. *et al.* Core–shell Au@(TiO2, SiO2) nanoparticles with tunable morphology. *Chem. Commun.* **46,** 4544-46 (2010).

109. Haiss, W. *et al.* Determination of Size and Concentration of Gold Nanoparticles from UV − Vis Spectra. *Anal. Chem.* **79,** 4215–4221 (2007).

110. Royal Society of Chemistry. 11-Mercaptoundecanoic acid. (2015). at <http://www.chemspider.com/Chemical-Structure.473151.html> accessed at 14/12/2016.

111. Chang, C. W. *et al.* Selective extraction of melamine using 11-mercaptoundecanoic acid-capped gold nanoparticles followed by capillary electrophoresis. *J. Chromatogr. A* **1217,** 7800–7806 (2010).

112. Huang, C.-C. & Chang, H.-T. Parameters for selective colorimetric sensing of mercury(II) in aqueous solutions using mercaptopropionic acid-modified gold nanoparticles. *Chem. Commun.***0,** 1215–1217 (2006).

113. Hermanson, G. T. *Bioconjugation techniques*. (Elsevier, 2008).

114. Li, H. & Rothberg, L. J. Label-free colorimetric detection of specific sequences in genomic DNA amplified by the polymerase chain reaction. *J. Am. Chem. Soc.* **126,** 10958–10961 (2004).

115. Li, L. & Li, W. Colorimetric kinetic determination of potassium ions based on the use of a specific aptamer and catalytically active gold nanoparticles. *Microchim. Acta* **182,** 2307–

2312 (2015).

116.   He, H. *et al.* Unusual sequence length-dependent gold nanoparticles aggregation of the ssDNA sticky end and its application for enzyme-free and signal amplified colorimetric DNA detection. *Sci. Rep.* **6,** 30878 (2016).

117.   Li, H. & Rothberg, L. Colorimetric detection of DNA sequences based on electrostatic interactions with unmodified gold nanoparticles. *Proc. Natl. Acad. Sci. USA* **101,** 14036–14039 (2004).

118.   Malvern Instruments. Polydispersity – what does it mean for DLS and chromatography? (2017). at <http://www.materials-talks.com/blog/2014/10/23/polydispersity-what-does-it-mean-for-dls-and-chromatography/> accessed at 29/01/2017.

119.   Royal Society of Chemistry. 3-Mercaptopropionic acid. (2015). at <http://www.chemspider.com/Chemical-Structure.6267.html> accessed at 21/03/2017.

120.   Park, J. W. & Shumaker-Parry, J. S. Structural study of citrate layers on gold nanoparticles: Role of intermolecular interactions in stabilizing nanoparticles. *J. Am. Chem. Soc.* **136,** 1907–1921 (2014).

121.   Lakshmanan, B. Infrared absorption spectrum of sodium citrate. *J. Indian Inst. Sci.* **39,** Suppl:108-120 (1968).

122.   Silverstein, R. M., Webster, F. X. & Kiemle, D. J. *Spectrometric Identification of Organic Compounds*. *Spectrometric identification of organic compounds* (John Wiley & Sons, 2006).

123.   Zhao, X. *et al.* Preparation of Alkanethiolate-Functionalized Core / Shell Fe_3O_4@ Au Nanoparticles and Its Interaction with Several Typical Target Molecules. *Anal. Chem.* **80,** 9091–9096 (2008).

124.   Amoli, B. M. *et al.* Thiocarboxylate functionalization of silver nanoparticles: effect of chain length on the electrical conductivity of nanoparticles and their polymer composites. *J. Mater. Chem.* **22,** 20048 (2012).

125.   Mathlouthi, M. *et al.* F.T.-I.R. and laser-Raman spectra of cytosine and cytidine. *Carbohydr. Res.* **146,** 1–13 (1986).

126.   Liu, X. *et al.* Extinction coefficient of gold nanoparticles with different sizes and different capping ligands. *Colloids Surfaces B Biointerfaces* **58,** 3–7 (2007).

127.   Held, P. G. Nucleic acid purity assessment using A_{260} / A_{280} Ratios. *BioTek* 1–5 (2001).

128.   Oxford Gene Tecnology. Understanding and measuring variations in DNA sample quality. (2011)<https://www.ogt.com/resources/literature/483_understanding_and_measuring_vari

ations_in_dna_sample_quality> accessed at 03/07/2017.

129.   Zhu, L.-N. *et al.* Specific recognition and stabilization of monomeric and multimeric G-quadruplexes by cationic porphyrin TMPipEOPP under molecular crowding conditions. *Nucleic Acids Res.* **41,** 4324–4335 (2013).

130.   Randazzo, A. *et al.* Circular dichroism of quadruplex structures. *Top Curr Chem* **11,** 13–35 (2012).

131.   Gattuso, H. *et al.* Circular dichroism of DNA G-quadruplexes: Combining modeling and spectroscopy to unravel complex structures. *J. Phys. Chem. B* **120,** 3113–3121 (2016).

132.   Duquette, M. L. *et al.* Intracellular transcription of G-rich DNAs induces formation of G-loops, novel structures containing G4 DNA. *Genes Dev.* **18,** 1618–1629 (2004).

133.   Chambers, V. S. *et al.* High-throughput sequencing of DNA G-quadruplex structures in the human genome. *Nat. Biotechnol.* **33,** 1–7 (2015).

134.   Williamson, J. R. *et al.* Monovalent cation-induced structure of telomeric DNA : The G - quartet model. *Cell* **59,** 871–880 (1989).

135.   Nacional center for Biotechnology Information. 3-Mercaptopropionic Acid. (2005). at <https://pubchem.ncbi.nlm.nih.gov/compound/3-mercaptopropionic_acid#section=Dissociation-Constants> accessed at 12/01/2017.

136.   The Metabolomics Innovation Centre. 11-Mercaptoundecanoic acid. (2010). at <https://www.drugbank.ca/drugs/DB08171> accessed at 12/01/2017.

137.   Weisbecker, C. S. *et al.* Molecular Self-Assembly of Aliphatic Thiols on Gold Golloids. *Langmuir* **12,** 3763–3772 (1996).

138.   Xue, Y. *et al.* Quantifying thiol-gold interactions towards the efficient strength control. *Nat. Commun.* **5,** 4348 (2014).

139.   Sigma-Aldrich. Sodium citrate tribasic dihydrate. *2017* at <http://www.sigmaaldrich.com/catalog/substance/sodiumcitratetribasicdihydrate29410613204311?lang=pt&region=PT> accessed at 15/10/2016.

140.   Sigma-Aldrich. Cytidine 5' diphosphocholine sodium salt. *2017* at <http://www.sigmaaldrich.com/catalog/product/sigma/c9880?lang=pt&region=PT> accessed at 25/11/2016.

7   Appendix

7 Appendix

A1. Surface Functionalization with MPA – Effect of MPA concentration and pH

Using the molar ratio between Au NPs/mercapto ligand that was used for the functionalization with MUDA (0.0014) [111] it was not possible to obtain stable Au NPs functionalized with 3-mercaptopropionic acid (MPA). The colloid changes to blue colour after the addition of MPA, which indicates Au NPs aggregation. Thus it was necessary to test different values of Au NPs/MPA molar ratio to find the most adequate conditions of the surface functionalization.

Different concentrations of MPA for the same concentration of Au NPs were tested in order to determine the best molar ratio for MPA. It was performed trials with different volumes of 0.04 M MPA solution (0, 10, 20, 30, 40, 50, 100, 150, and 200 μL) that were added to synthesized Au NPs_10 nm (865 μL; 2.67×10^{-4}M) for functionalization, during 2 hours. Note that the pH of MPA solution is around 3 and these tests the functionalization was performed without any further pH adjustment. As presented in **table 10** and **figure 42**, only the trial using 10 μL of MPA solution concentration of 0.04M did not induce aggregation. However, this molar quantity of MPA could not be sufficient for functionalization of Au NPs with MPA.
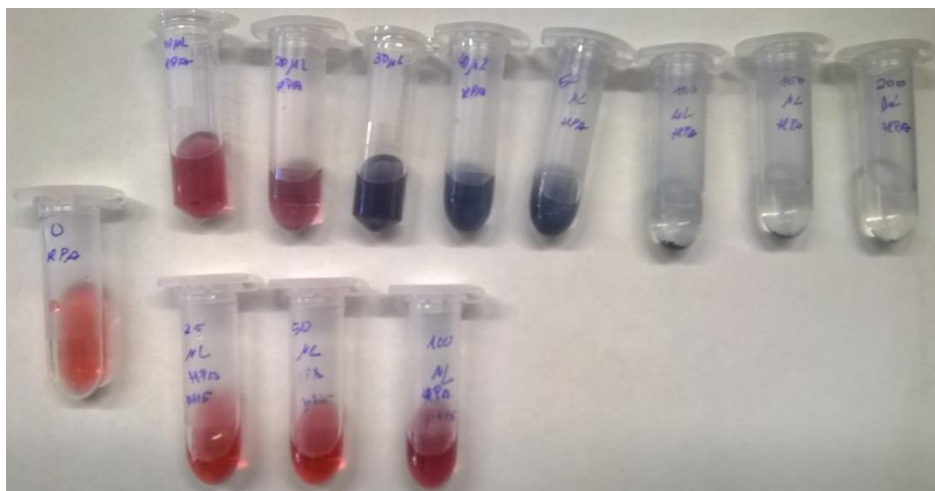
Table 10: State of gold nanoparticles after the addition of different volumes of MPA to gold nanoparticles at different pH values of MPA solution.

V(MPA) (μL)	Aggregation State AuNPs_10 nm	
	pH 3	pH 5.10
200	Aggregate	-
150	Aggregate	-
100	Aggregate	-
50	Aggregate	Not aggregate
40	Aggregate	Not aggregate
30	Aggregate	-
20	Aggregate	-
10	Not aggregate	Not aggregate
0	Not aggregate	-

The pH of the medium might affect the degree of protonation of the carboxylic acid group of mercapto ligands. The acid dissociation constant (pKa) of MPA is 4.34 [135] and pKa of MUDA is 4.95 [136]. It was verified that the pH of MUDA aqueous solutions used for functionalization was around 5 while and pH of MPA solutions was around 3. Consequently, at pH=3 of carboxylic acid groups of MPA molecules are protonated and do not promote electrostatic stabilization of Au NPs [137, 138]. Increasing pH of MPA solution, allowed the of the carboxylic acid group to obtained Au NPs that are stabilized by electrostatic repulsions. The pH of MPA solution was adjusted to 5.10.
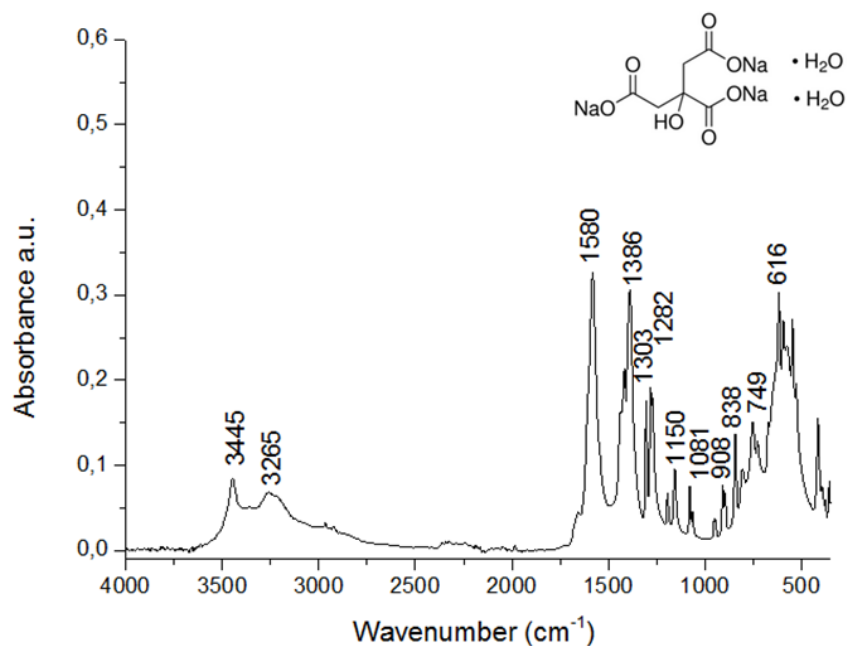
7 Appendix

For confirmation that this new MPA solution allow the functionalization of AuNPs without aggregation, different volumes (25 µL, 50 µL and 100 µL) of 0.032M MPA solution were added to 865 µL of 2.67×10^{-4} M of AuNPs. None of the trials showed aggregation, as could be observed in **figure 42**, and 50 µL of 0.032M MPA solution was selected for calculate the new molar ratio for MPA, 0.144. This ratio was used for both Au NPs_10nm and 40 nm for functionalization with MPA.
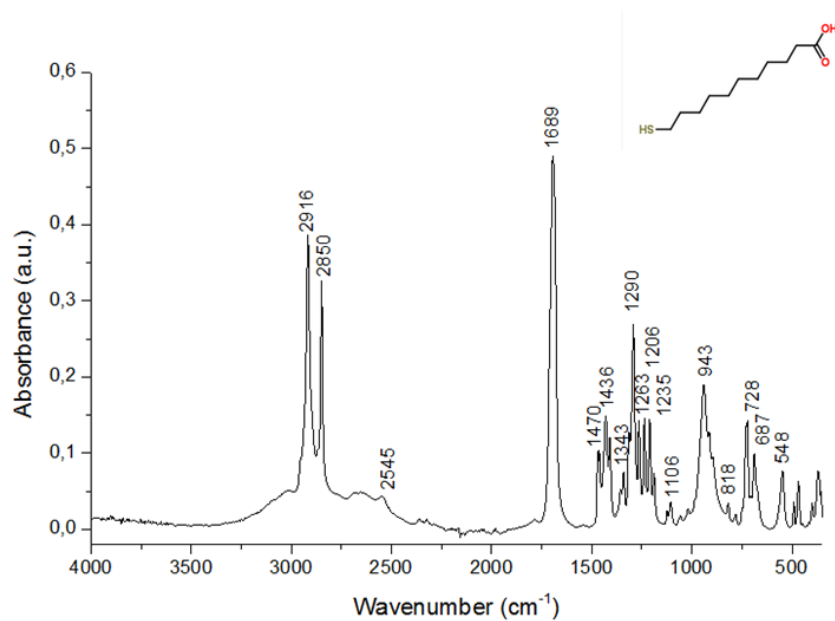

Figure 42: Photograph of the trials performed for the functionalization of gold nanoparticles with MPA, at the top using different ratios AuNPs/MPA and, at bottom using the ratio 0.144.

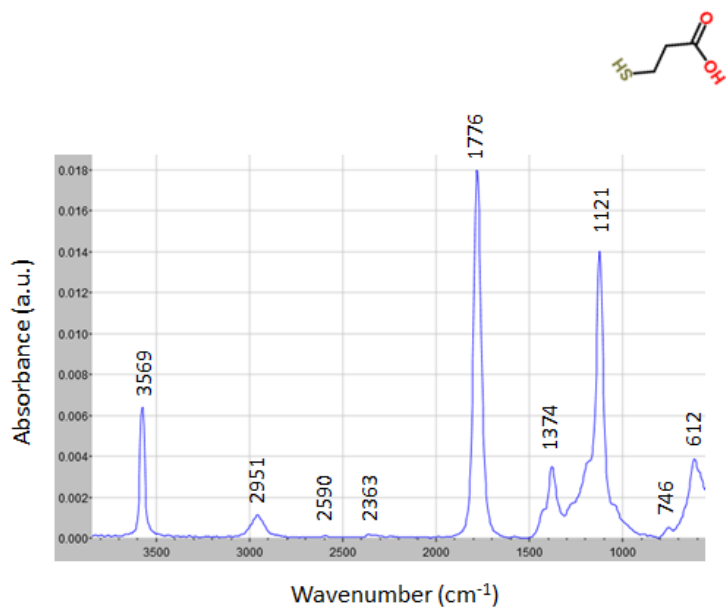## A2. FTIR spectra of sodium citrate, MPA, MUDA and CDP

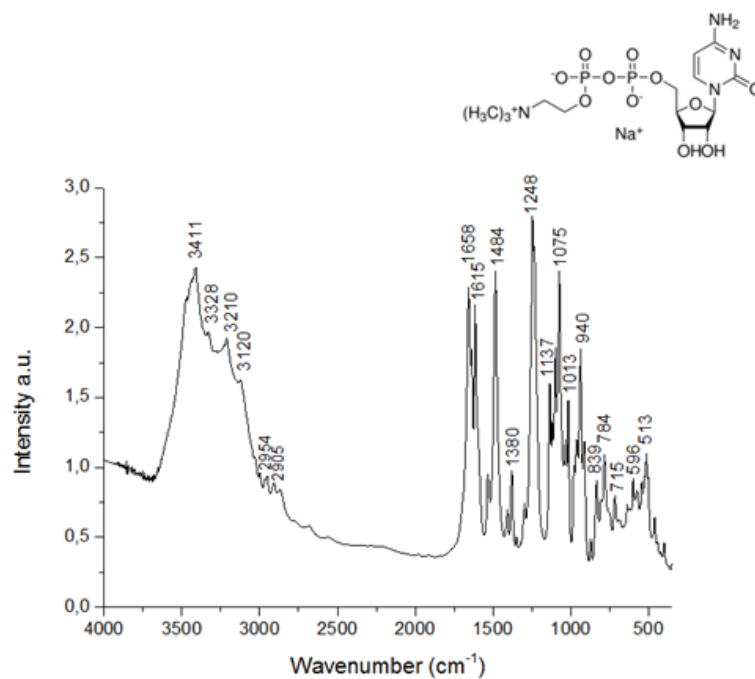**Figure 43:** FTIR spectrum of sodium citrate tribasic and the respective structure in the top corner at right [139].

Figure 44: FTIR spectrum of MUDA and the correspondent structure in the top corner at right [110].

7 Appendix

Figure 45: FTIR spectrum of MPA and the respective structure in the top corner at right [119].

Figure 46: FTIR spectrum of CDP and the correspondent structure in the top corner at right [140].

A3. FTIR tables of bare and functionalized gold nanoparticles with mercapto ligands and CDP

Table 11: Assignment of the infrared vibration bands of sodium citrate, Au NPs_10nm and Au NPs_40nm.

Vibration	Sodium citrate (cm^{-1})	Au NPs_10 nm (cm^{-1})	Au NPs_40 nm (cm^{-1})
$\nu_a(COO^-)$	1580	1584	1580
$\nu_s(COO^-)$	1386	1393	1400
$\nu(C\text{-}O\text{-}H)$	1282	1276	1269
$\nu(C-C)$	908	908	894
$\nu(C-COOH)$	838	848	841
pCH_2	749	-	-
$\rho(COO)$	616	624	624

Table 12: Assignment of the infrared vibration bands of MUDA commercial, Au NPs@MUDA_10nm and Au NPs@MUDA_40nm; MPA commercial, Au NPs@MPA_10nm and Au NPs@MPA_40nm.

Vibration	MUDA (cm^{-1})	Au NPs @MUDA 10nm (cm^{-1})	Au NPs @MUDA 40nm (cm^{-1})	MPA (cm^{-1})	Au NPs @MPA 10nm (cm^{-1})	Au NPs @MPA 40nm (cm^{-1})
$\nu(CH_2)$	2916	2925	2918	2951	-	-
$\nu(S\text{-}H)$	2545	-	-	2590	-	-
$\nu(O\text{-}H)$	-	-	-	2363	-	-
$\nu(C=O)$	1689	1733	-	1776	-	1740
$\nu(COO^-)$	1470 1436	1393	1395	-	1400	1393
$\nu(C-C)_\tau$	1206	1116	1116	1121	1123	1121
$\nu(C\text{-}O\text{-}H)$	1290	1313	-	-	1310	1303
$\nu(C-COO^-)$	943	922	922	-	929	929
$\nu(C-COOH)$	818	838	826	-	845	858

7 Appendix

Table 13: Assignment of the infrared vibrations bands of CDP commercial, Au NPs@MUDA@CDP_40nm and Au NPs@MPA@CDP_40 nm.

Vibration	CDP (cm^{-1})	Au NPs @MUDA@CDP 40nm (cm^{-1})	Au NPs @MPA@CDP 40nm (cm^{-1})
ν(C=O)	1658	1643	1649
ν(C=C)	1615	-	1587
ν(C-N)	1484	-	-
ν(C=C-N)	1380	1345	1395
ν(C-N)	1248	-	1263
ν(C−O)	1137	-	-
ν(C-H)	1075	-	-
δ_s(N-C-H)	1013	1047	1037

A4. Conjugation of Au NPs with CDP- Effect of EDC and CDP concentration

In the first attempts for performing the bioconjugation of Au NPs with cytidine diphosphocholine, CDP was added in a molecular ratio of 10:1 in relation to MUDA or MPA and the carbodiimide EDC was added in a molar ratio EDC:CDP of 10:1. In a typical experiment, EDC was added to 1 mL of functionalized gold nanoparticles and then CDP was added to the mixture. **Table 14** shows the concentration and volume of EDC and CDP aqueous solutions added in each experiment, to 1 mL of mercapto functionalized gold nanoparticles and the state of gold nanoparticles after CDP bioconjugation.

Table 14: The concentration of EDC and CDP, volumes of each used and state of Au NPs at the different trials performed for the functionalization with CDP.

| Sample	[EDC] (M)	[CDP] (M)	V(EDC) (μL)	V(CDP) (μL)	State AuNPs
AuNPs@MUDA_40nm	10^{-4}	10^{-5}	59.6	56.5	Not aggregate
AuNPs@MPA_40nm	10^{-2}	10^{-3}	20.0	19.8	-
AuNPs@MUDA_10nm	10^{-2}	10^{-3}	51.6	51.4	Aggregate
AuNPs@MPA_10nm	10^{-2}	10^{-3}	32.0	31.8	Aggregate

7 Appendix

In **figure 47** is possible to observe that only the trial using AuNPs@MUDA_40nm did not aggregate. The trials performed with AuNPs@MPA_40nm, AuNPs@MUDA_10nm, AuNPs@MPA_10nm aggregated after functionalization with CDP, in these trials the molar quantity added of EDC and CDP was higher than in AuNPs@MUDA_40nm. When EDC was added to functionalized gold nanoparticles, it was visually perceptible a repulsion of gold nanoparticles solution, followed by a stabilization of the gold nanoparticles solution. As AuNPs@MUDA_40nm was the unique one that did not aggregate, identical conditions of concentration and volume of EDC and CDP were then used for the bioconjugation of the other samples.
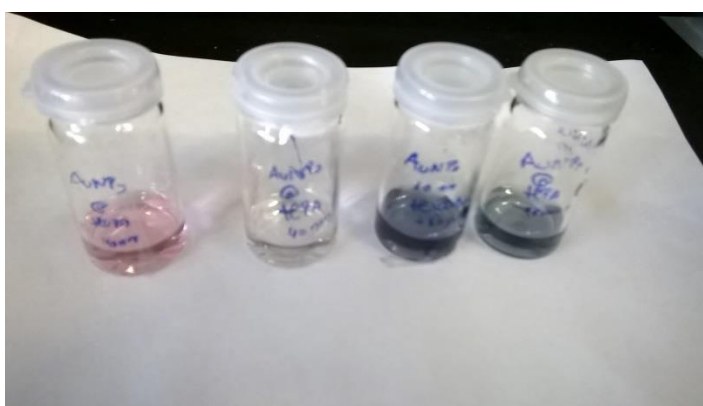

Figure 47: A photograph of AuNPs@MUDA_40nm, AuNPs@MPA_40nm, AuNPs@MUDA_10nm, AuNPs@MPA_10nm, respectively after the functionalization with CDP.

## A5. FT-Raman spectra of surface modification of Au NPs with MUDA or MPA
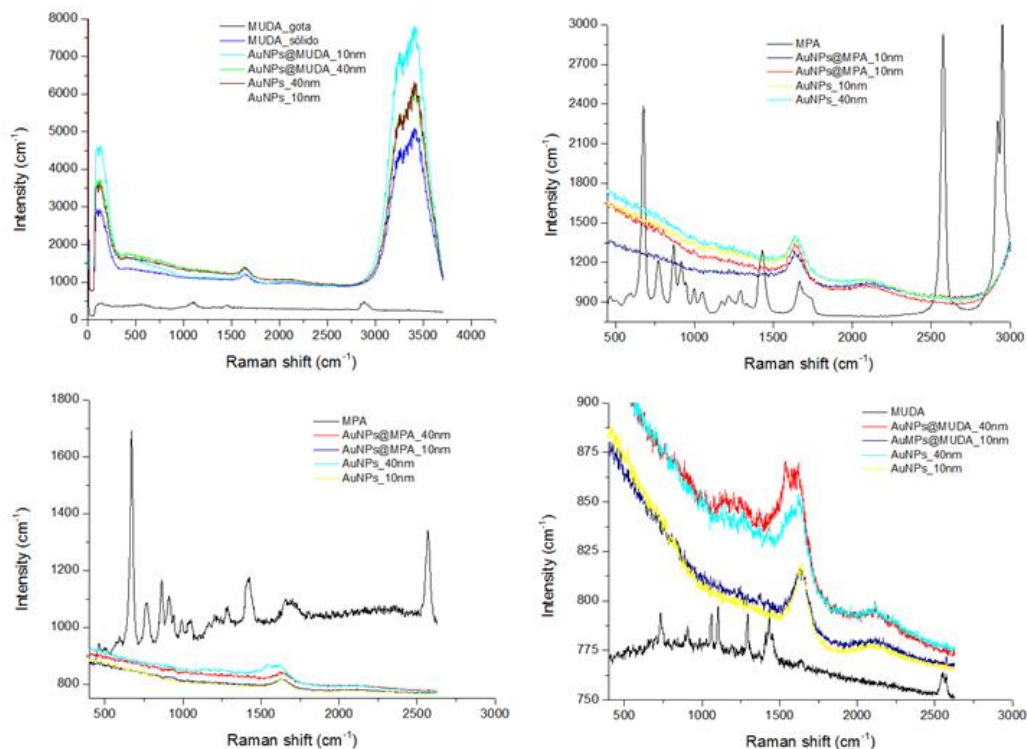
Figure 48: Raman spectra of bare and mercapto functionalized Au NPs in top corner at left and at the right with 523 nm laser; and in the bottom of the corner at left and at the right with 633nm laser.
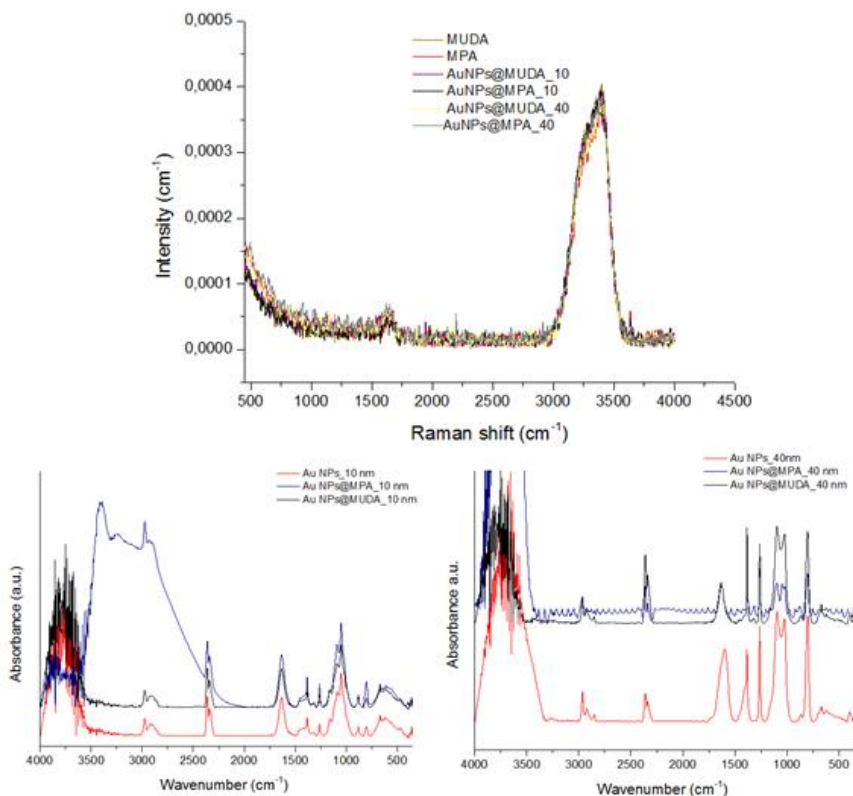
Figure 49: Raman spectra of bare and mercapto functionalized Au NPs in top with 1023 nm laser; and in the bottom of the corner at left and at the right the FTIR spectra.

A6. Surface modification with aptamer
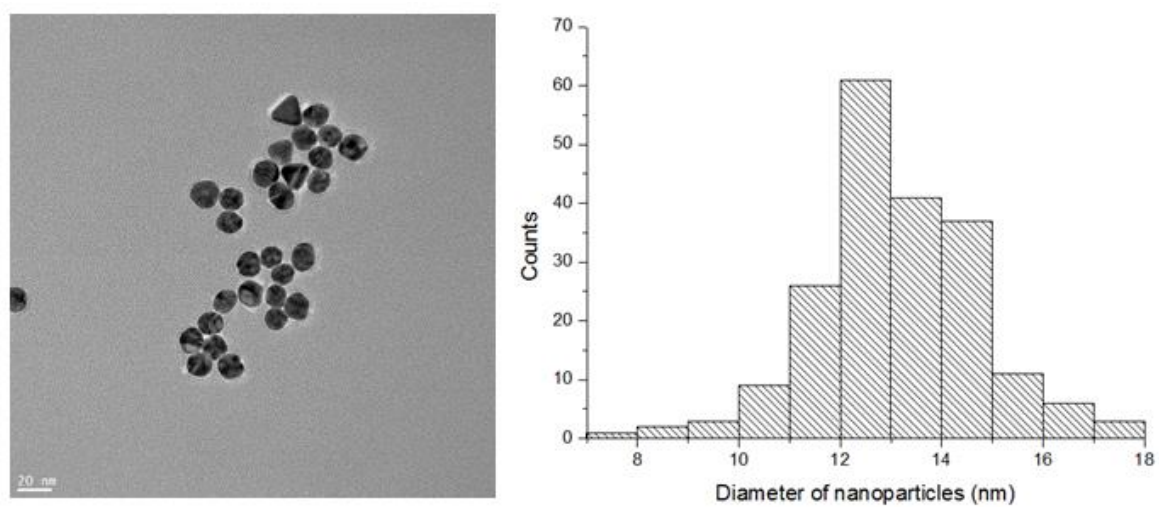
Figure 50: TEM image of Au NPs_13 nm (left) and at the right the respective histogram of particle size.